MONOLITHIC BULK PIEZOELECTRIC LATERAL BIMORPH TRANSDUCERS AND APPLICATIONS TO INERTIAL SENSOR CALIBRATION STAGES, GYROSCOPES, ULTRASONIC MOTORS AND ENERGY HARVESTERS

A Dissertation

Presented to the Faculty of the Graduate School

of Cornell University

in Partial Fulfillment of the Requirements for the Degree of

Doctor of Philosophy

by

Sachin Prakash Nadig

August 2017

© 2017 Sachin Prakash Nadig
ALL RIGHTS RESERVED

MONOLITHIC BULK PIEZOELECTRIC LATERAL BIMORPH TRANSDUCERS AND APPLICATIONS TO INERTIAL SENSOR CALIBRATION STAGES, GYROSCOPES, ULTRASONIC MOTORS AND ENERGY HARVESTERS

Sachin Prakash Nadig, Ph.D.

Cornell University 2017

A laser micro-machined bulk-piezoelectric PZT-4 (Lead Zirconate Titanate) based lateral bimorph transducer with differential drive and sense capability is demonstrated. Unlike conventional bimorph designs, the approach here does not require adhesive and/or non-piezoelectric layers. The monolithic fabrication makes arrays of bimorphs suitable for micro-systems integration. The in-plane bimorph transducer relies predominantly on the d_{31} coefficient for transduction. A bimorph transducer with length $6.25mm$, width $0.45mm$ and thickness $0.5mm$ is characterized to demonstrate DC actuation and resonance current to displacement sensitivities of $23nm/V$ and $1.1\mu A/\mu m$, respectively. Nonlinear effects in the transducer characteristics owing to nonlinear electrical and mechanical properties of PZT-4H is also investigated. The ratio of voltage amplitudes of the first harmonic ($2f$) to fundamental (f) for drive voltage amplitude V_1 is found to be $\approx 1.74 \times 10^{-5} e^{0.88V_1}$. The sense current noise of transducer is $5nA/\sqrt{Hz}$ and the sensor tip displacement measurement resolution at resonance is $\approx 0.9nm$ for small time scales ($\tau < 10s$).

A bulk-piezoelectric PZT actuator based ultrasonic motor in which the stator is an array of X-motion PZT bimorphs is demonstrated. X-motion signifies moving diagonally in the XZ plane. The bimorphs have three electrodes that are

designed to produce a bimorph tip trajectory consisting of diagonal motion in two orthogonal axes, mimicking 'X', hence the name X-motion planar bimorphs. The X-motion lateral bimorphs apply forces onto the rotor to induce rotation. The PZT bimorphs are fabricated using a laser-micromachining process resulting in monolithically integrated bimorphs to form the stator. Unlike previously reported approaches for ultrasonic motors using piezoelectric bimorphs, the fabrication process used here eliminates the need for manual bonding and selective arrangement of PZT corresponding to different poling orientations. The planar integration of the motor elements helps one to envision many co-located motor elements for multi motor systems. Three combinations of rotors and stators were tested to verify the physical model of the motor, with rotation rates of up to $400 - 600rpm$. One combination of stator and rotor operates with stator resonance of $32.6kHz$ and can withstand a load of $4.1g$ for $60V_{peak}$ drive at resonance. One of the stators is used to drive a 3D-printed plastic fan blades that produced maximum air flow rate of $160mm/sec$ at $60V_{peak}$ drive voltage.

A piezoelectric multi-modal mechanical (X, Y, θ_z) stimuli stage is demonstrated, which is capable of $\approx 50ppm$ precision in-situ calibration of MEMS gyroscopes packaged on the stage. The calibration system is capable of extracting instantaneous scale factor, bias drifts and cross axis sensitivities of MEMS Coriolis force gyroscopes. The bulk PZT calibration stage is capable of non-resonant sinusoidal angular rates of $0 - 300deg/s$ for scale factor and bias measurements and X-Y in-plane acceleration stimulus of $0 - 90m/s^2$ to extract the gyroscope in-plane acceleration sensitivities at $100V_p$, $0-250Hz$ drive voltage and frequencies. The stage has $< 5ppm/V$ undesirable out-of-plane motion while actuating in-plane for applying desired mechanical stimuli for calibration of the gyroscope. The calibration system consumes $\approx 400mWatts$ when the gyroscope is in op-

eration at baseband while the gyroscope is calibrated at higher frequencies. To achieve a long term stable calibration stage, an optical metrology system is used to calibrate the motion stage. The optical metrology system can ensure $10ppm$ stable stage metrology, to enable long term stable gyroscope calibration. The optical system uses an atomically stable laser source and a CMOS imager that can be potentially integrated into the same package as the calibration system, for closed loop control of the calibration stage.

A piezoelectric bulk-PZT Z-axis Coriolis force gyroscope is demonstrated, which utilizes spring-mass resonances of the in-plane PZT bimorphs and a PZT proof-mass. The design exploits the large piezoelectric coefficients and high mass density of bulk-PZT to obtain a sensitivity of $1.7\mu V/deg/s$, for $10V_{peak}$ drive under mode-mismatched operation and quality factor (Q) of $100-150$. The gyroscope is capable of high dynamic range owing to the elimination of micro-gaps that are associated with electrostatic gyroscopes. Nonlinearity in the elasticity properties and piezoelectric coupling in PZT is leveraged for frequency and quadrature tuning, with a DC voltage applied to control electrodes for a potential closed loop operation. Resonance and quadrature tuning of $10ppm/V_{dc}$ and $20deg/sec/V_{dc}$ respectively were achieved using nonlinear operation of PZT drive and sense resonators at $10V_{peak}$ drive at a resonance frequency of $108kHz$ drive. The gyroscope is monolithically integrated within a PZT calibration stage to enable in-situ gyroscope self-calibration. The monolithic device also improved the Q of the gyroscope by a factor of 10 leading to the improvement in sensitivity to $3.4mV/deg/sec$ at $1V_{peak}$ drive.

A 2-axis ($X-Y$) piezoelectric energy harvester is reported, whose sensitive axis in-plane is rotationally invariant, a result achieved by spiral in-place bimorph, which can be modeled as a cascade of lateral bimorphs. This is different

than conventional piezoelectric energy harvesters that are sensitive only along one axis or can realize multi-axis sensitivity through package level assembly of multiple devices at different orientations. Rotational invariance of the sensitive axis is useful when deployed in applications where the device orientation with respect to the vibration is stochastic in nature. At $1g$ applied acceleration, the vibration energy harvester generates maximum differential voltages of $\pm 6.8 V_{pp}$ across a $1 M\Omega$ load, at a resonance frequency of $163.5 Hz$. The energy harvester has a Q-factor of 129.5 and electromechanical coupling coefficient k_t of $> 15\%$ for the fundamental lateral mode and a peak normalized output power density of $0.89 \mu Watt/mm^3 g^{-2}$.

BIOGRAPHICAL SKETCH

Sachin Nadig received his B.E degree in Electrical Engineering from PES institute of technology, Bangalore, India, in 2011. He first visited the School of Electrical and Computer Engineering, Cornell University in spring 2011, as an undergraduate researcher for a semester, under the Provost International Internship Program (PIRIP). He started pursuing his Ph.D. at *Sonic*MEMS laboratory, Cornell University in spring 2012 and was awarded the Irwin Jacob's Fellowship. He worked as a research assistant during his Ph.D. pursuit, where he was part of the DARPA PASCAL program, which funded his work. During the summer of 2016, he worked on improving the performance of silicon MEMS gyroscopes, at the Advanced MEMS Development Group, Analog Devices Inc, Wilmington, MA. His research interests have been in piezoelectric transducers, and their applications in resonators, inertial sensors, energy harvesters, ultrasonic motors, and metrology.

To

my grandparents,

my parents,

Nadig family

and

Sathyanarayana family

ACKNOWLEDGEMENTS

It gives me immense pleasure to thank my advisor Prof. Amit Lal for giving me this wonderful opportunity to pursue my Ph.D. at *Sonic*MEMS laboratory. I am grateful for all the encouragement, advice and freedom that he gave me over the years. His creativity, patience, and dedication has been inspirational and has had a profound impact on me.

A special thank you to Prof. Vasudeva Iyer at PES University, Bangalore, India for recommending me to Prof. Lal.

A huge thank you to Serhan Ardanuç for all the useful discussion sessions and for being the "RED team" while bouncing off ideas. I am indebted to him for training me on the lab tools and for helping me tackle problems that came up in research. A good work atmosphere is essential during Ph.D pursuit, for which I thank the present and former members of *Sonic*MEMS group: Jason Hoople, Po-Cheng Chen, Justin Kuo, Ved Gund, Visarute Pinrod, Alex Ruyack, Mamdouh Abdelmajeed, Vinaya Kumar, Benyamin Davaji, Kwame Amponsah, Hadi Hosseinzadegan, Yuerui Lu and Ching-Ping Janet Shen. I would also like to thank the former members of OxideMEMS lab: Sidharth Tallur, Ryan Wang, and Matthew Storey for their help.

I am thankful to Prof. Sunil Bhave for his advice and moral support during times of distress. I am grateful to him for all the insightful discussions and for giving me access to his lab facilities. I would like to thank my committee members Prof. Alyosha Molnar and Prof. Christoph Studer for their support and advice.

I would like to acknowledge DARPA PASCAL program for funding this work and the program managers: Dr. Andrei Shkel and Dr. Robert Lutwak, for providing invaluable advice, which helped me focus on relevant topics. I

would also like to thank our collaborators in the program. Thanks to Dr. Bill Clark at Analog Devices Inc. for providing the gyroscope dies and for sharing his insights on MEMS gyroscopes. Thanks to Dr. David Scherer and his team at Microsemi for providing the atomically stable laser source units.

I am grateful to the staff of ECE department, especially, Scott Coldren and Sue Bulkley for making all the administrative processing smooth.

I would like to thank my friends, who were always there for me: Tanay Gosavi, Shreesha Srinath, Ajay Bhat, Anoop Grewal, Sidharth Chandrashekar, Nidhi Subramanyam, Vaibhavi Vaidya, Pooja Gudibanda Kritika Dusad, Ayush Dubey and Chaitanya Joshi for all the support and fun times during my years at Cornell.

I would like to thank my parents, Prakash and Bharathi, my extended family members for all their support and blessings, without which this would not have been possible.

TABLE OF CONTENTS

LIST OF TABLES

LIST OF FIGURES

CHAPTER 1

MONOLITHIC LATERAL PIEZOELECTRIC BIMORPH TRANSDUCER FOR MICRO-SCALE SYSTEMS

1.1 Introduction

Integrated micro-systems with actuators and sensors can be used in robotics [1–3] and Internet-of-things [4] (IoT) to address the requirements of interfacing of micro-systems with the physical world. There is a need for a technology comprising of micrometer to millimeter scale components such as precision actuators, sensors powered by limited energy sources for building autonomous micro-systems. There are many choices of transduction mechanisms that are available via micro and nano fabrication. Comb drives have been an integral elemental building block for MEMS sensors and actuators for applications such as micro-optic platforms, energy harvesters, inertial sensors etc. Comb drive devices use electrostatic transduction for actuation and sensing. Electromechanical coupling for electrostatic devices is the ratio of mechanical energy to electrical energy (k^2) scales as $\propto 1/g^4$, where g is the electrostatic gap. Hence, electrostatic transduction relies on micro to nanometer gaps to achieve sufficient electromechanical transduction efficiency. Piezoelectric transduction has been an attractive choice for micro-systems owing to their high electromechanical coupling coefficients. For example in PZT, the k_{31} which is the electromechanical coupling coefficient for electric fields applied in the thickness direction resulting in longitudinal vibrations in the $X-Y$ directions is 20% [5]. Furthermore, piezoelectric transduction eliminates the need for precision micro and nano gaps. Eliminating the gaps reduces variations in device performance due

to lithography errors and also minimizes the effect of dust particles collecting in air gaps, reducing the possibility of actuator failure by blocking gap motion.

Piezoelectric unimorph and bimorph transducers have often been used for many MEMS and mechatronics applications. They have been used for wings in centimeter scale insect inspired robots [1, 6], RF switches and mechanical logic [3], ultrasonic motors and motion stages [3] etc. Precision piezoelectric stages for linear and rotary motion have proven to be of great value in areas that require accurate positioning and calibration. Ultrasonic motors and piezoelectric actuators such as bimorphs, unimorphs, and shear tubes are key elements of these systems. Some of the best reported energy density for vibrational energy harvesters are piezoelectric bimorph-based transducers [7]. The bimorph configurations that have been studied extensively in literature often rely on manual assembly of macro/meso scale individually fabricated structures. They also involve assembly of other additional layers such as metals and adhesives for achieving the bimorph configuration. Most piezoelectric bimorphs are relatively large, millimeters in thickness, and centimeters in width and length, making them unsuitable for integration in microsystems. Alternatively, thin film MEMS piezoelectric unimorphs and bimorphs [8–10] use a limited thickness of a few microns of piezoelectric material (e.g. sol-gel PZT, AlN, ZnO, etc.) that generally do not compare favorably to the high piezoelectric coefficients found in bulk PZT [5]. There are exceptions when the thin films can be deposited in crystalline form [11] using MBE or MOCVD, however they have stringent process requirements. Additionally, thin film piezoelectric devices often have issues of stress mismatches between layers in fabrication which causes them to be curved at uncontrolled and unpredictable angles upon release [12]. Transducer configu-

rations that are not monolithic have significant problems with delamination and self-cracking which often lead to non-idealities and mismatches [12, 13]. Also, thin film piezoelectric materials can be deposited only up to several microns in thickness.

Bulk PZT ceramics have large piezoelectric coupling (k_{ij}) than most other piezoelectric materials [5]. PZT has higher fatigue resistance and stability of its piezoelectric properties over time [14] is superior to some of its thin film counterparts. Additionally, the hybrid integration aspect does not impose thermal budget constraints during fabrication on the devices to be attached to the transducers. A microsystem technology enabling monolithic integration of precision actuators and sensors all fabricated with one material (with electrodes) would eliminate problems of manual assembly, stress mismatches and thermal expansion based deformations. However, a micron-millimeter scale bimorph technology that enables many bimorph transducers with single direction of polarization to be placed precisely with respect to each other without manual assembly, without adhesive layers while providing in-plane motion control with minimal cross axis motion has not been available. In this work, a monolithic bulk-PZT in-plane bimorph transducer technology is presented to fulfill this void. A PZT bimorphs with minimum dimension of $150\mu m$ for $500\mu m$ thick substrates is demonstrated. The high aspect ratio (thickness/width $>$ 1) minimizes out-of-plane motion. The laser micromachined in-plane bimorph transducers evaluated here has a potential to be a fundamental building block of monolithically integrated microsystem components such as multi-axis motion stages [15, 16], gyroscopes [17], low power accelerometers, magnetometers, switches [18], energy harvesters [19], etc.

While laser micromachining is used here to create bimorph transducers, other direct-write (i.e, maskless) micromachining techniques such as water-jet drilling, ultrasonic drilling, electrical discharge machining, laser-assisted etching, [20,21] and micro-CNC technologies can also be used to create transducers of arbitrary shape. The laser micromachining process used here is subtractive with no additional deposition necessary. By using direct-write micro patterning technique, precision removal of PZT and/or electrode material, with double-side (top-bottom) alignment capability can be achieved. Transducers formed monolithically with additional grooves provide both in-plane and out-of-plane sensitivity. The technology here can be compared to some of the recent development of piezoelectric actuators such as PZT-on-silicon actuators [22] and the T-beam actuator described in [13]. Table.1.1 summarizes and compares this technology with existing and some of the other recent approaches for integrating many transducers together on one substrate.

Table 1.1: PZT transducer technology comparison

Parameter/Technology	Thickness/Width	DOF	Monolithic	Limitation
Commercial Bimorphs (Piezo Systems Inc)	$> 10^{-2}$	Mostly out-of-plane	No (Adhesive+other layers)	Not suitable for micro-systems
Thin film bimorph [8,10]	$< 10^{-2}$	Mostly single axis	No (Multi-layer stacking)	-Relatively poor piezo properties -Fabrication complexities
PZT-on-Si [22]	< 1	Multi-axis	No (Si/PZT bonding)	Complex fabrication
T-beam [13]	< 1	Multi-axis	Yes	Lower Q than piezo-on-Si transducers
This work	> 1	Multi-axis	Yes	Lower Q than piezo-on-Si transducers

1.2 Lateral PZT Bimorph Transducer

Fig.1.1 shows the conceptually simple monolithic in-plane bimorph transducer. The transducer can be designed with different dimensions (L, W, H) and shapes to achieve a desired resonance frequency, sensitivity to applied forces and me-

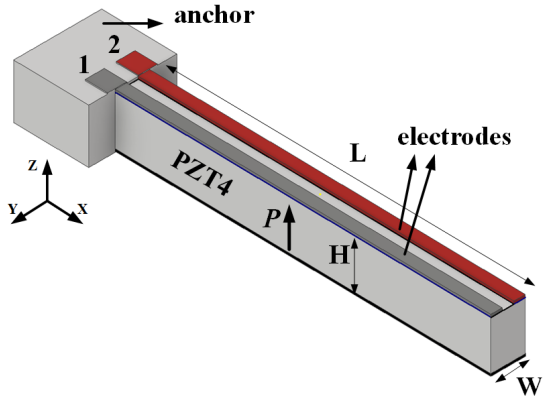

Figure 1.1: Schematic of the Lateral bulk PZT bimorph transducer. *P* indicates the polarization axis of the PZT4 plate

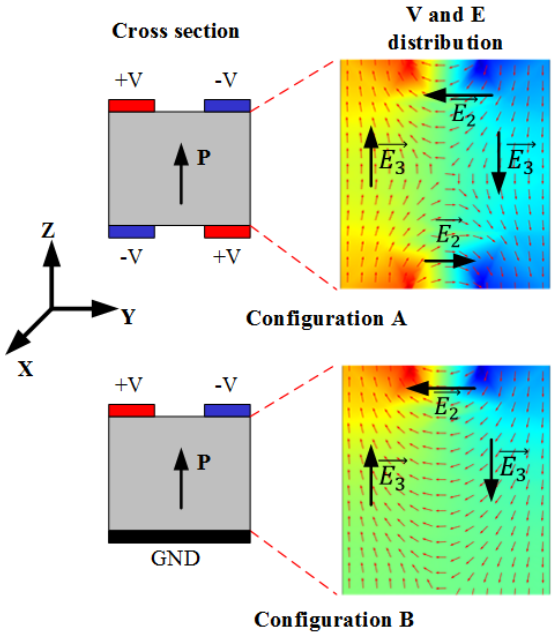

Figure 1.2: Configuration of lateral bimorph transducer with sketch of the cross section and COMSOL^{TM} simulation of electric field distribution showing electric field lines across the thickness for the configuration.

chanical forces generated for applied electric fields. The electrodes are optimized for coupling to in-plane motion for actuation and sensing. The transducer is fabricated using a 500μm thick PZT-4H ceramic substrate with silver or

nickel electrodes on top and bottom surfaces and is poled along the plate thickness. The top side of the bimorph has two electrodes (port 1 and 2) that are separated by a region with electrode removed extending along the length of the bimorph. The bottom side can either have similar electrode pattern as top (configuration A) or serve as a common ground for top electrodes (configuration B) as shown in Fig.1.2. The electrodes are connected to bond pads on the anchor. The size of the bond pads effect the input capacitance the voltage source has to drive in the actuator applications. For the sensor application, the bond pad size and placement effects the voltage sensitivity which are discussed subsequently.

1.2.1 PZT lateral bimorph as an actuator

The induced strain tensor for bulk PZT-4 under the influence of electric field (E_i) when there are no external mechanical forces is written as,

$$s = \begin{bmatrix} S_{xx} \\ S_{yy} \\ S_{zz} \\ \gamma_{yz} \\ \gamma_{zx} \\ \gamma_{xy} \end{bmatrix} = \begin{bmatrix} 0 & 0 & d_{31} \\ 0 & 0 & d_{31} \\ 0 & 0 & d_{33} \\ 0 & d_{15} & 0 \\ d_{15} & 0 & 0 \\ 0 & 0 & 0 \end{bmatrix} \begin{bmatrix} E_1 \\ E_2 \\ E_3 \end{bmatrix} \tag{1.1}$$

where, S represents the principle strains and γ represents shear strains in PZT. With the electrode patterning here, the electrodes on either sides are separated by removing electrode at the center. Therefore the charge $q = 0$ in this region. As shown in Fig. 1.2 the two non-zero electric fields in the transducer are E_2 and E_3. The applied electric field E_3 along the the thickness causes in-plane

bending due S_{xx} and S_{yy} strains induced due to $d_{31}(-1.23\times10^{-10}C/N)$ coefficient. An out-of-plane deformation is caused due to strain S_{zz} induced by $d_{33}(2.89\times10^{-10}C/N)$ coefficient. Additionally, electric field E_2 causes shear strain γ_{yz} owing to $d_{15}(4.96\times10^{-10}C/N)$ coefficient.

In-plane actuation due to E_3 and d_{31}

When a voltage +V and -V is applied on top electrodes and a common ground on the bottom, a compression is formed along the length for regions 1 and tension for region 2 along x-axis, owing to the d_{31} coefficient of the PZT beam. This causes in-plane bending along Y in the $X-Y$ plane of the beam as shown in the sketch in Fig.1.3. Configuration A allows for higher displacement compared to configuration B for the same applied voltage due to higher electric field E_3 [16]. Configuration B is discussed in detail henceforth.

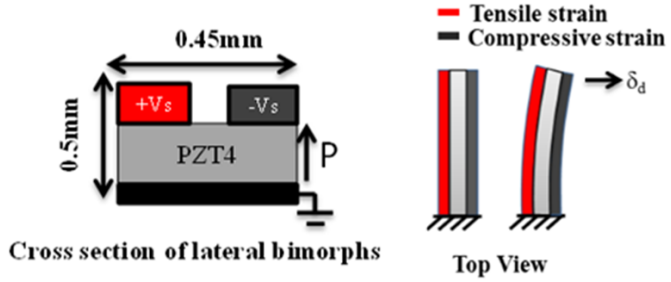

Figure 1.3: Sketch of cross section and top view of in-plane bending of bulk PZT piezoelectric bimorph transducer, operated as an actuator with differential voltage drive. P indicates the polarization

Analytical models for a conventional bimorph and other configurations with additional metal and adhesive layers have been developed by other investigators to address the non-idealities and mismatches [6,23,24]. The approach taken here eliminates the need for additional layers, and the analytical models are

hence simplified and is a special case of previously reported models.

Consider the lateral bimorph configuration as shown in schematic in Fig.1.4.

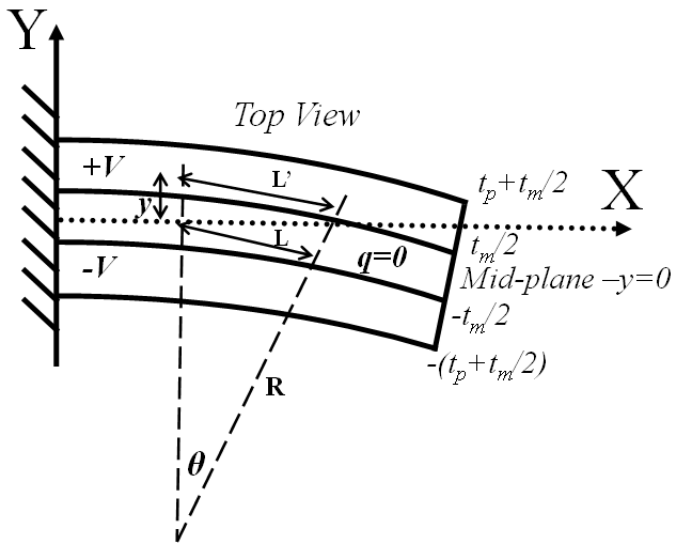

Figure 1.4: Schematic showing neutral axis, curvature, electrodes and boundary conditions.

For the piezoelectric layers with electrodes,

$$T_1 = Y_{11}S_1 \pm Y_{11}d_{31}E_3 \tag{1.2}$$

For the piezoelectric layer without electrode ($q = 0$)

$$T_1 = Y_{11}S_1 \tag{1.3}$$

From geometrical consideration of the beam, one can show that the curvature κ is,

$$\kappa = \frac{\frac{d^2v}{dx^2}}{\left(1 + \left(\frac{dv}{dx}\right)^2\right)^{3/2}} \tag{1.4}$$

Since the square of the slope (dv/dx) is small, the curvature can be approximated as,

$$\kappa = \frac{\mathrm{d}^2 v}{\mathrm{d}x^2} \tag{1.5}$$

With the assumptions of an Euler Bernoulli beam bending for the lateral bimorph, with an in-plane displacement v of the mid-plane, the strain is,

$$S_1 = \frac{L' - L}{L} = \frac{(R + y)\theta - R\theta}{R\theta} = \kappa y \tag{1.6}$$

where, y is the distance from the neutral axis (bimorph mid-plane) From (1) and (4), the bending moment of the lateral bimorph actuator can be derived as,

$$M = \int_{-(t_p + \frac{t_m}{2})}^{-\frac{t_m}{2}} (Y_{11}\kappa y - Y_{11} d_{31} E_3) h y dy + \int_{-\frac{t_m}{2}}^{+\frac{t_m}{2}} (Y_{11}\kappa y) h y dy$$

$$+ \int_{\frac{t_m}{2}}^{\frac{t_m}{2} + t_p} (Y_{11}\kappa y + Y_{11} d_{31} E_3) h y dy \tag{1.7}$$

$$M = Y_{11}\kappa h \left(\frac{t_m^2 t_p}{2} + t_m t_p^2 + \frac{2t_p^3}{3} \right) + Y_{11}\kappa h \frac{t_m^3}{12}$$
$$- h Y_{11} d_{31} E_3 \left(t_m t_p + t_p^2 \right)) \tag{1.8}$$

For a free lateral bimorph actuator, when no external moment is applied, $M = 0$, we can obtain the curvature of the actuator,

$$\kappa = \frac{12 d_{31} E_3 (t_m t_p + t_p^2)}{2(3t_m^2 t_p + 6 t_m t_p^2 + 4 t_p^3) + t_m^3} \tag{1.9}$$

Therefore, from equation (3) the lateral bimorph in-plane defection can be written as,

$$v(x) = \frac{\kappa x^2}{2} \tag{1.10}$$

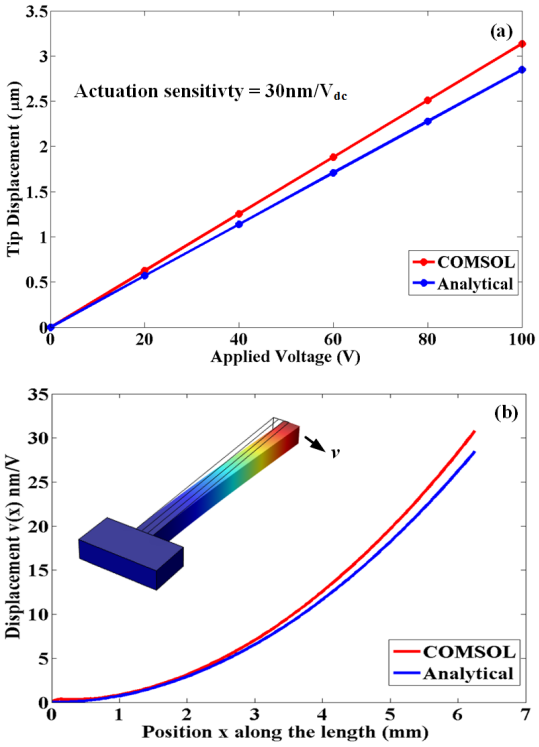

Figure 1.5: Comparison of the analytical solution with $COMSOL^{TM}$ simulation for (a) In-plane tip displacement of the bulk PZT piezoelectric bimorph transducer, operated as a differential drive in-plane actuator (Configuration B). (b) In-plane bending of bulk PZT piezoelectric bimorph transducer along the length, operated as a differential drive lateral in-plane actuator (Configuration B). Picture in the inset shows the $COMSOL^{TM}$ simulated in-plane displacement profile for differential voltage drive.

Further, results from the analytical model is compared with finite element mode as shown in Fig.1.5.Fig.1.5(a) shows the tip displacement as a function of applied DC voltages. Fig.1.5(b) shows the displacement profile of the lateral bimorph along the length. Picture in the inset shows the COMSOL^{TM} simulation of the beam deflection. As expected, the displacement profile is parabolic and is

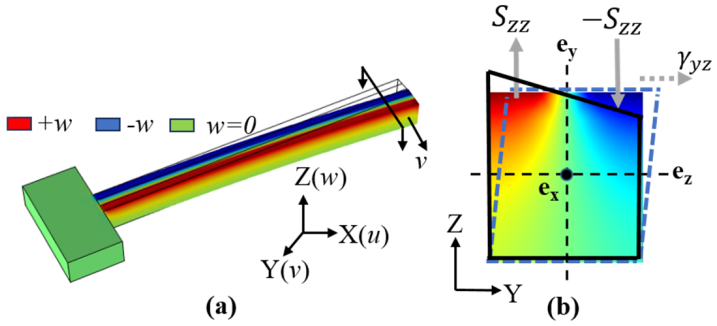

Figure 1.6: Out of plane displacement of the transducer for configuration B. (a) Shows the $COMSOL^{TM}$ simulation of the out-of-plane displacement w distribution in the transducer during in-plane bending (b) Shows the cross section showing strain S_{zz} of the transducer along the thickness and the shear γ_{yz}

in close agreement with FEA model. The simulation result is in agreement with analytical solution, with a maximum deviation of $\approx 0.083\%$ in the nm/V scale factor. This deviation is potentially due to the analytical model not including the Poisson's effect, shear strains and nonlinearities in curvature as shown in equation (4). Poisson's effect and shear strains causes additional transverse (along Y) strains caused due to axial tensile and compressive (along X) strains leading to anticlastic curvatures. The COMSOL^{TM} model includes such effects and hence estimates higher displacements as shown in Fig.1.5. For a lateral PZT-4 bimorph transducer of $L = 6.25mm$, $w = 0.45mm$ and $h = 0.5mm$, the expected actuation sensitivity is around $30nm/V_{dc}$. Since most of the actuation and sense are predominately due to in-plane strain and d_{31} coefficient, the design investigated in detail here is an in-plane lateral bimorph transducer.

Out-of-plane actuation due to E_3 and shear due to E_2

As seen earlier in equation (1) due to E_3, there is a out-of-plane deformation profile w along the length. This can be seen in Fig.1.6 for configuration B. The peak deformation along Z-axis can be written as,

$$w = d_{33}E_3h \tag{1.11}$$

the deformation is as shown in the cross section in Fig.1.6(b). Since $w \approx 0.29nm/V_{dc} << 30nm/V_{dc}$, for in-plane bending, and the contributions of S_{zz} for the overall bimorph action can be ignored. The effect due to E_2 causes shear in the Y_Z plane as shown in Fig.1.6(b). The peak deflections caused by shear (γ_{yz}) is,

$$\delta_\gamma \approx d_{15}E_2w \tag{1.12}$$

For the bimorph $\delta_\gamma = 0.45nm/V$ and hence its contributions are also negligible compared to in-plane motion.

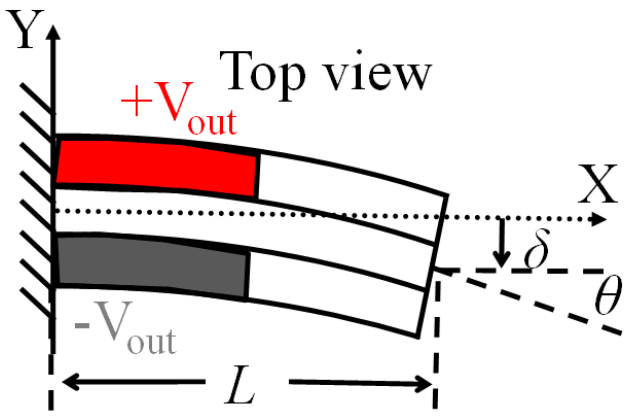

Figure 1.7: Sensor schematic showing tip deflection δ and surface potential $+V_{out}$, $-V_{out}$ induced due to strain distribution

1.2.2 PZT lateral bimorph as a sensor

When the tip of the lateral bimorph is deflected by in-plane forces, for pure bending case (Euler-Bernoulli beam assumption), there is compressive and tensile strain distribution, on either sides of the beam, along the length of the beam, with the strain magnitude being maximum at the anchor. From inverse piezoelectric effect, there is a charge accumulation on the electrodes due to strain, which can be read out. The sense signal can be current or voltage from the electrodes.

We can expect a differential voltage output on port 1 and 2 of the bimorph when an external force is applied (Fig.1.7). The electrical constitutive equation for the piezoelectric material can be written as,

$$D_3 = \epsilon_0 \epsilon_r E_3 + d_{31} T_1 \tag{1.13}$$

With the assumptions of an Euler Bernoulli beam bending for the lateral bimorph, the curvature can be written as,

$$\kappa = \frac{M}{YI} \tag{1.14}$$

where M is the moment, I is the moment of inertia and Y is the Young's modulus.

When the lateral bimorph experiences in-plane deflection δ, form (6) the strain can be written as

$$S_1 = \frac{k_{sp}\delta(L-x)y}{Y_{11}I} \tag{1.15}$$

where, k_{sp} is the spring constant of the cantilever beam, given by,

$$k_{sp} = \frac{3Y_{11}I}{L^3} = \frac{Y_{11}hw^3}{4L^3} \tag{1.16}$$

Substituting in (13),

$$D_3 = \epsilon_0\epsilon_r E_3 + d_{31}\left(\frac{k_{sp}\delta(L-x)y}{I} - Y_{11}d_{31}E_3\right) \tag{1.17}$$

$$D_3 = \epsilon_0\epsilon_r(1-K^2)E_3 + \frac{3d_{31}Y_{11}\delta(L-x)y}{L^3} \tag{1.18}$$

$$K^2 = \frac{Y_{11}d_{31}^2}{\epsilon_0\epsilon_r} \tag{1.19}$$

where K^2 is the electromechanical coupling coefficient. The total charge on the electrode is,

$$q = \int_0^L \int_{\frac{t_m}{2}}^{\frac{t_m}{2}+t_p} D_3 dxdy \tag{1.20}$$

Solving for q,

$$q = \epsilon_0\epsilon_r(1-K^2)Lt_pE_3 + \frac{3}{4}\frac{d_{31}Y_{11}t_p^2\delta}{L} \tag{1.21}$$

Using $I = dq/dt$ we get,

$$I = j\omega\left(\epsilon_0\epsilon_r(1-K^2)Lt_pE_3 + \frac{3}{4}\frac{d_{31}Y_{11}t_p^2\delta}{L}\right) \tag{1.22}$$

We can derive the output voltage of the bimorph by integrating the induced electric field E_3

$$V_{out} = -\int E_3 dz = -\frac{I}{j\omega C_{0d}} + \frac{3}{4}\frac{d_{31}Y_{11}t_p^2\delta}{LC_{0d}} \tag{1.23}$$

Where C_{0d} is the device capacitance given by,

$$C_{0d} = \frac{\epsilon_0\epsilon_r(1-K^2)Lt_p}{h} \tag{1.24}$$

The overall capacitance of the device is,

$$C_0 = C_{0d} + C_{pad} \tag{1.25}$$

where, C_{pad} is the capacitance of the bond pads on the anchors, connected to the top electrodes as shown in Fig.1.1.

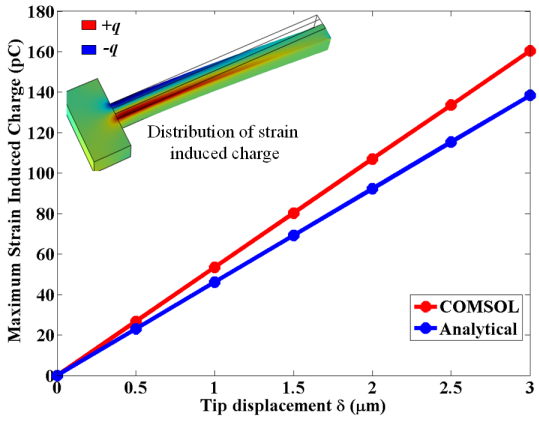

Figure 1.8: Comparison of analytical and simulation result for charge on electrodes as a function of in-plane tip displacement for a lateral bimorph transducer operated as a sensor. Picture in the inset shows the COMSOL^{TM} simulated differential surface charge distribution for in-plane tip deflections.

Fig.1.8 shows the comparison of surface charge obtained from the analytical model and COMSOL^{TM} model. From simulation and analytical solutions, we expect the sensor sensitivity to in plane deflections to be around $50pC/\mu m$. This

result is for a lateral PZT-4 bimorph transducer of $L = 6.25mm$, $w = 0.45mm$ and $h = 0.5mm$ The error between simulation and analytical result is potentially due to the analytical model not including the Poisson's effect, shear strains and non-linearities in curvature. Since the voltage from the PZT bimorph $V_{out} = q/C_0$, the output voltage can be maximized by optimal electrode placement. By having electrodes in the regions of maximum induced charge while removing the electrodes in regions with low induced charge we can minimize capacitance. As seen in the COMSOL^{TM} simulation result in the inset of Fig.1.8, it is desirable to have electrodes near the anchor and no electrodes close to the tip of the bimorph.

1.3 Lateral Bimorph Resonator

For the same transducer, using *port*1 to actuate and *port*2 to sense the response, the transducer can be tested to track sense resonator parameters such as electrical impedance, sensitivity (displacement (mV/μm) or velocity (mA/μm)), resonance frequency, insertion loss etc. The frequency response of this transducer can be measured experimentally by driving on *port*1 and sensing the resonator response on *port*2

1.3.1 Frequency response

The resonance frequencies of the bimorph can be written as [23]

$$F_r = \frac{a_n^2}{L^2}\frac{Y_{11}I}{\rho_s} \tag{1.26}$$

where, F_r is the resonance frequency, ρ_s is mass per unit area of the bimorph and a_n is the coefficient associated with each mode defined in [23]. The fundamental mode of the bimorph is in plane motion. The second mode is the out-of-plane motion with frequencies close to the fundamental mode. For the electrode configuration B as shown in Fig.1.2, the in-plane mode has the highest coupling compared to any other modes such as the out-of-plane and torsional modes. Further, the second order mechanical response of the lateral PZT bimorph can be expressed as,

$$v(x,\omega) = \frac{v(x)}{(1-(\frac{\omega}{\omega_r})^2) + \frac{j\omega}{\omega_r Q}} \tag{1.27}$$

where, quality factor Q models for all the loss mechanisms viz., anchor, viscous, material losses. In a single ended drive case discussed here on $port1$, we can expect the lateral bimorph to displace by $\frac{v_{DEA}(j\omega)}{2}$ where, $v_{DEA}(\omega)$ is the displacement for symmetrical differential voltage drive.

1.3.2 Transducer nonlinearity

Various kinds of non-linearities for PZT have been explored in literature [25,26]. Some of them are due to nonlinearity in damping forces, non-linear spring constants. These can lead to Duffing non-linearities [27], parametric oscillators and noise squeezing. Parametric resonators have proven to be useful in sensing applications to reduce the parasitic coupling into the sense from the drive electrodes [28]. Thermal noise squeezing help improve SNR and improve sensor resolution [29]. In PZT, material properties such as Young's modulus, d-coefficients, dielectric constants and mechanical loss factor have non-linear

dependence to stress, strain and electric fields [30–33].

A simple model of a spring-mass resonator can be expressed as,

$$\ddot{v} + \alpha\dot{v} + \omega_0^2 v = Fcos(\Omega t) \tag{1.28}$$

Where, α is the mass normalized viscous damping, F is the amplitude of the force, Ω is the frequency of the applied force and ω_0 is the natural frequency of the resonator. Resonant frequency of a cantilever resonator is proportional to the Youngs modulus (Y) is given by,

$$\omega_0^2 \propto \frac{Yw^3h}{4L^3m} \tag{1.29}$$

Where, m is the mass. The nonlinearity in Y due to stress in PZT can be expressed as [12],

$$Y = Y_0 + \beta Y_0 T_m^2 + (higher\ order\ terms) \tag{1.30}$$

where, $\beta = \frac{\Delta Y}{Y_0}$ and T_m is the stress.The stress caused due to applied AC and DC voltages on the bimorph is,

$$T_m = T_0 cos(\Omega t + \phi) + T_{dc} \tag{1.31}$$

Here, both T_0 and T_{dc} are proportional to $\frac{d_{31}}{h}$ and applied AC and DC voltages respectively

Substituting (31) in (30) and (29) and simplifying (28), an approximate model of the non-linear resonator can be expressed as,

$$\ddot{v} + \alpha\dot{v} + \omega_0^2 \left[1 + \beta\left(\frac{T_0^2}{2} + T_{dc}^2\right)\right] v$$

$$+\omega_0^2\left[\beta\left(2T_{dc}T_0 cos(\Omega t+\phi)+\frac{T_0^2}{2}cos(2\Omega t+2\phi)+...\right)\right]v$$
$$= Fcos(\Omega t) \tag{1.32}$$

Nonlinearity in the elastic constants can be leveraged by operating the resonator at high stress regions (stresses > 10^7 Pa) [30]. As shown in (32), the nonlinearity in E also leads to higher order harmonics in the resonator response. Similar harmonics due to resonator nonlinearity were observed in [34–36]. Stress dependent non-linearities in Young's modulus in PZT can be leveraged for applications in non-linear resonators with frequency tuning and driving parametric oscillations. Additionally, from (2) and (13) it can be seen that stress dependent non-linearities in d coefficient and dielectric constants also leads to nonlinearities in the resonator sensitivity with respect to drive voltage.

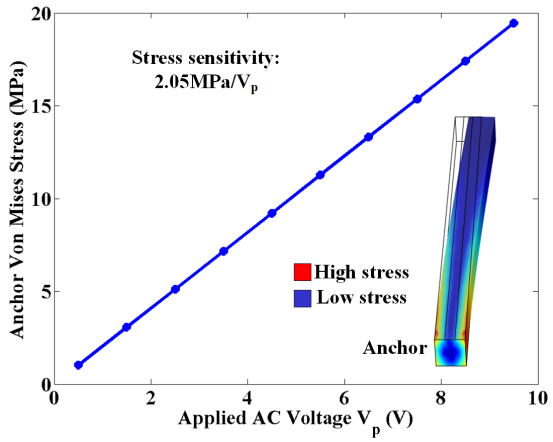

Figure 1.9: COMSOL^{TM} simulation of anchor stress as a function of drive voltage at in-plane resonance mode.

Using finite element analysis software (COMSOL^{TM}), we simulated the stress as a function of drive voltage at in-plane resonance frequency in the piezoelectric transducer. The Q factor of the resonator model is 1000, which is the mechanical quality factor (Q_m) of PZT4 as reported by the vendor (APC Inter-

national Ltd.) . This is done to calculate the drive voltage required to operate in the non-linear region. COMSOL^{TM} simulation in Fig.1.9 shows the stress distribution for the device. Simulation predicts that for this design, the Von-Mises stress at the anchor is 2.05MPa/V_p. With stress higher than 10^7 Pa for >= $5V_p$ drive at resonance(<yield stress 500 MPa for PZT [5]) we can be certain that nonlinearity can be achieved.

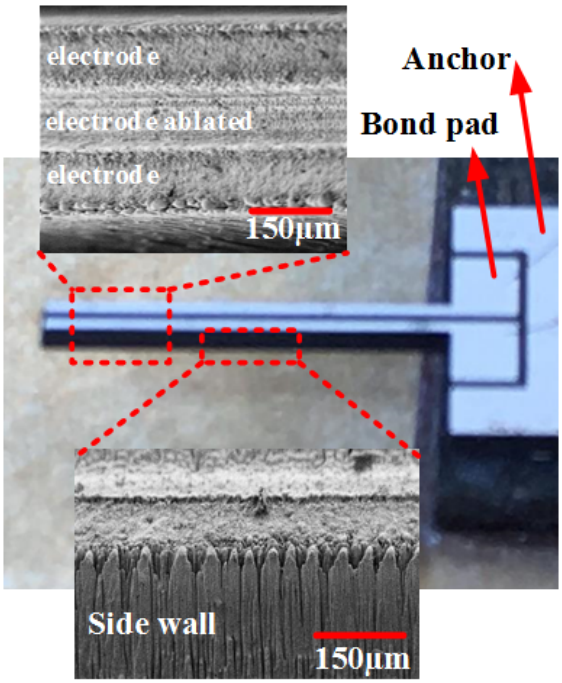

Figure 1.10: Laser micromachined lateral bimoprh transducer and SEM images.

1.4 Fabrication

The actuators were fabricated using a commercial laser tool (LPKF ProtoLaser U). A process flow is developed to create structures and electrode patterns on

bulk PZT by effective control of laser power, beam scan speed and scan lines (hatching) density. Direct laser patterning of PZT is mask-free and monolithic. A CAD file generated by commercial software (L-Edit from Tanner Tools) is fed to the control software of the laser. Here each process step is assigned a recipe, where the laser parameters, namely, laser power, frequency, scan speed, hatch density and the z-offset of the 3D stage are optimized to perform each of the steps. The fabrication steps involved are: a) Through cut of PZT plate by way of repetitive hatching on the PZT, to define the beams. b) Partial hatch through the thickness of top nickel or silver layer, so as to have electrical isolation between the two electrodes. c) Manual reversal of PZT plate for bottom side processing d) Alignment using optics and image processing associated with commercial laser tool with the help of fiducial marks created in the first step. e) Laser etching to define the bottom electrodes.

Typical cut rates for PZT are $16.6\mu m/min$ in thickness, leading to a linear cut rate for beams corresponding to a minimum cut width of $150\mu m$. After laser-micromachining, the PZT structures were cleaned with IPA (Iso-propyl alcohol) to clear the debris formed due to laser cutting and scribing process. Several batches of bimorphs were fabricated for testing the reliability and repeatability of this process. In this process the laser can be used to locally depolarize the PZT material due to heat, if used at high enough pattern density around a small PZT region. The smallest PZT feature successfully fabricated with this process flow is $\approx 70\mu m$. This limitation is a result of many factors such as laser beam size (specified to be $25\mu m$ at FWHM), material thickness and thermal conductance along with other recipe parameters such as beam hatching density, power, and pulsing frequency of the laser tool. Fig.1.10 shows the fabricated PZT lateral bimorph transducer with SEM images in the inset showing the top surface and

the side wall of the bimorph. More details of the process flow are discussed in the work in [15, 16].

1.5 Experimental Results

All the characterization work is done for a lateral PZT-4 bimorph transducer designed for $L = 6.25mm$, $w = 0.45mm$ and $h = 0.5mm$ with the two top electrodes separated by a $0.15mm$ wide region with electrode removed along the length of the lateral bimorph.

1.5.1 Characterization of PZT bimorph actuator

In order to characterize the the tip displacement sensitivity as a function of drive voltage, an in-plane optical stroboscopy technique is used. A sinusoidal drive voltage near DC (10Hz) is applied and the device displacement amplitude is measured optically using the Polytec MSA400. In this approach, a 20X lens and CMOS imager in the Polytec tool is used and the displacement noise in the measurements is $\approx 300nm$. Fig.1.11(a) shows measured tip displacement as a function of applied differential voltages on port1 and 2. The actuation sensitivity is measured to be $23nm/V$, which is within 10% to the simulation and the analytical result. The error can can attributed to measurement noise and the the fabrication tolerances. Since the laser spot size is $25\mu m$ one can expect tolerances in w and L to be $\approx \pm 25\mu m$ corresponding to worst case variations of $\approx \pm 13\%$ in k_{sp} (equation (16)). On sweeping the frequency for the applied voltage of $1V_p$ in configuration 2 (Fig. 1.2), the in-plane resonance response with peak tip dis-

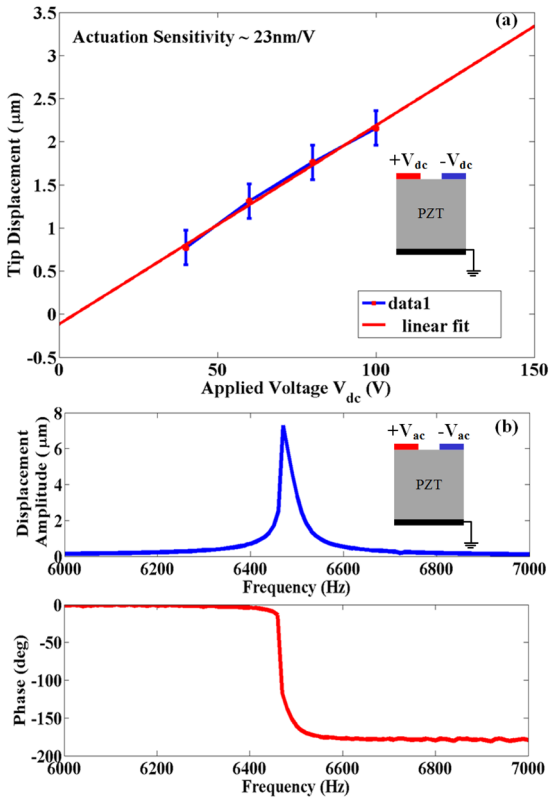

Figure 1.11: Optical charaterization of lateral bimorph actuator using Polytec in-plane stroboscope. (a) shows the amplitude of tip in-plane displacement as a function of applied differential voltage near DC (10Hz). (b) shows the in-plane tip displacement frequency response for $1V_p$ differential drive.

placement of 7.3μm at resonance frequency is measured optically Fig.1.11(b).

The impedance response of the bimorph transducer is measured using HP4194A as shown in Fig.3.9. An equivalent RLC circuit model fit (Butterworth Van-Dyke model) for the linear resonator case is obtained using the measured impedance response. The parameters from the equivalent circuit model for linear resonator case with drive voltages of $< 100mV_p$ are summarized in Table.1.2. It is observed that the resonator has a non-linear response for higher drive voltages ($>= 0.5V_p$). There is spring softening effect in the PZT bimorph resonator as the drive voltage is increased, as shown in Fig.1.11(b) and Fig.3.9. Since the

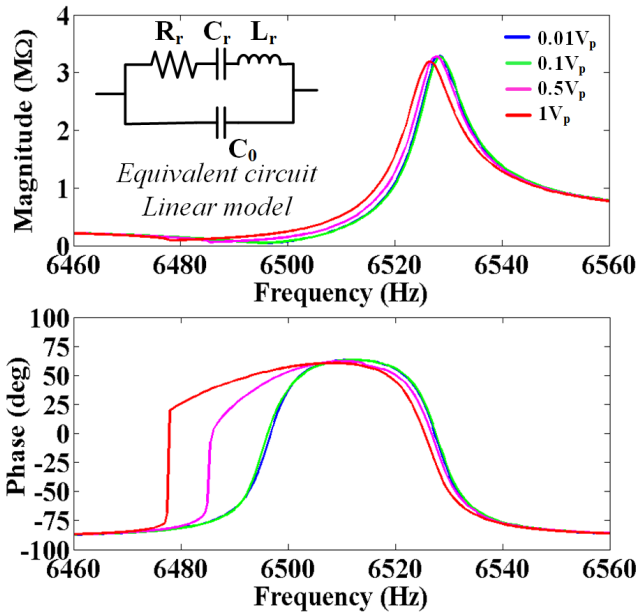

Figure 1.12: Impedance response of the bimorph transducer as a function of drive voltage, measured using HP4194A impedance analyzer. Sketch in the inset shows the equivalent circuit model for the linear resonator at drive voltage of $< 100mV_p$

impedance analyzer used can drive a maximum voltage of $1V_p$, the non-linear behavior of the bimorph transducer as a function of higher voltages is investigated using high speed ADC and function generators which is discussed in section *V.C*.

1.5.2 Characterization of PZT bimorph sensor

As discussed in III.A, on driving the transducer on *port*1 and sensing the voltage or current response on *port*2 we can characterize the transducer sensor characteristics. In this configuration we can expect half the tip displacement for the same drive voltages at resonance as seen in Fig.1.11. On sweeping drive frequency for $1V_p$ drive on *port*1 the frequency response on *port*2 of the lateral bi-

Table 1.2: Parameters from equivalent circuit model of the linear bimorph transducer for drive voltages < $100mV_p$

Parameter	Value
C_0	$62.1pF$
R_r	$47.2k\Omega$
C_r	$605.7fF$
L_r	$991H$
$Q = 2\pi f_r L_r / R_r$	850
f_r(resonance)	$6.49kHz$
f_a (anti-resonance)	$6.52kHz$
$k_{31} = \sqrt{\left(\frac{f_a}{f_r}\right)^2 - 1}$	12%

morph sensor is measured (Fig.1.13). The peak voltage response was measured to be around $6.5kHz$. As shown in Fig.1.13 both the voltage and the current from sense *port*2 are measured for $1V_p$ drive as a function of frequency. Using results from Fig.1.11, the peak displacement at resonance for driving just *port*1 can be estimated to be $3.65\mu m$ at resonance. The peak voltage and current on sense port for this configuration are $125mV$ and $4\mu A$ respectively, from Fig.1.13. So the the lateral bimorph sensor sensitivity at resonance are $\approx 38.5mV\ /\mu m$ and $\approx 1.1\mu A\ /\mu m$ respectively. The result is in agreement with the analytical result of $1.02\mu A/\mu m$ at resonance for the single-ended drive case (section *II.B*) (Charge sensitivity × resonance frequency = $25pC/\mu m \times 2 \times \pi \times 6500Hz$). The sensitivity is only applicable for strains below yield (< 0.5%). As observed in Fig.1.11 and Fig.3.9, we again see the spring softening effect in the output current response of the bimorph resonator for $1V_p$ drive (Fig.1.13(b)).

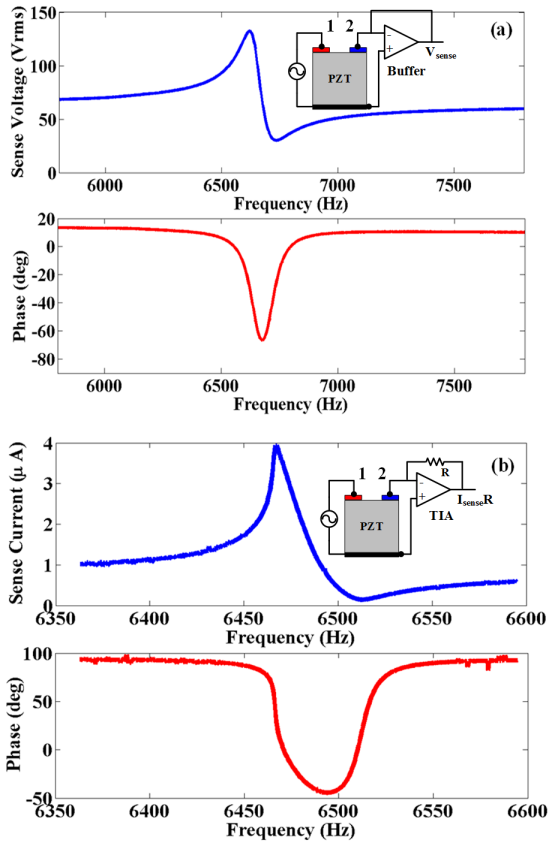

Figure 1.13: Electrical Frequency response characteristics of bimorph transducer. (a) Sense voltage response on *port*2 as a function of frequency for $1V_p$ drive on *port*1 (b) Sense current frequency response on *port*2 for $1V_p$ drive on *port*1.

1.5.3 Characterization of resonator nonlinearity

On measuring the output spectrum of the transducer's *port*2 on driving *port*1 at resonance frequency (Fig.1.14(a)), we see a peak response at the resonance frequency as expected. Additionally, higher order harmonics of the resonance frequency with lower amplitudes are observed as predicted by equation (32). This is observed only at resonance, when the stress criterion for nonlinearity is met, as discussed earlier. Further, the dependence of amplitude of the harmonic response to applied drive voltage stress is characterized. The frequency spec-

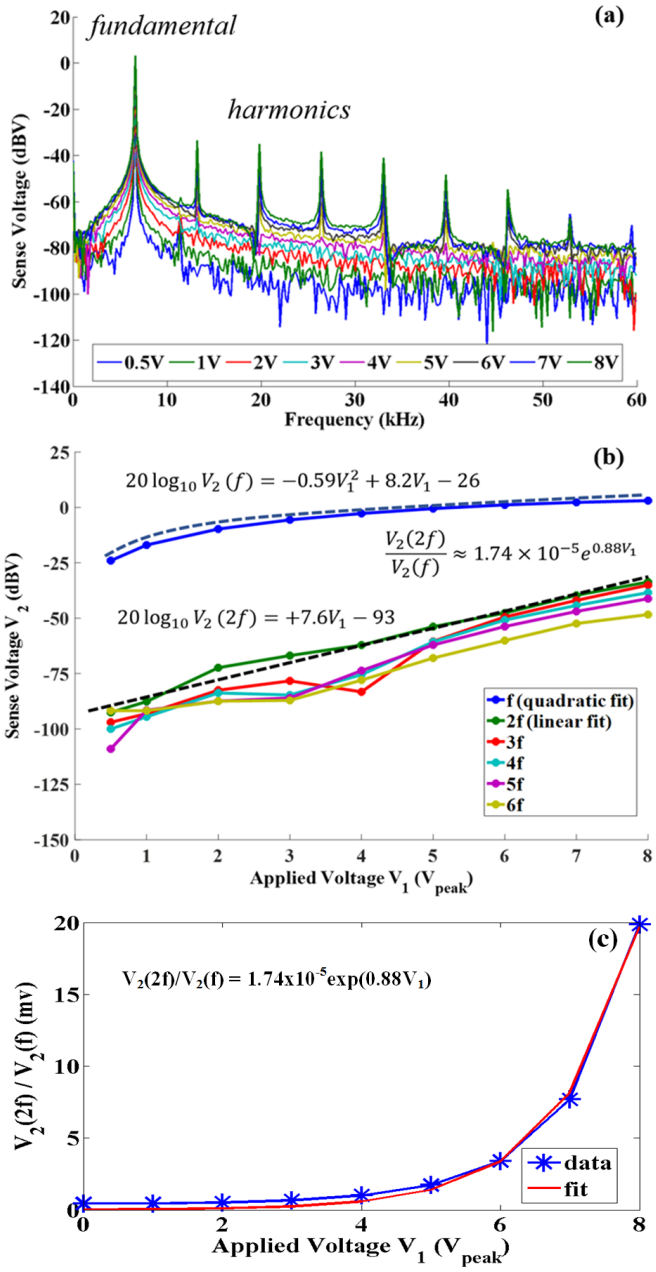

Figure 1.14: (a) Frequency spectrum of *port*2 sense voltage for different drive voltages at resonance at fundamental on *port*1. (b) The dependence of amplitude of harmonic components as a function of drive voltage V_1. (c) Ratio of the voltage amplitude of the first harmonic ($2f$) to the fundamental (f) as a function of drive voltage V_1

trum for different drive voltages at resonance are are as shown in Fig.1.14(b). It can be seen that the the amplitude of the harmonic components increase with drive voltage. This is because of increase in stress leading the resonator to be more non-linear as described by equation (32). The ratio of voltage amplitudes of the first harmonic ($2f$) to fundamental (f) is found to be $1.74 \times 10^{-5} e^{0.88V_1}$, where V_1 is the amplitude of the drive voltage on $port1$

1.5.4 PZT bimorph sensor performance

In order to validate the performance of the lateral bimorph transducer as a sensor, the different noise sources prevalent in the sensor are measured. Due to the pyroelectric and temperature dependent properties of PZT (d-coefficients and dielectric constants), one can expect voltage and current noise on the sense port. Also, there is noise induced by frequency drift in the resonator. Additionally, one can expect errors arising from resonator aging [14] and self-heating over time [37, 38]. To alleviate the noise from parasitic capacitances and $60Hz$ noise, the current from the bimorph transducer is sensed using a transimpedance amplifier circuit. Assuming the noise sources are uncorrelated, the sense current i_{out} on sense $port2$ can be expressed as,

$$i^2_{out}(t, T, j\omega) = i^2_{out}(t, j\omega) + i^2_{ne}(T, j\omega) + i^2_{nm}(T, j\omega) + i^2_{pyro}(T)$$
$$+ i^2_{\Delta f}(t, T) + i^2_{flicker} \tag{1.33}$$

Further, for the bimorph the fundamental noise sources can be calculated as follows, with Table.1.3 describing all the parameters and design specifications,

PZT electrical-thermal noise can be expressed as [39],

$$V_{ne} = \sqrt{\frac{4k_B T}{\omega Q C}} \tag{1.34}$$

PZT mechanical-thermal noise from [39],

$$V_{nm} = \sqrt{\frac{4k_B T \omega_0 q_T^2}{mQC^2}} \tag{1.35}$$

Contributions from current induced by pyroelectric effect in PZT owing to resonator self heating can be estimated as [40,41]

$$i_{pyro} = \lambda_p A_e \frac{dT}{dt} \tag{1.36}$$

Where λ_p is the pyroelectric coefficient. The thermal time constant $\tau_{th} = R_{th}C_{th}$, R_{th} having contributions from conduction through metal, air and convection components R_c, R_{ca} and R_{conv} respectively.

$$\frac{1}{R_{th}} = \frac{1}{R_c} + \frac{1}{R_{ca}} + \frac{1}{R_{conv}} \tag{1.37}$$

$$R_c = \frac{h}{\kappa_{PZT} A},\ R_{ca} = \frac{1}{4\kappa_{air} r},\ R_{conv} = \frac{1}{h_c A_e} \tag{1.38}$$

where $r = L/\sqrt{\pi}$

$$C_{th} = \rho_{PZT} V c_p \tag{1.39}$$

For experimental validation of different noise contributions prevalent in the sensing system, Allan deviation of bimorph *port*2 current is measured for $1V_p$ voltage drive . Allan deviation in Fig.1.15 shows these different noise sources and their dominance over different time scale and averaging times. The current from *port*2 is measured using a tranimpedance amplifier SR570 for no drive and

Table 1.3: Parameters and design specifications

Parameter	Value
charge sensitivity q_T	$10^{-13} C/m/s^2$
pyroelectric coefficient λ_p	$10^{-4} C\ /m^2\ /^\circ C$
T	300K
Q	850
C	24pF
Electrode area A_e	$2.81 \times 10^{-6} m^2$
bandwidth	225Hz, 50Ω termination
i_{ne}	0.56nA
i_{nm}	0.34 nA
i_{pyro}	$0.937nA\ /(^\circ C\ /s)$
Acquisition circuit noise	$\approx$ 3.2nA
κ_{air}(room temperature)	0.026 W/m K
κ_{PZT}	1.1 W/m K
c_p (PZT)	420 kJ/Kg K
h_c	$20\ W/m^2K$
(convective heat transfer coefficient)	
R_{th}	1.089×10^3 K/W
C_{th}	4.5×10^{-3} J/K
τ_{th}	4.9 s

drive at resonance cases as shown in Fig.1.15. From the analytical calculations and Allan deviation measurement in Fig.1.15, it can be seen that for a no drive case (broad band measurement, blue curve), we are limited by acquisition circuit noise. However, for the $1V_p$ drive case at resonance, the Allan deviation of

demodulated voltage with a $10Hz$ low pass filter stage for $port2$ current (narrow band measurement, red curve) is limited by fundamental noise sources such as the mechanical-thermal noise and electrical thermal noise as calculated. Further, with increase in the resonator operation cycles ($\tau > 1s$) the noise arising from self heating effect dominates and causes sensor noise due to frequency drift (Δf), and probably noise induced by pyroelectric effect ($i_{pyro} = 0.937nA\ /(^{\circ}C\ /s)$). It has been shown in [37] that the self-heating origin is probably interaction between the domain and defects. The heating rate can be visualized as the heat generated by friction of the domains moving in a viscous medium. This in-turn effects the polarization of PZT and effect the dielectric constant, d-coefficients and Young's modulus leading to current noise.

Therefore, sensor current measurements for small averaging times ($1s$) is preferable. In order to reduce voltage/current noise, additional controls such as automatic gain control PID loops and phased lock loops (PLL) on the drive are necessary to lock to stable drive displacement amplitude and resonance frequency respectively. However, active temperature compensation or dedicated design considerations are necessary to suppress the temperature induced noises. From the Allan deviation measurements in Fig.1.15, the sensor tip displacement measurement resolution at resonance is estimated to be $\approx 0.9nm$ for small time scales ($\tau < 10s$).

1.6 Conclusion

A monolithic piezoelectric bimorph transducer was designed, fabricated and tested. The applications of the lateral bimorph to actuators and sensors are were evaluated. An in-plane resonator and its stress dependent non-linear properties

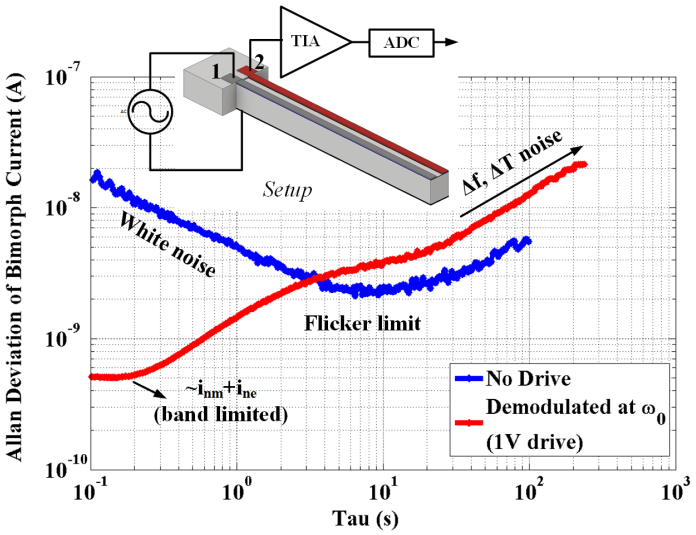

Figure 1.15: Allan deviation of current from lateral PZT bimorph transducer. Plot shows the comparison of a broad band measurement ($1kHz$) of sensor noise under no drive condition and a narrow band sensor noise with $1V_p$ drive to isolate different noise sources. Sketch in the inset shows the measurement setup

was also explored. Further, different noise sources prevalent in the lateral bimroph sensor were characterized to measure sensitivity of actuator, sensor and sensor resolution.

CHAPTER 2

LASER MICROMACHINED SINGLE-PHASE ULTRASONIC MOTOR UTILIZING A PLANAR X–MOTION PZT BIMORPH STATOR

2.1 Introduction

Ultrasonic motors have found widespread applications in systems such as camera focusing assemblies, micro positioning devices, automation and biomedical instruments [42–44]. Ultrasonic piezoelectric motors transform electrical energy into mechanical motion using the inverse piezoelectric effect. The stator comprises of piezoelectric transducers which is actuated by applying suitable voltages, generating forces which are transferred through frictional coupling to a rotor [43]. Ultrasonic motors offer many advantages including high drive and hold torques and small displacements enabling precise position control of loads [42]. Because the motors are made of piezoelectric materials, without the need of magnetic materials, the motors can operate without interference from external magnetic fields.

Ultrasonic motors have been made with size scales ranging from mm to 10's of cm, with different vibrational modes, and different mechanisms of momentum transfer to the rotor. These include direct contact and viscous drag through air bearing [45, 46]. The conventional piezoelectric motors are traveling wave ultrasonic motors, which consist of composite piezoelectric actuators arranged in a circular configuration. The actuators generate circular traveling vibration modes in which the clock-wise and counter-clockwise traveling waves result in standing waves with elliptical trajectories on the stator. The stator forms frictional contact point to the rotor [47,48] applying normal and tangential forces to

move the rotor. In hybrid-mode piezoelectric motors, the piezo-ceramic plates are arranged such that different phase signals excite, (i) longitudinal and bending modes [49–51], (ii) or two orthogonal longitudinal modes [52,53], (iii) or two orthogonal bending modes [54,55] simultaneously and imparts motion onto the rotor via frictional coupling. Ultrasonic motors with piezoelectric bimorph as the driving elements also exist in literature. Piezo-ceramic plates are bonded, electrically isolated, and are controlled independently such that the excited signal pattern actuates the tip of the bimorph [56–60].

In many existing ultrasonic motors, the stator is manually assembled by adhesive bonding of the piezo-ceramics. The stator designed using this technique have been shown to have significant problems such as delamination and self-cracking [61]. Stress mismatch between layers of PZT- adhesive composites often causes stress gradients leading to deflected structures after fabrication. This makes the stator prone to fatigue under conditions of high electric field drive, which can lead to failure of the motor [44]. The additional adhesive layer leads to complexity of the ultrasonic motor analytical/FEM model as the adhesive thickness can vary across the motor making stator to rotor coupling hard to be uniform and are device specific. The adhesive layer can also add to damping and generate heat during operation. Many different techniques have been investigated to overcome these problems [60, 62] through complex assembly processes, which increases cost and size of the device and limit performance.

In this work, an ultrasonic motor with PZT bimorph actuators that does not require manual bonding of the bimorphs is demonstrated. Bulk PZT ceramics are important for motor as PZT has larger piezoelectric coupling (k_t), and piezoelectric coefficient (d_{31}) than many other piezoelectric materials. In this motor,

the stator is a monolithically integrated, circularly arranged array of PZT bimorphs [63] with multi-axis actuation capabilities. The design is planar and is realized through direct-write, single step laser-micromachining process, which is suitable for miniaturization with 100μm minimum feature size. This process enables fabrication of mm scale bulk PZT ultrasonic motors which are currently realized at 10's of mm. Also, this approach allows for decoupling of process flows for the fabrication of stator, rotor and substrate housing the stator. Since each layer (substrate, stator and rotor) are fabricated independent of each other, various applications can be possible. One such example is a 3D printed plastic blade fan rotor using the laser micromachined monolithic PZT bimorph stator. The design and working principle is introduced in Section 2, along with FEM and analytical results. Device fabrication is explained in Section 3. This is followed by experimental results and a discussion in Section 4. The operation of a 3D printed ABS plastic fan shaped rotor as well as a baseline, minimal-load rotor is also presented. Finally, Section 5 gives a summary of results along with concluding remarks.

2.2 The Basic Building Block: X-Motion PZT Bimorph

2.2.1 Design

The piezoelectric beam design shown in Fig.2.1 is used as a fundamental building block in the stator design. The PZT-4 beam actuator consist of silver electrodes on top and bottom and is poled along the thickness of the plate. The top side of the beam actuator has two electrodes, $A1$ and $B1$, which are separated by

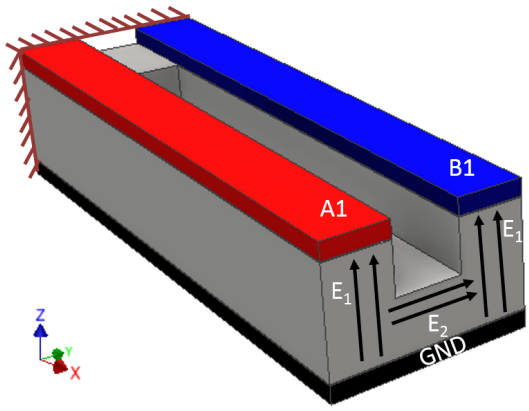

Figure 2.1: Schematic of the monolithic multi-axis piezoelectric bimorph.

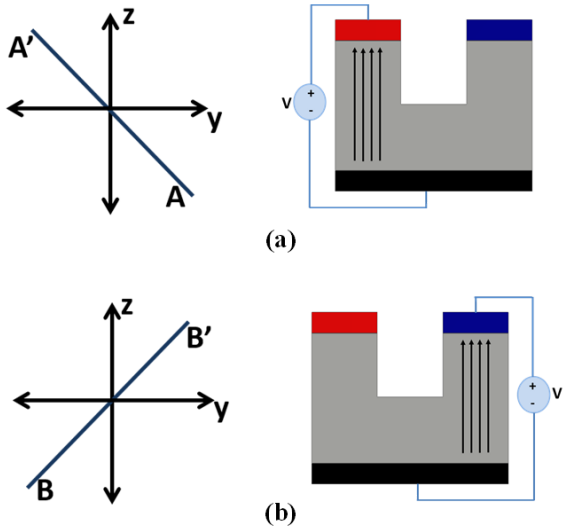

Figure 2.2: Motion trajectory of the tip of deflected beam when voltage applied to (a)electrode $A1$ and (b)electrode $B1$.

a rectangular groove that extends along the length of the beam. The electrode at the bottom serves as a common ground for the top electrodes. When a voltage $+V$ is applied on $A1$ and $-V$ is applied to $B1$ electrodes, a compression is formed along the length of $A1$, and tension along $B1$, owing to the piezoelectric coupling due to $d_{31}(-1.23 \times 10^{-10} C/N$ for $PZT-4)$. Hence, this structure can be called a lateral bimorph, as most of the motion can occur in the plane of the plate. Such

bimorphs are used for realizing dither stages and piezoelectric sensors [17, 64]. In addition to the lateral bimorph motion, an out-of-plane tip motion can be generated by applying voltages with different phases on $A1$ and $B1$ electrodes.

The region of the beam under the influence of applied electric field can be considered as active and the remaining region as passive. The drive configuration is as shown in Fig.2.2 where AC signal is applied between electrode $A1$ (or $B1$) and bottom electrode and while keeping the other top electrode $B1$ (or $A1$) grounded. The drive scheme enables for 2 orthogonal applied electric fields E_1 (along thickness) and E_2 (along width) as shown in Fig.2.1 The lateral bending is due to strains generated owing to d_{31} coefficient in PZT when electric field is applied along the poling direction in the active part of piezoelectric beam. The cross field E_2 along the width of the bimorph causes shear owing to d_{15}. Additionally, the groove cut in between A and B electrode reduces the moment of inertia along the thickness of the bimorph and moves the centroid closer to the ground electrode (plane of neutral axis as per Euler-Bernoulli Beam equations), improving the out-of-plane displacements. This results in both in and out of plane motion with trajectory as described in Fig.2.2. The beam will follow trajectory $A - A^{'}$ [shown in Fig.2.2(a)], when AC voltage is applied between electrode A1 and the common ground. It will bend long path $B - B^{'}$ [shown in Fig.2.2(b)], when the AC voltage is applied to electrode B1.

This actuator is similar to the T-beam actuator presented in [60]. In this work laser micro-machining is used to fabricate a U-beam actuator with aspect ratio (thickness/width) <= 1 compared to the T-beam with aspect ratio 0.5.

2.2.2 Analytical model of the lateral PZT bimorph

To predict the tip deflection and blocking force of the piezoelectric motor, analytical model previously developed for piezoelectric T-beam actuator [61], for a general asymmetric piezoelectric actuator, is modified for this design. The governing equation is derived using the principle of virtual work with the assumptions of Euler-Bernoulli beam conditions [61]. From the constitutive equations, the resultant maximum in-plane (v_f) and out-of-plane displacement (w_f) are shown. For the asymmetric configuration of designed piezoelectric beam, neutral axis will lie at a location e. Here w represents width of piezoelectric beam, s is separation between two electrodes, h is the overall thickness of beam, $(h - t)$ is the depth of PZT hatched region [Fig.2.4(a)].

$$e = \frac{1}{2}\frac{2wht - 2sht + sh^2 + st^2 - wh^2}{wh - hs + ts} \tag{2.1}$$

$$v_f = \frac{a_8 A_{p2} L^2 V}{2E_p(I_{p2} + I_{b2})} \tag{2.2}$$

$$w_f = -\frac{a_4 A_p L^2 V}{2(2a_2 I_{p3} + 2a_3 A_p + E_p I_{b3})} \tag{2.3}$$

Here, E_p represents Young's modulus of the piezoelectric material, L is length of beam and V is the applied voltage between one of the top and bottom electrode. The blocking forces for individual beam, F_{2b} in longitudinal direction and F_{3b} in transverse direction can be represented as follows,

$$F_{2b} = (3a_8 A_{p2} V)/2L \tag{2.4}$$

$$F_{3b} = -(3a_4 A_p V)/2L \tag{2.5}$$

The actuator is divided into an active (volume with non-zero electric field) and passive parts (volume with no electric field). The coefficients in the expressions are tabulated below (Table.2.1). Subscript b and p represent coefficients for passive and active parts of the actuator respectively. The results obtained from the analytical model of PZT bimorph is compared with COMSOL^{TM} FEA simulation in Fig. 2.3. The analytical model of the bimorph does not include Poisson's effect and shear from d_{15} strain coefficient. Therefore, for the out-of-plane (Z) actuation, there exists a deviation of $0.4nm/V$ between the analytical and FEA simulation result.

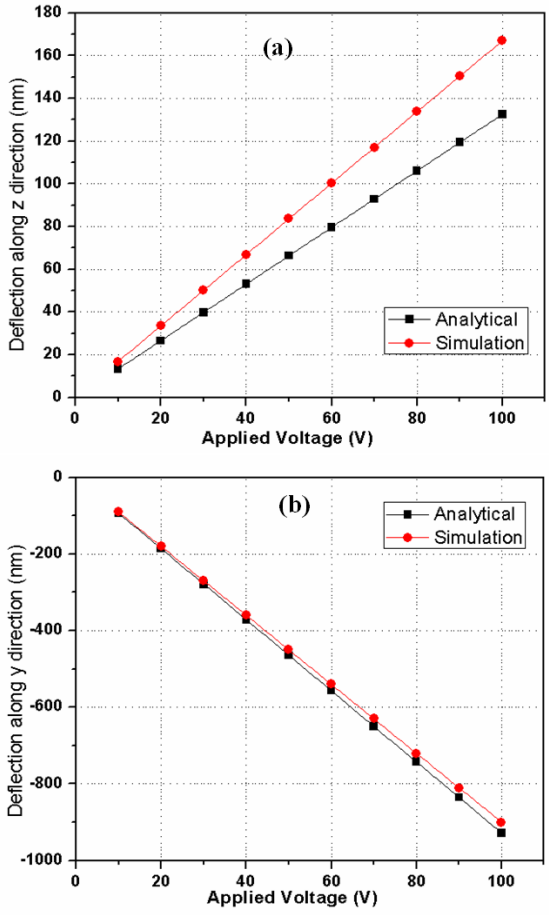

Figure 2.3: Maximum displacement vs driving voltage of 5 mm long beam with 250μm cut in between two electrodes for (a) out-of-plane motion (b) in-plane motion.

Table 2.1: Derived Constants Used in Model

Coefficient	Single Electrode	Both Electrode
a_2	$\frac{1}{2}(E + \frac{{e_{31}}^2}{\epsilon_{33}})$	
a_3	$\frac{-e_{31}^2(2e+h-2t^2)}{8\epsilon_{33}}$	
a_4	$\frac{-e_{31}^2(2e+h-2t)}{2h}$	
a_8	$\frac{-e_{31}}{h}$	
A_b	bt	$\frac{(2t-h)b+sh}{2}$
A_p	$h(s-b)$	$\frac{(s-b)h}{2}$
A_p2	0	$\frac{h(s^2-b^2)}{8}$
I_b2	$\frac{b^3t}{12}$	$\frac{(2t-h)b^3+s^3h}{24}$
I_p2	$\frac{h}{12}(s^3-b^3)$	$\frac{h}{24}(s^3-b^3)$
I_b3	$\frac{bt^3}{12} + A_b(e-\frac{t}{2})^2$	$I_p3 + \frac{th^3}{12} + bt(e-\frac{t}{2})^2$
I_p3	$\frac{(s-b)h^3}{12} + A_p(e-t+\frac{h}{2})^2$	$\frac{(s-b)h^3}{24} + A_p(e-t+\frac{h}{2})^2$

2.3 Stator Design And Motor Operation

The stator of the ultrasonic motor consists of a circular arrangement of twelve PZT lateral bimorphs, each of length L, placed at equal angles away from each other (shown in Fig.2.4(b)). The bimorphs are formed from one PZT plate. Each beam is patterned with two separate electrodes (A_n and B_n). On each individual bimorph, PZT has been partially removed in between the two electrodes and the cross-section view of beam is shown in Fig. 2.4(a), to form a U-shaped beam. The stator can produce two orthogonal motions, where the tip of the actuator

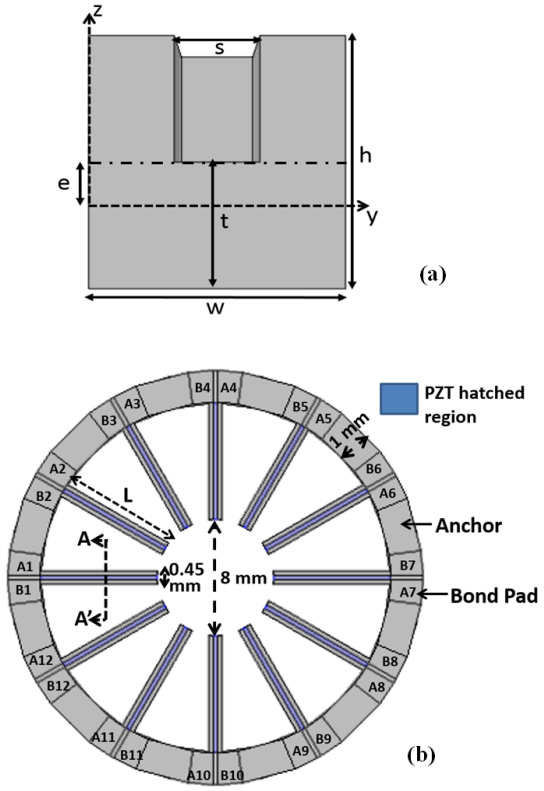

Figure 2.4: (a) Cross-section view of individual PZT bimorph and (b) Lay-out of designed stator.

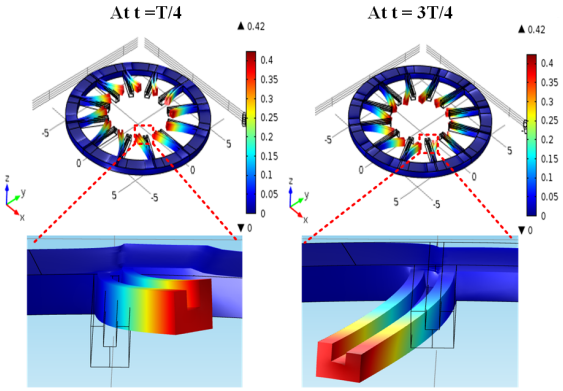

Figure 2.5: COMSOL^{TM} simulation of PZT stator with beam length of $3mm$, for an applied sinusoidal voltage signal of $100Vp-p$ at $25.03kHz$ between A_n set of electrodes and bottom electrode .

approximately follows straight line trajectories in $Y - Z$ plane along trajectory a or b (Fig.2.2). The motion trajectories facilitates to rotate the rotor that is in contact with the stator, in clockwise or counter clockwise direction due to the applied normal and tangential force from the bimorph.

2.3.1 FEM modeling of stator

In order to obtain the resonance frequencies of the bimorphs, eigen-frequency analysis is carried out using finite element analysis in COMSOL^{TM} Multiphysics modeling tool. For the beam length of 3mm, the predominant modes were, bending lateral motion mode at frequency of $25kHz$ and the next mode being an out-of-plane bending mode at $26.6kHz$. Stationary analysis in COMSOL^{TM} is used to capture actuator trajectories at different time instants. The stator is excited with voltage signal on electrodes A_n while the other electrode set B_n is grounded. At $t = 0$, rotor will be at static position because the stator does not produce any deformation at this instant. From 0 to $T/4$ (T is the period of applied sinusoidal signal), the active part of the PZT beam expands longitudinally and contract in transverse direction; therefore, the beam tip moves toward the up and right direction as shown in Fig.2.5. At $t = T/4$ corresponds to maximum deflection. From $t = T/4$ to $t = T/2$, the expanding deformation decreases gradually and at $t = T/2$, it goes back to the initial point. From $t = T/2$ to $3T/4$, due to negative electric field, stress direction will get reversed and the bimorph moves down and left direction as show in Fig.2.5 with maximum deflection at $t = 3T/4$. Then, the contracting deformation of the stator decreases gradually and the beam finally goes back to its initial point ($t = T$). During one cycle, the beam tip produces an 'X'-shaped motion in in $Y - Z$ plane, which can be used to

rotate a rotor in clockwise and counter-clockwise direction.

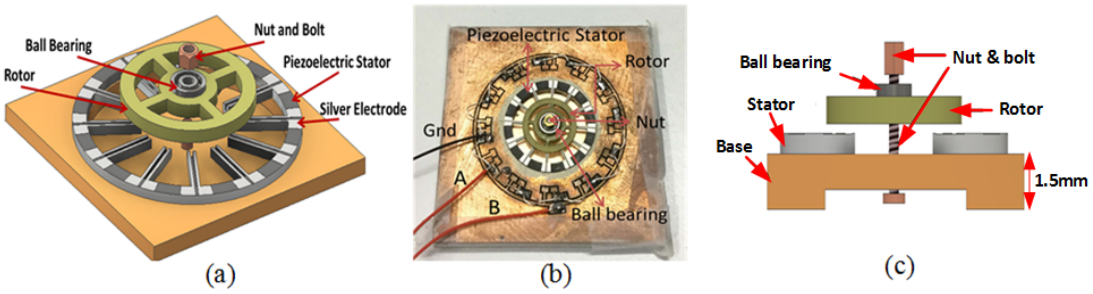

Figure 2.6: (a) 3D sketch of the motor (b) Photograph of the assembled ultrasonic piezoelectric motor (c) Sketch of the cross section of the prototype.

2.3.2 Motor assembly and operation

The piezoelectric stator is bonded using silver acrylic adhesive onto the base PCB to ensure bottom PZT electrode contact. The stator is aligned to the PCB along a laser cut alignment mark. The patterned electrodes on anchors are wire bonded to bond pads on custom PCB as shown in Fig.2.7. A miniature ball bearing (Dynaroll 440C) is bonded at center of the PCB rotor using cyanoacrylate adhesive. The rotor is then assembled on to the stator using miniature nut and bolt, that applies compression of the rotor against the tips of the PZT bimorphs.The sketch and the photograph of assembled motor is shown in Fig.2.6.

Each motor has three input terminals, *A* and *B* terminals that are connected to the top electrodes of piezoelectric stator and a bottom electrode which is the common ground. Operating the motor requires a single AC voltage source to actuate one set of electrode. On applying voltage on terminal *A* we observe clockwise rotor motion voltage, and voltage on terminal *B* for counter clock-

wise rotor motion (Fig.2.2). When an AC voltage is applied to the A terminal and common ground, during positive voltage, active part of PZT will expand longitudinally and also undergo shear whereas the inactive part resists motion which leads to beam bending sideways and upwards as described in Fig.2.2. This results in contact and a lateral force between rotor and stator, causing the rotor to move. During negative voltage, the beams will bend in opposite direction causing loss of frictional coupling with the rotor. The rotor continues rotating for the non-contact time span due to the rotor inertia.

Table 2.2: Dimension of fabricated stators

Length of Beam (L)	Diameter of Stator	Labeled
2*mm*	14*mm*	Type1
2.5*mm*	15*mm*	Type 2
3*mm*	16*mm*	Type 3

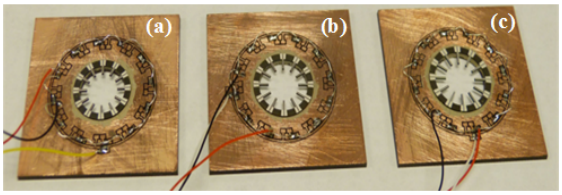

Figure 2.7: Fabricated three different ultrasonic motor stators with (a) 2*mm*, (b) 2.5*mm* and (c) 3*mm* bimorph lengths bonded onto base PCB

2.4 Fabrication Of Stator And Rotor

Ultrasonic stators of three different diameters with varying beam length were fabricated (Table 2.2). The stator PZT bimorph arrays were fabricated out of

commercially available piezoelectric PZT plates, 0.5*mm* thick, and with silver electrodes (APC International, Ltd.). The rotor and the base substrates for the stator were fabricated using laser cutting a 1.5*mm* thick metalized FR4 (PCB material) sheet where the metal is also selectively removed using the laser. The stator and rotor were fabricated using a laser micro-machining process, discussed in detail in [63]. The laser-cutting process enables us to create structures and electrode patterns on bulk PZT by controlling the laser power, beam scan speed, and (hatching) density. The laser patterning of PZT described here is direct-write and monolithic. The laser is also used for partial removal through the thickness of top silver/copper layer, so as to have electrical isolation between the two electrodes. Typical cut rates for PZT are 25μm/min along the PZT thickness. This rate is a result of many factors such as laser beam size (specified to be 25μm at FWHM), material cutting properties, with other recipe parameters such as beam hatching density, power, and pulsing frequency of the laser tool. After laser-micromachining, the PZT structures were cleaned with IPA (Iso-propanol alcohol) to remove the debris formed during laser cutting [63].

2.5 Experimental Results

2.5.1 Stator bimorph characterization

To operate the motor at its fundamental resonance frequency, first the electrical impedance response of the stator at low voltage is measured using an impedance analyzer (HP 4194A). The measured resonance frequency from impedance characteristics for Type 1, Type 2, and Type 3 stator are 47.5*kHz*,

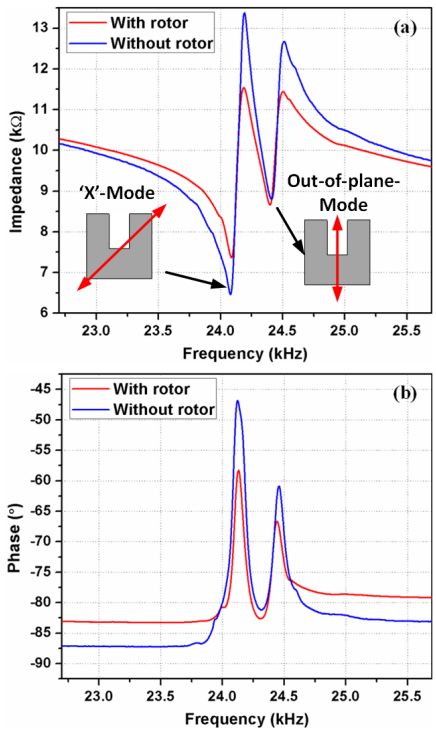

Figure 2.8: Electrical impedance response of Type 3 stator for $0.5V_p$ excitation (a) magnitude response (b) phase response

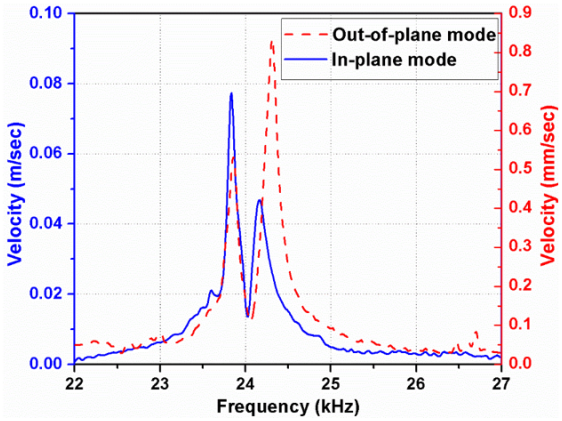

Figure 2.9: Frequency response for the Type 3 stator with in-plane and out-of-plane resonances measured an excitation voltage of $2Vp-p$ measured using Polytec MSA400

$32.6kHz$ and $24.1kHz$ respectively, which is in close agreement with FEM modal analysis. The impedance magnitude and phase spectrum were measured for

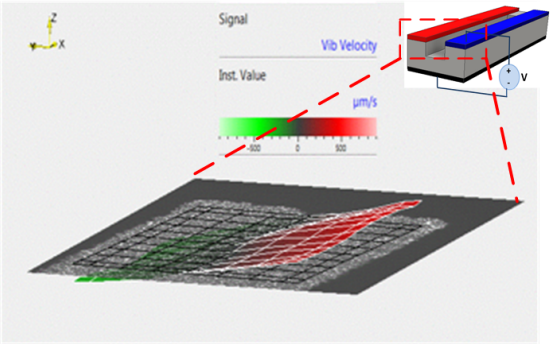

Figure 2.10: Out of plane motion of piezoelectric bimorph measured using Polytec MSA400 at $2Vp-p$ at frequency $23.9kHz$, applied across one top electrode and bottom

different dimensions of the fabricated stator (Table.2.2) and the results for Type 3 motor is shown in Fig.2.8.

The mechanical frequency response is measured using Polytec MSA400 Laser Doppler Vibrometer. The in-plane motion at the tip of piezoelectric beam is measured by stroboscopic technique and out-of-plane motion is measured using Laser Doppler technique. The measurement is done by applying a sinusoidal voltage between one of the top electrode terminal (A_n or B_n) and bottom electrode of piezoelectric stator. The frequency response of Type 3 stator for in-plane and out-of-plane bending mode is shown in Fig.2.9. The vibration mode shape of beam tip is obtained using Laser Doppler vibrometer at $23.9kHz$ for $3mm$ beam length motor, shown in Fig. 2.10. The out-of-plane bending mode shape is in close agreement to COMSOL^{TM} modal analysis. The resonance frequencies for dominant in-plane and out of plane bending modes are $24kHz$ and $24.3kHz$. We observe an out-of-plane mode due to the groove and shear strains excited by electric field E_2, as predicted by FEA. In this motor, the 'X' mode of the stator bimorph generate frictional coupling to the rotor and the in-plane motion provides the lateral momentum to the rotor.

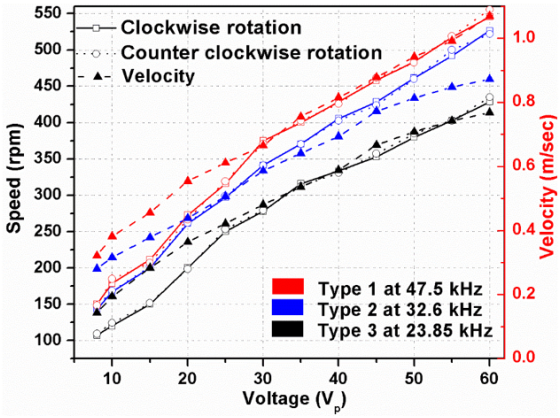

Figure 2.11: Rotor speed and stator bimorph tip velocity versus the applied voltage for different dimension beam length motor.

2.5.2 Ultrasonic motor output characteristics

To measure the rotational speed of each motor, the motors were driven by a sinusoidal voltage signal at their respective fundamental resonance frequencies of the stators. For Type 1, Type 2 and Type 3 stator, the resonance frequencies are $47.5kHz$, $32.6kHz$ and $23.85kHz$ respectively. The rotary motion is observed at $8V_{peak}$ for Type 3 motor. The rotational speed is measured by recording videos of the rotor at varying amplitude of applied AC signal for both clockwise and counter-clockwise motion of the rotor. The velocity for one of the bimorphs of the actuated stator has been measured using in-plane stroboscopic capability of the Polytec MSA400. For different dimension stators, rotor speed and bimorph tip deflection velocity as a function of applied voltage is shown in Fig. 2.11.

The speed of the rotor and tip velocity of piezoelectric beam on the stator increased with the increase in driving voltage at resonance frequency. The minimum speed of $148rpm$, $142rpm$ and $107rpm$ for Type 1, Type 2, Type 3 stator respectively, for a drive voltage of $8V_{peak}$. The motor output performance is nearly the same in both CW and CCW direction with repeatable response for

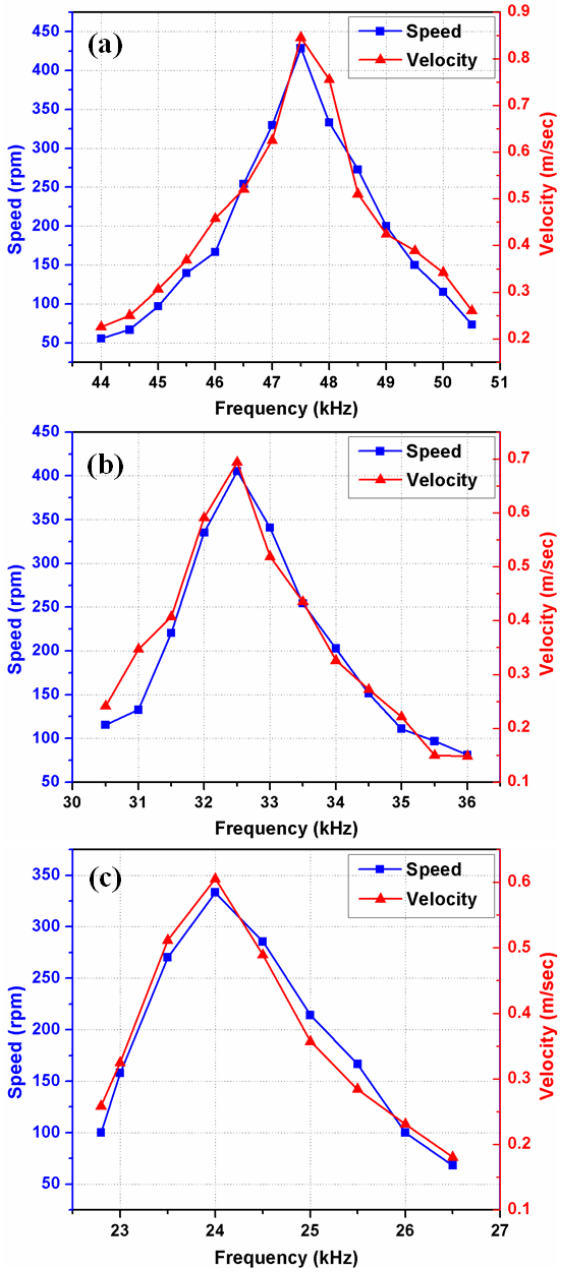

Figure 2.12: Speed vs. excitation frequency at driving voltage of $40V_{peak}$ for: (a) Type 1 motor, (b) Type 2 motor and (c) Type 3 motor.

the resonant drive configuration. The speed of the rotor increased linearly with increase in applied voltage at resonant frequency due to increased strain and actuation velocity of piezoelectric bimorph. A maximum rotation of $545rpm$ is achieved at a drive voltage and frequency of $60V_{peak}$, $47.5kHz$ for the $2mm$ beam

length motor.

The rotor speed and bimorph tip velocity as a function of excitation frequency at a constant drive voltage of $40V_{peak}$ is also measured, for the different types of motor (Table.2.2). The speed of rotor and the vibrating bimorph velocity with different exciting frequencies are shown in Fig.2.12. The speeds of the rotor and the velocities of the bimorph tip followed the same trend as expected and were maximum at the resonance frequency of the motor.

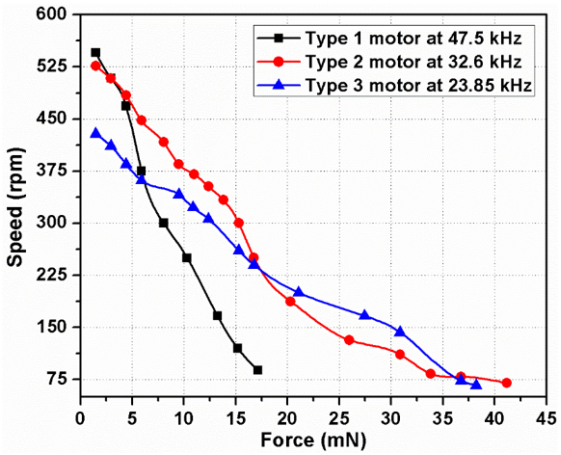

Figure 2.13: Speed vs load at driving voltage of $60V_{peak}$ for different dimension motor at their respective resonance frequency.

To measure the payload handling capacity of the ultrasonic motor, the speed of the motor is measured on incrementally adding additional uniform loads on the rotor. Response of the motor to mass loading is characterized by measuring the speeds of the motor as a function of applied load for the three types of devices (Fig.2.13). The motors were driven at their resonance frequencies with an applied signal of $60V_{peak}$. The load consisted of a 3D printed disc with center orifice to be affixed to the rotor, similar to the assembly shown in Fig.2.6. Additional masses were added on top to measure performance as a function of load. The decrease in speed of motor with increase in payload is different for

each motor. As the load increases the dynamic frictional force between the rotor and stator increases such that the bimorph displacement is decreased for a given drive voltage. Although the resonance frequency of the bimorph is likely to change with loading, it is not measured during the data acquisition.

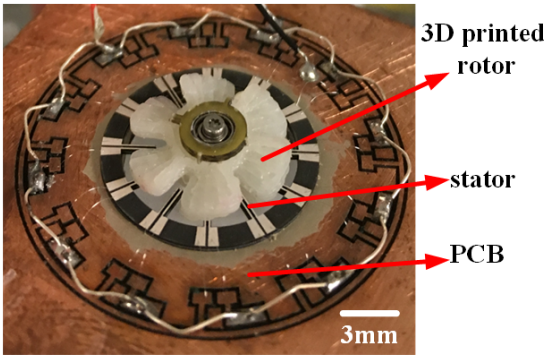

Figure 2.14: Prototype of 3D printer rotor used for operation of a fan application.

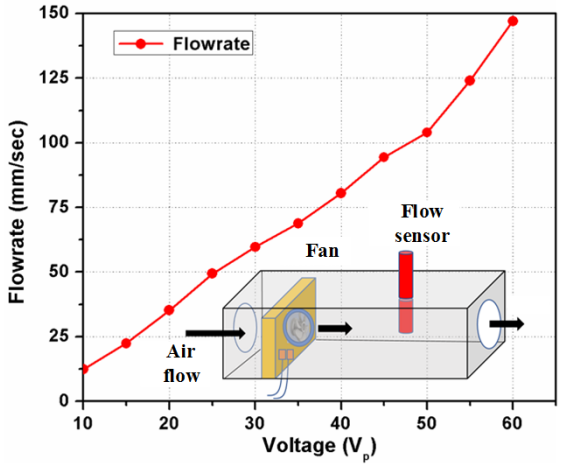

Figure 2.15: Air flow rate as a function of drive voltage of frequency $32.6kHz$ for Type 2 motor. Sketch of the experimental setup is shown in the inset

2.5.3 Application to operation of a fan

The fabricated motor can operate at low voltage of $8V_{peak}$ with speed in the $100-200rpm$ range. The motor has the potential of being used in a wide variety of small scale applications which demand light, small and low profile motor. The performance of the motor working as a mini fan is tested and can be potentially used for heat dissipation in electronic cooling circuits and other applications. The rotor used for this application is a 3D printed fan blade shown in Fig.2.14. The mount and assembly is similar to the one shown in Fig.2.6 with the FR4 rotor replaced with 3D printed ABS plastic fan blades.

A single source voltage supply is used for driving the motor and a flow sensor (FMA 902R- V1) is used to measure the air flow rate. The flow meter is kept near to motor in an enclosed box and when external voltage is applied to motor, the rotor will start rotating and will force air to move. Fig.2.15 shows the air flow rate for $2.5mm$ beam length motor at different driving voltage and achieved maximum flow rate of $165mm/sec$ at driving voltage of $60V_{peak}$.

2.6 Discussion And Conclusions

In this work, a piezoelectric ultrasonic motor was designed, fabricated and tested and was designed using a monolithic lateral U-shaped bimorph. Three different dimension motors were fabricated and their frequency response, speed and payload capacity were characterized. A maximum speed of $550rpm$ was demonstrated at $60V_{peak}$ for a $2mm$ beam length device, with its fundamental resonance frequency of $47.5kHz$. A maximum payload capacity of $4.1g$ at

$60V_{peak}$ was measured for $2.5mm$ beam length stator. The motor performance in a mini fan application was also tested, and measured a maximum flow rate of $165mm/sec$. In future designs, the operation voltage requirements for the motor can be reduced by a factor of 2 by double side electrode patterning of the bimorphs on the stator [63].

CHAPTER 3

MULTI MODAL PIEZOELECTRIC MECHANICAL STIMULI STAGE FOR IN-SITU CALIBRATION OF MEMS GYROSCOPES

3.1 Introduction

MEMS Coriolis force gyroscopes have scale factor and bias errors that are in the order of $10,000ppm$ [65]. The errors are a result of systematic and stochastic noise sources, which limits their use in inertial navigation applications, under GPS-denied conditions. Inertial sensors with bias and scale factor drifts that are $< 10ppm$ are needed for navigation applications [66]. MEMS gyroscopes suffer from scale factor and bias drifts due to aging and environmental conditions such as temperature fluctuations, shock and package stress etc. [67, 68]. Ongoing recent research efforts to enable the use of MEMS inertial sensors for inertial navigation are broadly focused on two main approaches. One approach relies on fabricating precision gyroscopes which are less susceptible to scale factor and bias drifts due to aging and temperature fluctuation [69, 70]. The other efforts have progressed towards in-situ calibration, where the scale factor and bias drifts are extracted during operation while applying known stimuli to the gyroscopes. The in-situ calibration approach can be further classified under the kind of stimuli (electrical and/or mechanical) applied to the inertial sensors. Electronic rate injection relies on applying electrostatic forces, additional control loops, and dedicated electrodes in the gyroscope design for self-calibration [71–73]. The mechanical stimuli approach [74] relies on applying rotation rates via physical platform to the inertial sensor for calibration. This work focuses on the latter approach of applying mechanical stimuli to the gyroscope under test

to extract the scale factor and bias from the input-output characteristics of the gyroscope. For accurate calibration of gyroscope, it is necessary to apply pure mechanical stimulus to the gyroscope under test, ideally with no cross-axis motion coupling. Conventional inertial sensor characterization tools such as rate tables and off the shelf precision motion stages [75,76] are capable of applying pure mechanical stimuli. However, they are bulky and consume power much greater than that of the MEMS sensor. This work introduces an inertial sensor calibration system that is capable of being integrated within cubic-centimeter package.

It is desirable to have precision millimeter scale motion stages, for in-situ calibration of MEMS inertial sensors. A stage that can be used for gyroscope calibration in a compact manner should be planar, have high angular dynamic range, low power, and minimal cross axis coupling for accurate calibration. Several actuators compatible for micrometer to millimeter length scales motion stages with different transduction schemes such as thermal, electrostatic and piezoelectric have been reported [77, 78]. However, conventional micro electrostatic actuators such as comb drives yield smaller forces due to their low electromechanical coupling coefficient (k_{31}). Additionally, surface micromachined electrostatic stages are limited in the dynamic range of motion due to electrostatic gaps. For thermal actuators, the forces are considerably higher, but the high temperatures and power consumption can make thermal actuators impractical for portable applications. Piezoelectric actuators can generate high forces and support high rigidity structures for a given displacement and operate at low powers owing to their high electromechanical coupling efficiencies. Amongst the many piezoelectric materials, PZT (Lead Zirconate Titanate)

is known to have high strain coefficient (d_{31}), which is crucial for the in-plane actuation performance. A common method of fabricating macro-scale PZT actuators such as bimorphs and unimorphs is to bond multiple layers of piezoelectric and elastic materials [79,80] in large sheets, and then cut the sheets into millimeter to centimeter scale plates and beams. However, this approach is not optimal for micro-millimeter scale PZT actuators. Thin film micro fabrication techniques for piezoelectric actuators enable actuators only several microns in thickness achieving small forces. Furthermore, micro-piezoelectric actuators often fail to match the piezoelectric properties and fatigue resistance of the bulk PZT materials [13]. Also, thin film piezoelectric actuators suffer from delamination, non-uniformity, and issues such as stress mismatch between layers, which can lead to deformed structures post-fabrication [81]. Hence, the ability to realize bulk-PZT devices, but at the millimeter to micron scale is desired. Between the bulk-PZT macro-scale actuators realized by bonding, and thin film actuators, the domain of millimeter thick but 100's-micron wide actuators has not been explored for high speed actuation stages.

In this work a monolithic θ_z, X, Y bulk PZT motion stage for in-situ calibration of a MEMS gyroscope is evaluated. For a proof of concept demonstration of gyroscope calibration, a commercially available ADXRS646 Z-axis gyroscope is calibrated after bonding it to the stimuli platform. Calibration is done by extracting the scale factor, bias drifts and gyroscope acceleration sensitivities to within $100ppm$. The calibration stage does not add additional noise. It is demonstrated by measuring the Allan deviation of the gyroscope when the calibration stage is active. The gyroscope calibrated rate output is also compared to the $1ppm$ accurate rate applied by a commercial rate table. For long term stability of the calibration apparatus and to counter for errors from piezoelectric

stage creep and aging, a diffractive optics based stage metrology technique using, Nano Optical Ruler Imaging System (NORIS) [82] is implemented on the stimuli stage. NORIS utilizes a atom stabilized laser wavelength that generates a diffraction pattern that is used for in-situ metrology. Here, a portable, self-contained Diffractive Optics Metrology Enabled Dithering Inertial Sensor Calibration System (DOME-DISC) is demonstrated, which is capable of calibrating MEMS gyroscope die mounted on the stage (Fig.3.1(a)).

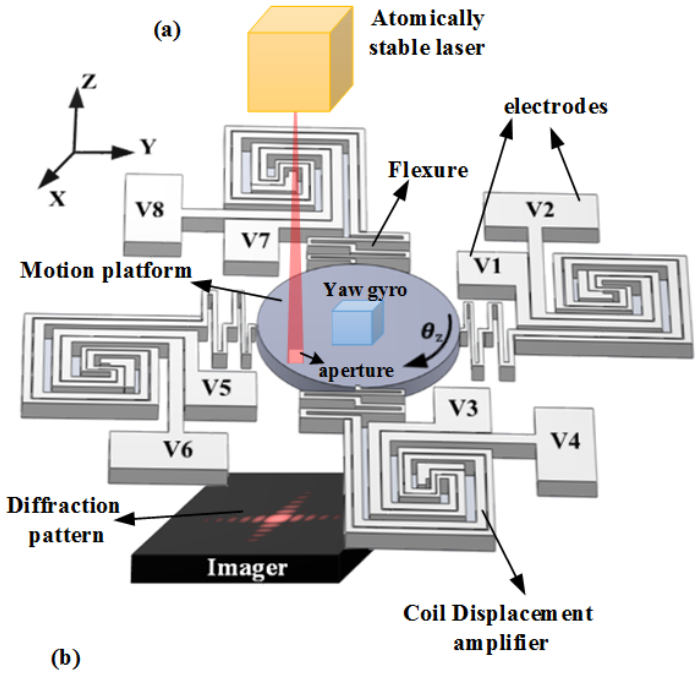

(b)

Motion	V1	V2	V3	V4	V5	V6	V7	V8
X	-V	-V	+V	-V	+V	+V	-V	+V
Y	+V	-V	+V	+V	-V	+V	-V	-V
θ_z	+V	-V	+V	-V	+V	-V	+V	-V

Figure 3.1: (a) 3D schematic of DOME-DISC consisting of a monolithic bulk PZT multi-modal stage with integrated diffraction aperture for optical metrology and a atomically stable laser source. (b) The modes of operation of the stage controlled by changing the polarities of the voltages on the 8 electrodes.

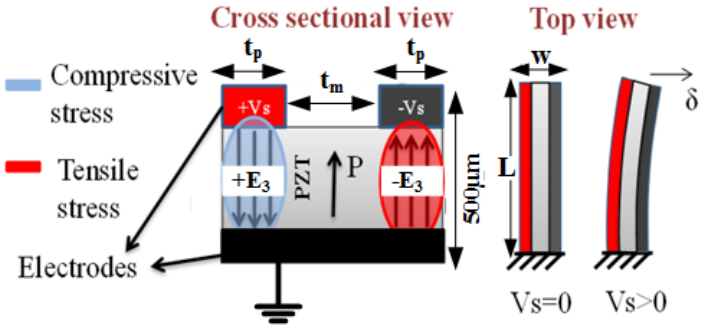

Figure 3.2: The lateral PZT bimorph actuator which is the building block of the coil displacement amplifier for actuation of the stage.

3.2 Multi Modal Piezoelectric X Y θ_z Stage for Z-axis Gyroscope Calibration

3.2.1 Stage design and operation

In order to achieve the stage constraints such as being planar, have high angular dynamic range, low power consumption, and minimal cross axis coupling, one approach is to monolithically integrate motion platform, planar flexures and in plane actuators that have linear actuation as a function of applied voltages. Fig.3.1(a) shows a monolithic mechanical stimuli stage that consists of bending actuators, flexures and motion platform all fabricated out of a single 500μm thick PZT-4 plate using the laser micromachining process [16]. The stage has high aspect ratio components (width to height of 1:5) with 100μm minimum feature size. The fundamental building block of the stage is an in-plane lateral bimorph (Fig.4.2). The lateral bimorph provides linear in-plane motion as a function of drive voltage, with low cross axis motion coupling. The details of the lateral PZT bimorph are discussed in detail in [16]. The tip deflection of such a bimorph

with length L, width w and thickness h with electrode width t_p and width of the region with no electrode t_m is given by,

$$\delta = \frac{\kappa L^2}{2} \tag{3.1}$$

where κ is the curvature of the bimorph, can be written as,

$$\kappa = \frac{12 d_{31} E_3 (t_m t_p + t_p^2)}{2(3t_m^2 t_p + 6t_m t_p^2 + 4t_p^3) + t_m^3} \tag{3.2}$$

where $E_3 = V_d/h$ is the applied electric field, with drive voltage on PZT bimorph electrodes V_d along the thickness h. Series and parallel combinations of the lateral PZT bimorph actuators can be monolithically integrated to achieve a displacement amplifier [83, 84]. The coil/spiral shaped displacement amplifiers with lateral in-plane bimorphs are connected such that they increase the total actuation of the spiral. The motion of the sprial actuators are coupled to a central rotor platform carrying the payload (inertial sensor) via planar, hinge-like springs [85]. However, an out-of-plane motion is also generated due to the shear stress along the thickness of the beams and the Poisson's effect. S-shaped springs were designed in order to maximize transmission of the displacement to the central rotor from the spiral actuators, while also minimizing the undesired out-of-plane motion. The S-shaped springs behave as planar hinges and facilitate in-plane rotation and translation while maintaining the stiffness to cross-axis motion during the desired in-plane dither [86, 87]. One of the undesired consequences of the S-shaped springs is to reduce the rigidity and lower the resonance frequency of the stage. The motion of the stage is a function of applied voltage and has multiple degrees of freedom (X, Y, θ_z) owing to the several control electrodes. The coil-shaped bimorph either bends right, left or expands/contracts along its length causing different modes of bending possible. On changing the polarities of the voltages on these 8 electrodes X, Y, θ_z motions can

be achieved as shown in Fig.3.1(b), Fig.4.2. The angular rate (Ω_z) can be controlled precisely by changing the frequency at a fixed voltage to circumvent the strain hysteresis errors in PZT.

3.2.2 Insitu calibration approach

A typical gyroscope response, with and without applied rate is corrupted by errors such as stochastic scale factor variation, bias drift, acceleration sensitivities and flicker noise. The gyroscope rate can be can be modeled as,

$$\Omega_{gyro} = \frac{1}{SF_g(t,T)}\left(V_\Omega(t,T) + V_{aging} + V_{bias}(t,T) + V_\epsilon\right) + \frac{1}{SF_{am}(t,T)}\left(V_{a_c} + V_{a_t}\right) + \frac{1}{SF_{ae}(t,T)}(V_{a_e}) \tag{3.3}$$

where, V_Ω is the voltage induced by the applied rate, V_ϵ models for stochastic noise and flicker floor. A gyroscope is also sensitive to accelerations, which include the external linear acceleration a_e, centripetal and tangential accelerations a_c and a_t experienced by gyroscope due to mount induced errors when the gyroscope is mounted off axis of rotation in the package or the calibration stage. Quantities SF_g, SF_{am} and SF_{ae} are the gyroscope scale factors for rate, mount induced acceleration and external acceleration along gyroscope sensitive axes respectively. The acceleration sensitivity of the gyroscope causes undesirable voltage signals V_{a_c}, V_{a_t} and V_{a_e}. The scale factors vary with time t and temperature T and have to be extracted along with the bias drift for in-run correction.

The goal of an ideal calibrator is to extract all of the above scale factors and bias errors. The extraction procedure consists of the following steps. When

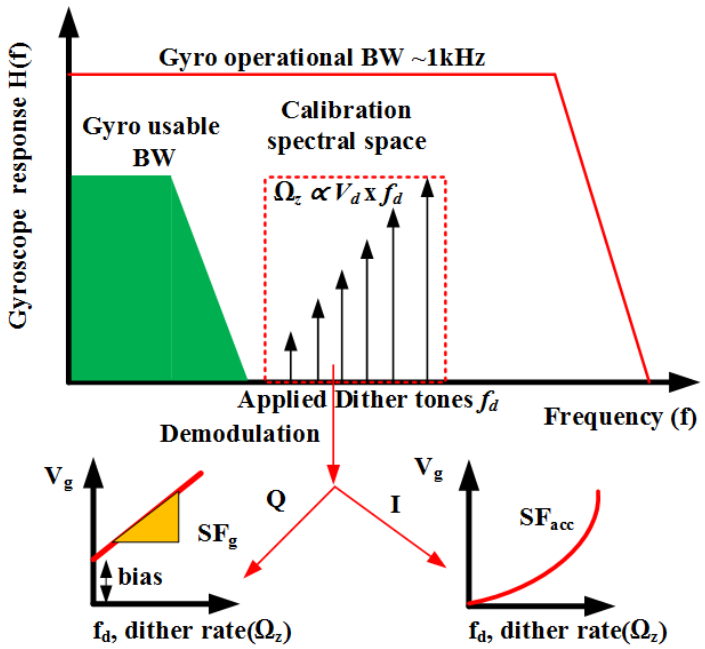

Figure 3.3: Gyroscope calibration approach where the scale factor, bias and acceleration sensitivities are extracted on applying dither rates (Ω_z) at high frequencies ($50 - 500Hz$), while the gyroscope is in operation at lower bandwidths

a voltage V_d is applied in the dither mode configuration (Fig.3.1(e)) at dither frequency ω_d, the stage generates a dither angle θ_z given by,

$$\theta_z(t) = \theta_0 cos(\omega_d t) \tag{3.4}$$

The corresponding angular dither rate is,

$$\Omega_z(t) = -\theta_0 \omega_d sin(\omega_d t) \tag{3.5}$$

The angular acceleration experienced by the gyroscope is,

$$a_\omega(t) = \frac{d\omega_z(t)}{dt} = -\theta_0 \omega_d^2 cos(\omega_d t) \tag{3.6}$$

Assuming that the gyroscope is placed off the center by an offset ΔR, the

tangential acceleration experienced by the gyroscope is

$$a_t(t) = a_\omega \Delta R = -\theta_0 \omega_d^2 \Delta R cos(\omega_d t) \tag{3.7}$$

The centripetal acceleration experienced by the gyroscope is,

$$a_c(t) = \Omega_z^2 \Delta R = \frac{\theta_0^2 \omega_d^2 \Delta R}{2}(1 - cos(2\omega_d t)) \tag{3.8}$$

In this approach of in-run calibration, the gyroscope spectrum is divided into gyroscope usable bandwidth near baseband ($0 - 10Hz$) and calibration spectral space ($20 - 400Hz$). On applying mechanical dithering in the calibration frequencies, known rates ($\Omega_z(f_d)$) are applied for calibration purposes, while the gyroscope is functional at low frequencies for sensing external rate (Fig.3.3). The piezoelectric stage applied rate is a function of frequency (f_d) and voltage (V_d) to stage. On sweeping frequency f_d of the sinusoidal voltage input to the PZT stage, with a constant drive voltage (V_d), rate (Ω_z) is applied at different frequencies as illustrated in Fig.3.3. The scale factor and acceleration sensitivity are obtained from I-Q demodulation of gyroscope voltage at the dither frequencies (Eqns(3),(5),(7)). Since the dither angles are small and $\theta_0^2 << \theta_0$, contributions from a_c on gyroscope output is negligible. Due to the phase relationship between acceleration and rate terms as shown in Eqns(5)-(7), the acceleration and rate sensitivities are decoupled and the former is canceled.

The scale factor extracted from the dither-demodulation approach at different frequencies is free from baseband noise sources such as flicker, earth rate and slow varying bias. The scale factor measured in the calibration spectrum is applicable for baseband measurements as the scale factor of the gyroscope is typically independent of frequency before the first pole of the gyroscope response ($1kHz$) (ADXRS646 datasheet). Also, on using the $X - Y$ mode of the

PZT calibration stage (Fig.3.1(b)) the gyroscope sensitivity to linear in-plane accelerations can be measured. On sweeping the frequency f_d at constant drive voltages, the gyroscope response to applied in-plane accelerations (a_e) along the gyroscope sensitive axes can be measured.

3.3 Nano Optical Ruler Imaging System For PZT Stage Metrology

In PZT actuators, strain as a function of applied voltage is non linear demonstrating a hysteretic behavior [88]. The hysteresis can cause rate and acceleration repeatability errors in the PZT calibration stage. In order to minimize this error, the bimorph actuators are operated at fixed electric field and the frequency of the applied voltage is varied for stage rate and acceleration control. Additionally, PZT suffers from creep and polarization aging when operated for long term at constant electric fields [88, 89]. Some dipoles in PZT will continue to move slowly by a displacement Δx and reorient differently from the original position Δx_0 under applied electric fields at long time t, expressed as,

$$\Delta x(t) = \Delta x_0 \left(1 + \gamma log \frac{t}{t_0}\right) \tag{3.9}$$

where γ is the creep factor. For example, Δx can be $\approx 0.5 - 1\%$ after several days of operation. This systematic aging requires correction.

To be able to calibrate the errors in gyroscope, the calibration apparatus should not age or drift in the short term timescales of the gyroscope. It is desirable to have a long term stable calibrator which can correct for short term

gyroscopic errors for stable short term (30 minutes) operations. An atomically stable laser whose wavelength (λ) is locked to an atomic transition that does not age with time and temperature [82]. One way of using such an atomically stable system is to form an optical ruler, like the ones used in optical encoders, but here with a square diffractive aperture of side d formed on the stage. The diffraction pattern obtained on an imager by reflection or transmission (Fig.3.1(a),(d)) can be used to measure motion. A laser beam of intensity I can undergo diffraction through a square aperture can produce a diffraction pattern that can be written as,

$$I(x,y) = I_0 sinc^2\left(\frac{dx}{\lambda z}\right) sinc^2\left(\frac{dy}{\lambda z}\right) \tag{3.10}$$

The pattern consists of maxima and minima of intensities. The separation of the orders (maxima) of the diffraction pattern k can be approximated as,

$$k = \frac{\lambda z}{d} \tag{3.11}$$

In the expression above, I_0 is the peak intensity of the 0^{th} order and z is the distance between the imager and the grating. A square aperture is formed on the stage using laser micromachining, which is used as a transmission grating as shown in Fig.3.1(a),(d). To the first order it is essential to have stable wavelength to cancel the temperature induced errors in the diffraction pattern image due to thermal expansion and contraction of aperture and other optical components. Temperature induced errors alter the separation of the orders ($k + \Delta k$). Since the diffraction pattern for the square aperture is a known function given by Eqn(10), any deviation from the known pattern can be detected using image processing and can be compensated. In-plane stage motion corresponds to translation of

the entire diffraction pattern which can be detected using sub-pixel image registration algorithms [90] applied to the diffraction pattern images. The algorithm compares each image frame of the diffraction pattern off the stage with the initial pattern before motion to calculate the stage position, angular rate and acceleration. The subpixel interpolation algorithm computes the upsampled cross-correlation of the diffraction pattern images, by zero padding the and FFT (Fast Fourier Transforms) to detect shift in the peaks (orders of diffraction pattern) during translation and rotation. With subpixel interpolation, shifts corresponding to $1/N^{th}$ ($N <= 100$) of a pixel can be determined. This accuracy is a result of cross correlation algorithm applied to the highly correlated images during dithering. This technique has been used to resolve motion upto $1/100^{th}$ of a pixel ($\approx 20nm$) [82].

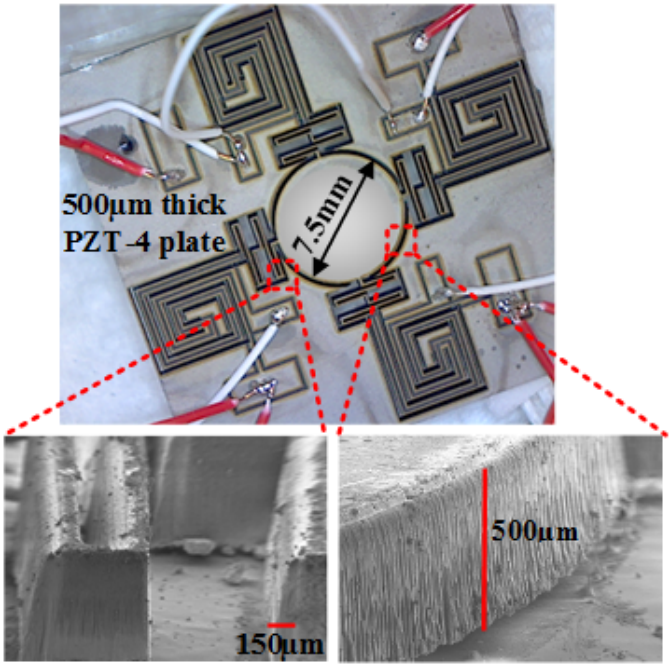

Figure 3.4: Bulk PZT calibration stage fabricated using the laser micromaching process. The SEM images of the sidewalls are in the inset

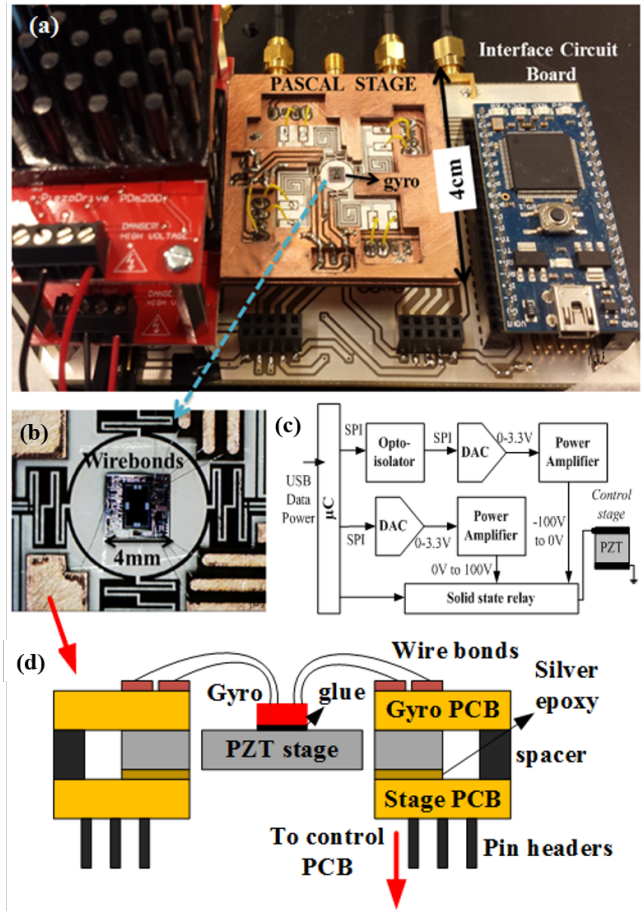

Figure 3.5: Gyroscope calibration system (DOME-DISC) (a) Photograph of the system (b) Picture focusing on the gyroscope (ADXRS646) mounted on the stage and wire bonded (c) Control schematic (d) Cross section of the custom DIP implementation for bulk PZT stage and gyroscope under test

3.4 Fabrication, Assembly And System Implementation

The bulk PZT calibration stage is fabricated using a laser micromachining process [16] on PZT4 Plate (PZT841) from American Piezo Ceramics. The process is a subtractive process and by using direct-write micro patterning technique, precision removal of PZT and/or electrode material. Double-sided (top-bottom) alignment is possible with front-back alignment marks. Actuators, flexures and

displacement amplifiers are formed monolithically by patterning top and bottom electrodes in addition to cutting through PZT. One can realize a wide variety of stages for desired stage motion. One of the fabricated stages is shown in Fig.3.4 with SEM images in the insets imaging the side walls of the highlighted regions. The stage is confined to a 25 x 25mm, 500μm thick PZT-4 plate. The minimum feature that can be patterned through the 500μm thick PZT is 70μm. With the laser beam size of 25μm and the control of cutting parameters such as scan speed and hatch density, limit through cuts to form features smaller than 70μm, but can be improved with a laser with smaller spot size. The typical linear cut rates for PZT are 16.6$\mu m/min$ and each stage can be fabricated in $\approx$ 2hrs. After the laser cutting, the device is cleaned in iso-propyl alcohol and cleaned with cotton swabs to clear off surface debris.

After fabrication, the stage is assembled and connected to a custom PCB as shown in Fig.3.5(a). The the stage is bonded using silver acrylic onto a custom DIP package which is laser cut out of a PCB. The commercial gyroscope die is mounted using an adhesive (3M CA-7) at the center of the stage, onto laser defined alignment marks formed during stage fabrication. As illustrated in Fig.3.5(b), the DIP package assembly has signal routing for wire-bonded gyroscope pins on the top layer and a separate bottom layer for routing PZT calibration stage control electrodes. The two PCB layers are separated by a spacer and the DIP package has standard pin headers which connect to the control PCB. The control PCB houses high voltage amplifiers to drive the PZT actuators generating up to 100V_p sinusoids. Stage control, gyroscope signal acquisition, and control are achieved by a Mbed microcontroller (NXP LPC1768). The PZT stage control electronics also includes digital switch matrix for digital switching control between X, Y and θ_z modes. The power consumed by the bulk PZT stage

can be written as,

$$Power = 2\pi f C tan(\delta) V_d^2 \tag{3.12}$$

For the bulk PZT-4 stage capacitance C is $1.1nF$, the dissipation factor $tan(\delta)$ is 0.6. The PZT stage consumes a power of $13mWatts$ for drive voltage V_d of $100V_p$. The overall system along with power amplifiers, DACs, microcontroller and switches on custom PCB has dimension of 12.7x7.6x10cm and consumes $396mWatts$ power. The gyroscope filter capacitors were chosen to test the gyroscope at high system bandwidths of up to $800Hz$.

3.5 Measurement Results

The components of DOME-DISC are characterized in this section. The unloaded and gyroscope loaded stage performances are first evaluated. Next the stage metrology using NORIS is demonstrated and its performance is compared with a commercial tool from Polytec Inc. The gyroscope calibration using DOME-DISC is discussed and the calibrated gyroscope rate output is compared to the applied rate by a precision rate table. Lastly, the stability of DOME-DISC components are measured.

3.5.1 Characterization Of bulk PZT calibration stage

Optical characterization of unloaded PZT stage at low operation frequencies

Using optical stroboscopy capability of Polytec MSA400, the unloaded stage angular (θ_z) and in-plane ($X-Y$) motion is measured as a function of drive fre-

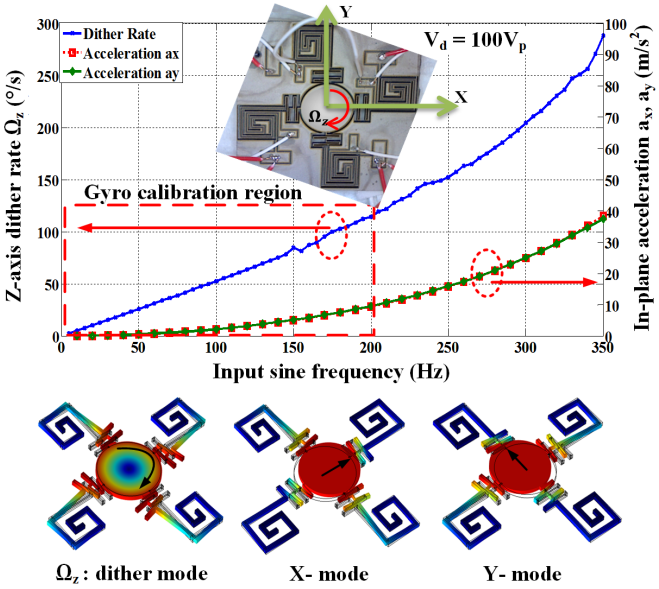

Figure 3.6: Optical characterization of the dither rate (Ω_z) and in-plane acceleration (a_x, a_y) sensitivity of the stage using Polytec MSA400. COMSOL^{TM} simulation of stage motion for the X,Y and θ_z modes of operation of the stage are also shown.

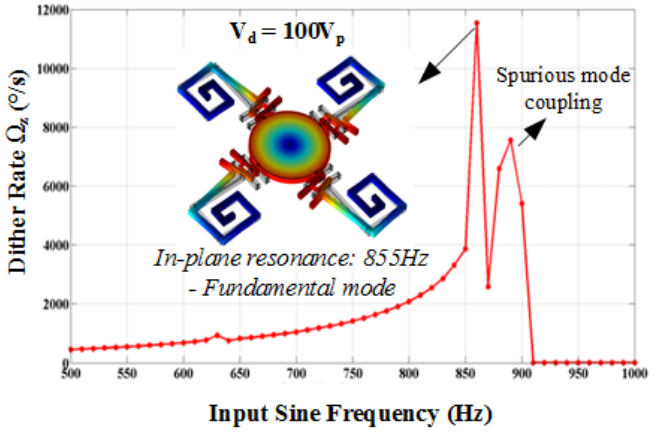

Figure 3.7: Mechanical frequency response of the stage measured using Polytec MSA400, showing maximum dither rate (Ω_z) achievable at resonance before failure. COMSOL^{TM} simulation of the mode shape is also shown

quency, at a fixed drive voltage of $100V_p$. Digitally controlled relays were used to switch between different stage motion modes.The stage motion for each mode

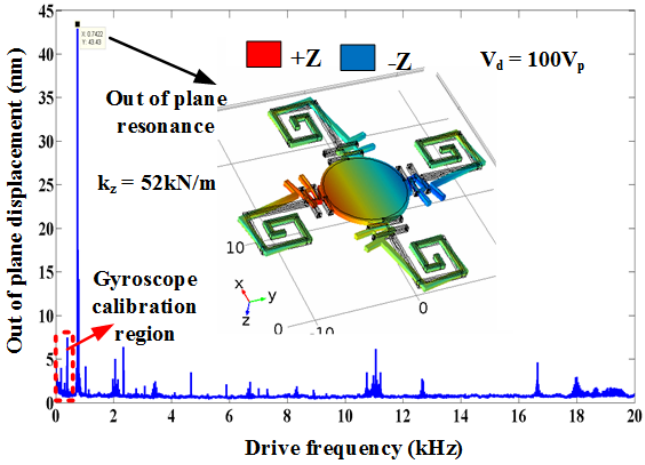

Figure 3.8: Cross axis motion (along Z) sensitivity of the stage when operated in dither mode (θ_z) as a function of drive frequency at $100V_p$ drive voltage. Measured using Polytec MSA400

is shown in Fig.3.6. For the gyroscope calibration, the stage is operated in the $0-200Hz$ frequency range, where the stage dither response is linear. The unloaded stage dither mode sensitivity is $0.89deg/s/Hz$ in the linear region. The peak displacement in dither mode is measured to be $7.1\mu m$ at low frequencies with drive voltage of $100V_p$. The dither response is non-linear at higher frequencies as we approach the fundamental resonance mode of the stage. The in-plane acceleration sensitivity is $\approx 0.3\times10^{-3}m/s^2/Hz^2$ for the frequency range $0-200Hz$. The peak linear (X-Y) displacement is measured to be $8.2\mu m$ at low frequencies with drive voltage of $100V_p$.

Mechanical resonance response of the unloaded PZT stage

The PZT stage is operated in the θ_z mode to measure the in-plane resonance. The fundamental dither mode (θ_z) of the stage, measured using Polytec MSA400 is shown in Fig.3.7. A maximum dither rate (θ_z) of $\approx$ $11,000deg/s$ for $100V_p$ at

the stage fundamental resonance frequency of $855Hz$ is measured. The in-plane dither mode shape is simulated in COMSOL^{TM} and the resonance frequency of the dither mode is in agreement with the results from the finite element model. The stage fractured for $100V_p$ drive at resonance due to excessive strain. A spurious peak measured after resonance can be attributed to the fracture.

For a gyroscope calibration stage, cross-axis motion while operating in desired in-plane dither motion has to be minimized. Any cross-axis stage motion will contribute to the gyroscope output due to gyroscope sensitivities in the motion axis (Eqn(3)). Using a laser doppler vibrometer (Polytec MSA400) the stage out-of-plane motion is measured during desired in-plane dither, as a function of drive frequency at a fixed $100V_p$ drive (Fig.3.8). For calibration of the gyroscope, the stage is operated in the frequency range of 0 to $200Hz$ to achieve the dynamic range of $\approx 200deg/s$ for the ADXRS646 gyroscope. In this frequency range a maximum out-of-plane motion of $3nm$ for a desired in-plane motion of $7.1\mu m$ is measured at $100V_p$ drive. The cross-axis z motion error in the calibration frequencies for the stage is $< 5ppm/V$. Low z motion coupling is enabled by the high out-of-plane spring constant of k_z = 52kN/m. The maximum out-of-plane (z) motion of $44nm$ is measured at the out-of-plane resonance frequency of $742Hz$ (Fig.3.8). The z motion corresponding to $\approx 1000ppm$ of undesirable cross-axis motion. The COMSOL^{TM} simulation of the out-of-plane tilt mode is also shown.

Frequency response of bulk PZT calibration stage on loading the gyroscope

The gyroscope loading effect on the stage motion after adhesively mounting and wire-bonding the gyroscope onto the stage is also measured. Fig.3.9 shows the

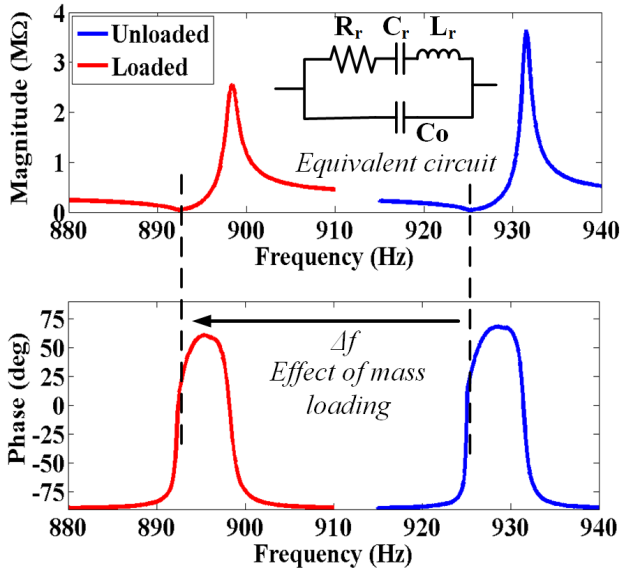

Figure 3.9: Impedance response of the stage measured using HP4194A impedance analyzer for unloaded and loaded (with gyroscope mounted and wire bonded) cases

impedance response of the stage for the loaded and unloaded case. On loading the stage with gyroscope die and wire bonding, the resonance frequency of the stage shifted by $33Hz$. An equivalent circuit model for the unloaded stage is summarized in Table.3.1. Using optical stroboscopy capability of Polytec MSA400, a reduction of 13.5% in dither rate sensitivity is measured due to mass loading as shown in Fig.3.10. The loaded stage dither rate sensitivity is $0.77deg/sec/Hz$. On loading the stage with the gyroscope, the stage still has the desired linear stimuli response to the input frequency at a fixed drive voltage, enabling computationally less intensive approach for the in-situ high bandwidth gyroscope calibration.

Table 3.1: Parameters from equivalent circuit model of the unloaded stage for drive voltage of $500mV_p$

Parameter	Value
C_0	$361.9pF$
R_r	$34.4k\Omega$
C_r	$4.6pF$
L_r	$6.45kH$
$Q = 2\pi f_r L_r / R_r$	≈ 1000
f_r(resonance)	$925.2Hz$
f_a (anti-resonance)	$931.5Hz$
$k_{31} = \sqrt{\left(\frac{f_a}{f_r}\right)^2 - 1}$	11.7%

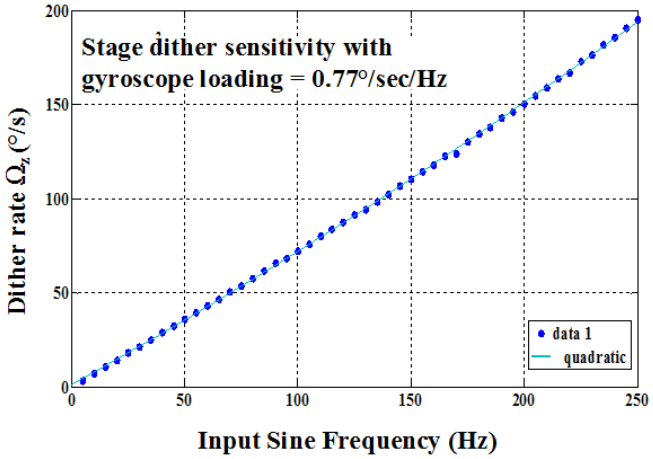

Figure 3.10: Dither rate sensitivity (Ω_z) of bulk PZT stage after the gyroscope is mounted on stage and wirebonded, measured using Polytec MSA400

3.5.2 NORIS results

For the gyroscope calibration, DOME-DISC is operated without NORIS, once the PZT stage sensitivity is initially measured. To compensate for long term

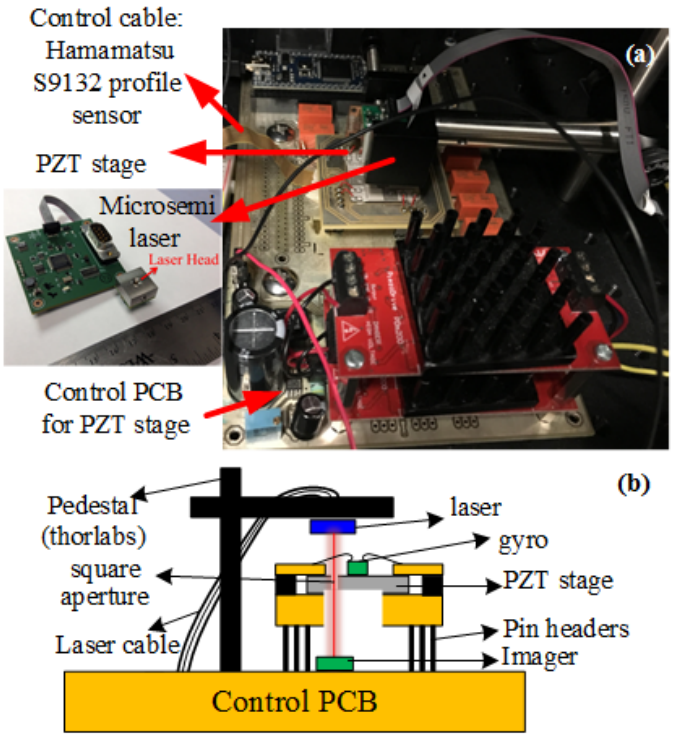

Figure 3.11: NORIS experimental setup (a) Experimental setup showing the atomically stable laser source (ASLS) mounted on top of the PZT calibration stage PCB with profile sensor at the bottom (b) Shows the sketch describing the experimental setup

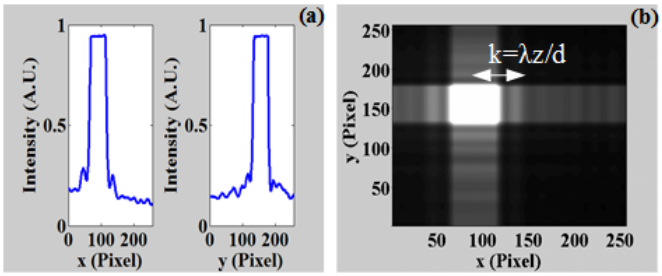

Figure 3.12: Readout from image sensor (a)Plots showing capture of the 1D diffraction pattern by the X and Y pixels of the Hamamatsu profile sensor (b) 2D plot showing the spatial reconstruction of the captured diffraction pattern

aging in the PZT calibration stage (over days - Eqn(9)), NORIS can be used for optical metrology of the PZT calibration stage to extract the new stage sen-

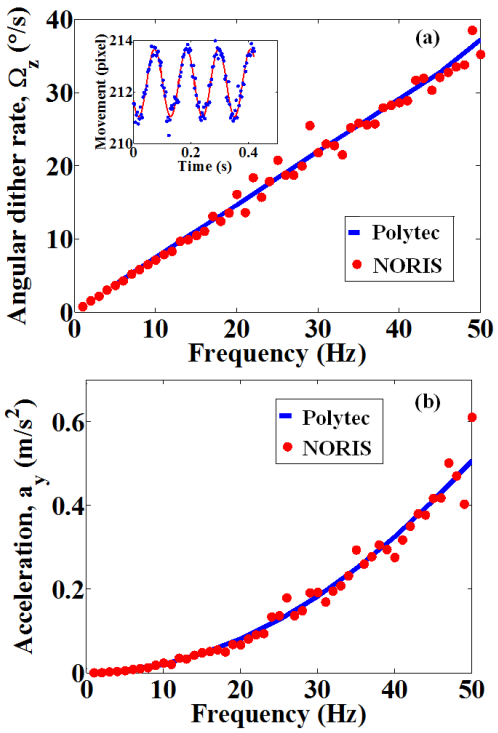

Figure 3.13: Comparison of measurements from NORIS and Polytec MSA400 for (a) In plane dither as a function of PZT stage drive frequency at $100V_p$ drive voltage. Plot in the inset shows the dither as a function of time captured by NORIS. (b) In plane acceleration along Y as a function of dither frequency for $100V_p$ PZT stage drive voltage

sitivity. To demonstrate the performance of the Nano Optical Ruler Imaging system (NORIS), an experimental setup is assembled as shown in Fig.3.11(a). The schematic of this setup is as illustrated in Fig.3.11(b). On shining the atomically stable wavelength laser (from Microsemi) onto the laser cut square aperture ($50\mu m$ side) on the stage a diffraction pattern is captured on the imager as shown in Fig.3.12(a), (b). The spacing between the 0^{th} and 1^{st} order (Eqn(11)) is measured to be $0.312mm$ when the imager is at a distance of $\approx 23mm$ from the square aperture. Using sub-pixel interpolation algorithm [90] on the acquired diffraction pattern images, the stage motion as a function of applied frequency can be measured. The algorithm is currently implemented in MATLAB. Using

NORIS, w the stage dither rate (Ω_z) and in-plane acceleration (a_y) is characterized as a function of drive frequency for a constant $100V_p$ drive voltage amplitude. As shown in Fig.3.13 the NORIS measurement of Ω_z and a_y are in close agreement to Polytec MSA400 measurements for low frequencies of operation. The deviation at higher frequencies can be attributed to image sensor and readout electronics noise. At imager frame rates $> 20 frames/sec$ to capture high frequency dither motion, the ADC on the image sensor operates in 8 bit mode (limited bits) with dark voltage $\approx 50mv$ (Hamamatsu S9132 datasheet) which adds to the intensity error in diffraction peaks

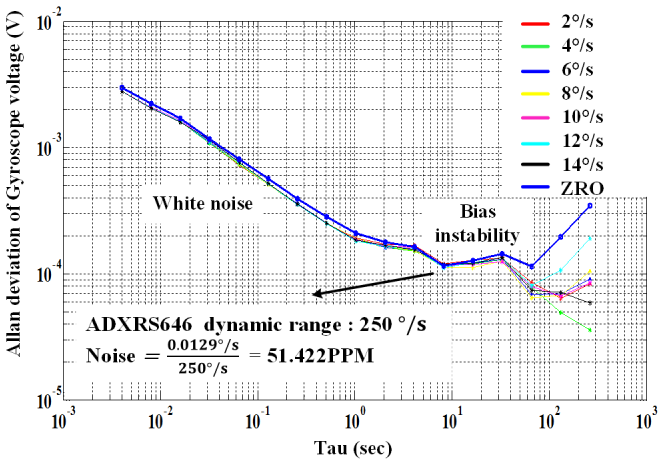

Figure 3.14: Allan deviation of ADXRS646 gyroscope voltage measured at different $1ppm$ accurate rates applied by Acutronics rate table

3.5.3 Gyroscope calibration results

Allan deviation of ADXRS646

The gyroscope under test (ADXRS646) has different error sources that are often characterized by the Allan deviation measurement [91]. The common noise

sources measured using the Allan deviation of the gyroscope output voltage signal are white, flicker noise, and temperature or package stress induced rate random walk at longer averaging times [92]. White noise in the gyroscope output is reduced on averaging, until we are fundamentally limited by the flicker noise for the gyroscope. Fig.3.14 is the measurement of Allan deviation of the ADXRS646 gyroscope output voltage. The Allan deviation for zero rate output (ZRO) condition as well as a the Allan deviation of gyroscope voltage is measured at constant applied rates from a $1ppm$ accurate rate table (Acutronics). The gyroscope white and flicker noise are nearly invariant to applied rate. The lowest noise achievable from the gyroscope rate measurement is $51ppm$ ($\approx 40deg/hr$) at averaging time of $\tau = 20s$. The measurement precision is fundamentally limited by the bias instability of the gyroscope. However the Allan variance for $tau > 30s$ increases for certain applied rates. Therefore, all the rate measurement henceforth are averaged for $20sec$ to achieve lowest possible noise.

Comparison of DOME-DISC with rate table

The scale factors obtained from DOME-DISC and a commercial rate table (Ideal Aerosmith 1270VS) are compared. Fig. 3.15 show the scale factor match between the dither-demodulation approach and the conventional rate table to within 1% error. This deviation is because the rate table has a rate repeatability error of $1000ppm$ (Ideal Aerosmith 1270VS data sheet) and mount induced acceleration errors in the gyroscopes were not compensated. As discussed in section $II.B$, a Z-axis gyroscope is also responsive to external accelerations, as shown in Eqn(3). The in-plane X-Y acceleration sensitivity of the gyroscope is measured using the stage X-Y mode to apply different in-plane accelerations a_x and a_y to

extract the gyroscope sensitivity to external accelerations. The sensitivity to a_x and a_y is measured to be $0.44 deg/s/g$ and $3.26 deg/s/g$ respectively as shown in Fig.3.16. The worst case in-plane cross-axis acceleration sensitivity is calculated to be 13.64%.

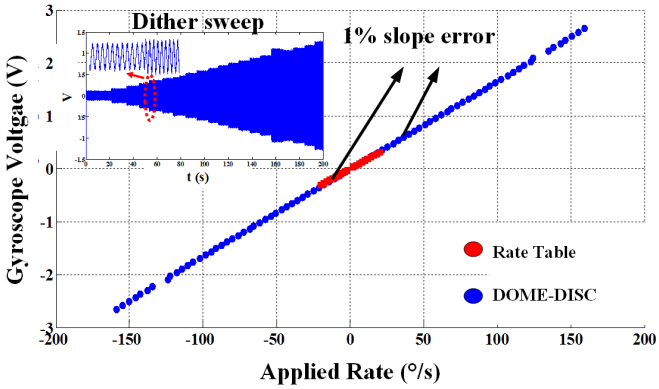

Figure 3.15: Comparison of scale factor (SF_g) measurements from PZT calibration stage and a commercial rate table (Ideal Aerosmith 1270VS) Time domain response of gyroscope to PZT stage rate sweep shown in the inset

To check for the repeatability of DOME-DISC calibration its performance is compared with a $1 ppm$ accurate industry standard rate table (Acutronics BD122) for 10 hours. The comparison is done by correcting the gyroscope rate error, with the instantaneous scale factor, bias drift and acceleration sensitivities obtained from DOME-DISC. While the rate table rates were applied to measure the input-output response of the gyroscope near DC, dither tones is simultaneously applied at higher frequencies using DOME-DISC. As shown in Fig.3.17(a), using the dither-demodulation approach, we were able to repeatedly extract the scale factor ($SF_g \approx 8.9 mV/deg/s$), bias ($2mV$) and cancel the mount induced acceleration errors by I-Q demodulation of the gyroscope response to dither tones (Fig.3.3, Eqns(3),(5),(7)). Since the input-output responses of the gyroscope were measured simultaneously using both the approaches, we can assume that the

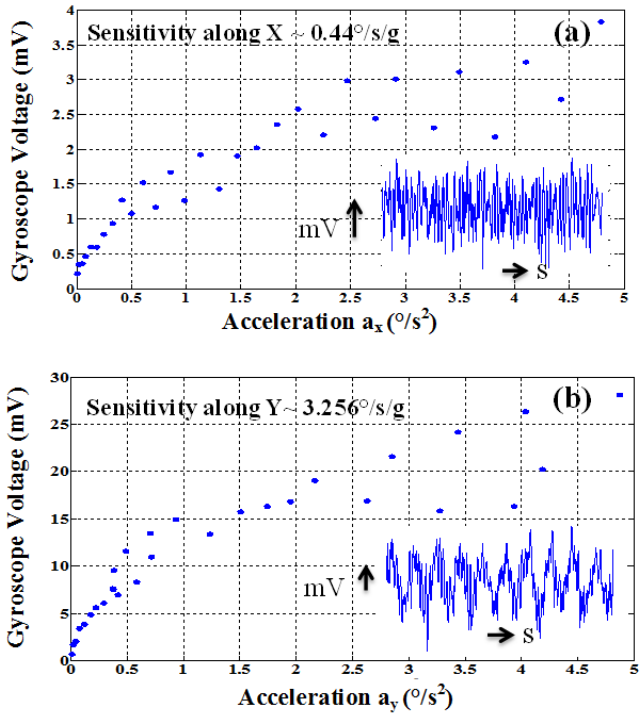

Figure 3.16: Gyroscope sensitivity to in-plane cross axis acceleration (a) a_x along X axis and (b) a_y along Y axis

tests were done under the same environmental conditions. Each rate is applied for $\tau = 30s$ for averaging the white noise to achieve lowest possible noise in each measurement. The response of the gyroscope to rate table applied DC rates were obtained by low pass filtering the gyroscope voltage to remove the DOME-DISC calibration dither signals. Fig.3.17(b) shows the DOME-DISC corrected gyroscope measured rate versus the $1ppm$ accurate rates applied by the rate table. Ideally, we must measure the slope of to be one, when all the errors are removed. However, the results match to within $100 - 400ppm$ and is currently limited by gyroscope bias instability ($50ppm$ Fig.3.14), stochastic ambient temperature induced fluctuations and the stage cross-axis actuation error of $\approx 100ppm$ for $100V_p$ drive as discussed in section *V.A*.

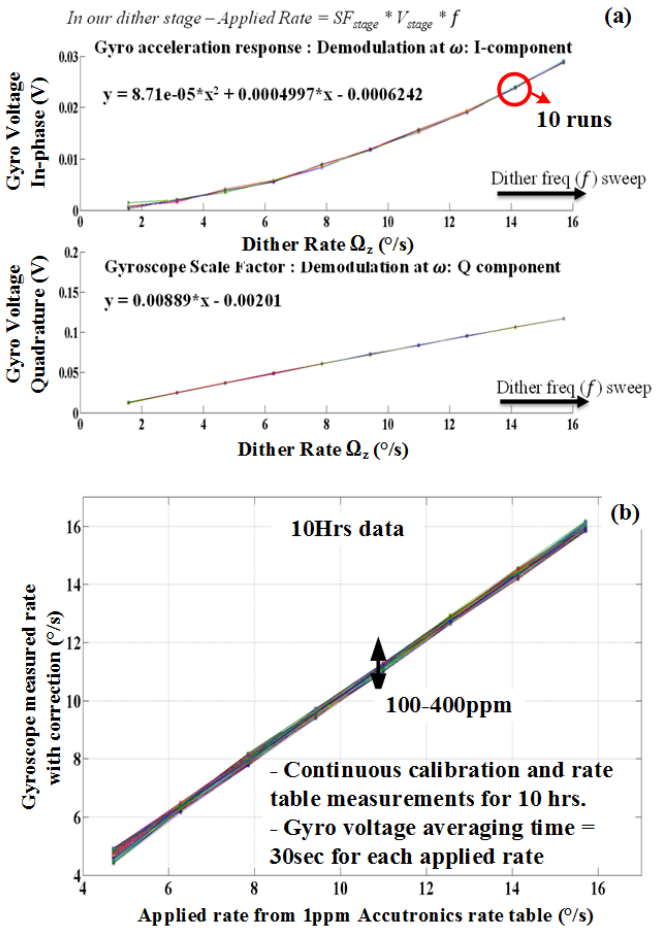

Figure 3.17: Gyroscope calibration data (a) I-Q demodulation of gyroscope response at dither frequencies to extract scale factor, bias and mount induced acceleration sensitivity. The dither sweeps were performed 10 times to measure variations (b) Gyroscope calibrated rate response to applied $1ppm$ accurate rate table rates

3.5.4 Stability and noise in calibration

The noise performance of DOME-DISC is characterized by comparing the Allan deviation of gyroscope scale factor (SF_g) obtained using DOME-DISC and the rate table. The Allan deviation of the stage position is obtained using NORIS when there is no drive voltage applied to the PZT stage. As shown in the Allan deviation plot in Fig.3.18(a), the DOME-DISC approach can track the

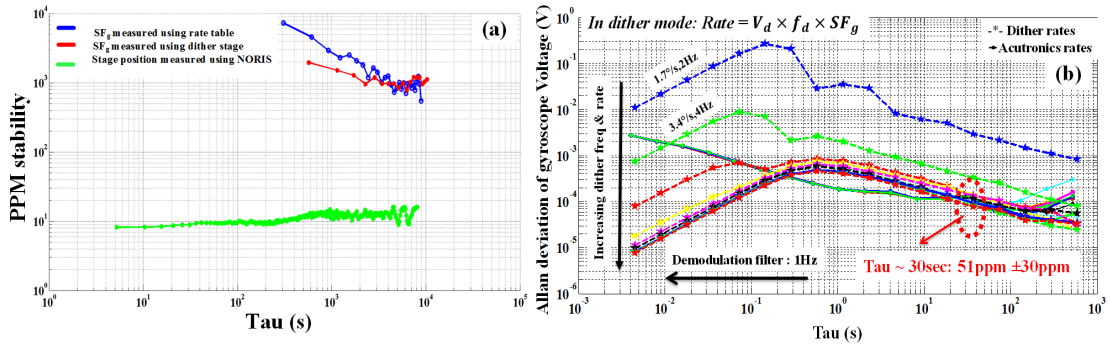

Figure 3.18: Stability measurements of DOME-DISC components in ambient conditions (a) Allan deviation of scale factor (SF_g) of ADXRS646 measured using DOME-DISC and Acutronics rate table along with Allan deviation of NORIS position measurement when the PZT stage is not driven (b) Comparison of Allan deviation of gyroscope output voltage for different applied rates by DOME-DISC and comapred to the Allan deviation of gyroscope voltage to rate table applied rates (Fig.3.14)

stability of gyroscope scale factor (SF_g) as good as the commercial rate table (Accutronics BD122). The stability of stage position measurement from NORIS is $\approx 10ppm$, which is better than the scale factor stability of the gyroscope under test ($> 5000ppm$). Therefore, NORIS can be used for long term calibration of the gyroscope. In order to measure the optimal averaging time for the gyroscope output rates and measure the dither rate stability, the Allan deviation of the gyroscope voltages for rate table applied rate is compared with the gyroscope voltage for the demodulated dither rates ($\Omega_z(f_d)$: Fig.3.10) from DOME-DISC (Fig.3.18(b)). Any additional errors from the DOME-DISC applied rates ($\Omega_z(f_d)$) should show in the demodulated gyroscope voltage signal. Result shows the that DOME-DISC has optimal noise performance at $\tau = 30s$ with the Allan deviation of $\approx 50ppm$, which is as good as the Allan deviation of gyroscope voltages at different rate table applied rates. Also, this is the bias instability limit of the

gyroscope under test (Fig.3.14). The dithering did not introduce any significant noise to the gyroscope voltages. However, at low frequency dither ($1-2Hz$), the measurement is limited by flicker noise of the demodulation circuitry as seen in the plot Fig.3.18(b). Frequencies $< 10Hz$ is avoided for calibration purposes. The additional $\pm 30ppm$ error is potentially from the frequency error in the thermally uncompensated drive oscillator ($\pm 5ppm$) and the the cross axis motion error of the PZT stage which can be as high as $100ppm$ for $100V_p$ drive (Fig.3.8).

3.6 Discussions

The gyroscope calibration precision of $50ppm$ demonstrated here is currently limited by the flicker noise (bias instability) limit of the gyroscope. To achieve $< 10ppm$ accurate gyroscope for applications in GPS denied inertial navigation [66], a low short term noise gyroscope is essential. While active calibration using DOME-DISC can correct for errors in timescales of minutes-hours, it is necessary to have gyroscopes which are short term (10-100 seconds) stable and low noise. Recent efforts in high Q, mode matched gyroscopes have shown promise in achieving low short term noise performance, reaching $< 5ppm$ ($\approx 1deg/hr$) [93]. However, they still suffer from scale factor and bias errors which need correction. It is desirable to have high Q mode-matched gyroscopes in DOME-DISC to achieve better MEMS sensor based inertial navigation systems. Some of the limitations in the current DOME-DISC implementation is power, size and also aging in PZT. Implementing the stage, NORIS and gyroscope closed loop control in CMOS might help reduce size, power requirements and also help achieve closed loop control of the stage.

3.7 Conclusion And Future Work

A $50ppm$ bulk PZT calibration stage with $< 5ppm/V$ cross axis motion coupling is demonstrated for Z-axis MEMS gyroscope calibration. The dither-demodulation approach enables in-situ calibration of the MEMS gyroscope at higher frequencies while the gyroscope is operational in baseband. For long term stable operation of the calibration apparatus, a $10ppm$ stable optical metrology system, NORIS can be employed in closed loop and can be potentially integrated in the same package as the calibration system. The stage can further be extended to operate for $X, Y, Z, \theta_z, \theta_x$ and θ_y to facilitate calibration of IMU (inertial measurement unit). The IMU calibration approach can help identify cross-talk and error correlation in the accelerometers and gyroscopes in the package and help improve their performance to achieve compact north finder using MEMS inertial sensor.

CHAPTER 4

BULK PZT CORIOLIS VIBRATORY Z-AXIS GYROSCOPE WITH INTEGRATED PZT STAGE FOR SELF CALIBRATION

4.1 Introduction

Gyroscope performance metrics such as sensitivity and rate resolution, rely on large mass and high drive resonator velocity [94]. High electromechanical transduction efficiency enables good drive velocities for low operation voltages. High density materials allow for large mass for a small areas compared to lower density materials. Piezoelectric transduction can be an attractive choice for gyroscopes owing to the high electromechanical coupling coefficients (k_{31}) and higher mass density of some piezoelectric materials compared to the electrostatic silicon gyroscopes [95]. For example, $\rho_{PZT} > 4\rho_{Si}$. The rate resolution of the gyroscope is fundamentally limited by the Brownian noise. The large mass in gyroscope leads to lower Brownian noise. Piezoelectric gyroscopes of different form factors, design and material choices have been explored before. Although, some of the previous works have demonstrated good sensitivity and quality factors [95,96] the solutions have often been large (centimeter scale) and not planar in design. The quartz tuning fork gyroscope demonstrated in [95] relies on side wall electrodes which could be difficult to fabricate at smaller scales. Planar shear mode gyroscopes [97] and SAW gyroscopes [98] offer high shock survivability, which is a desirable metric for inertial sensors in industrial and automotive applications. However, they have suffered from low sensitivities due to relatively low drive resonator velocity and effective mass. Recently, thin film AlN on silicon BAW gyroscope in [99] demonstrated a planar design with

good sensitivity and shock tolerance. Alternatively, a bulk-PZT gyroscope has a potential to have high sensitivity owing to its high electromechanical coupling coefficients compared to thin film AlN. The higher aspect ratio in bulk-PZT gyroscope enables gap-free sensors with high dynamic range and better shock tolerance. Additionally, the potential for monolithic integration of bulk-PZT gyroscope within the precision piezoelectric in-situ calibration platforms [100] using the laser micromachining process, enables a pathway for long term stable gyroscopes.

As in most Coriolis force gyroscopes, fabrication variations often lead to non-ideal spring constants causing frequency mismatches and cross-axis stiffness components between drive and sense resonators [101]. These errors have proven to be detrimental for gyroscope operation as they lead to bias and quadrature errors [101]. The resonance frequency is also known to drift with temperature and time, especially in PZT [14, 95] leading to variability in scale-factor and bias, which are sources of sensor inaccuracies. Operating under closed loop control with mode-matched drive and sense resonances, along with quadrature control is one of the pathways for high performance gyroscopes [101]. Previous work on piezoelectric gyroscope tuning and controls have focused on electrostatic tuning mechanisms [102]. However, this technique relies on micro-scale gaps, making it susceptible to failure under high shock conditions and limited sensor dynamic range. Recent work in gap free piezoelectric tuning schemes [99] has shown AC tuning of resonance frequency for piezoelectric thin film AlN on silicon BAW gyroscopes. In this work, piezoelectric tuning of frequency and quadrature error in bulk-PZT gyroscope with DC voltages is presented. The DC tuning approach circumvents the problems of feedthrough

and phase errors that arise in AC tuning methods. Also, the DC approach does not require precision oscillators and additional loops as in the AC tuning method, leading to simplification of the gyroscope tuning circuitry.

To compensate for fluctuations in scale factor and bias in PZT gyroscopes, one approach is to have an in-run calibration platform. In general, inertial sensors are calibrated on a rate table for their input-output characteristics, right after packaging the device. For active calibration of gyroscopes, it is desirable to have a miniature platform capable of applying rate stimulus with minimal cross axis coupling or undesirable motion. PZT bimorph actuators are known to have high force and good electro-mechanical transduction efficiency making them a viable option for low power high precision micro stages for gyroscope calibration [100, 103]. In this work the monolithic integration of bulk PZT gyroscope onto PZT dither stage is demonstrated. The PZT stage is capable of in-situ gyroscope scale factor and bias measurements. The scale factor data can be used to track drift and mismatches in the gyroscope for a potential close loop correction.

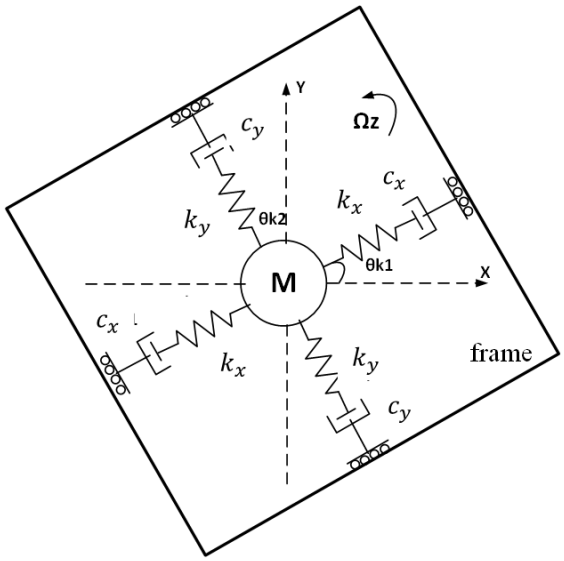

Figure 4.1: Generic Coriolis vibratory mass gyroscope schematic.

4.2 Bulk PZT Gyroscope

4.2.1 Design consideration

Generic model

A conventional Coriolis vibratory rate gyroscope can be represented as shown in Fig.4.1. The model for such a gyroscope can be written as, [104]

$$m\ddot{q} + (2\Omega + C)\dot{q} + Kq = F \tag{4.1}$$

where, x is the drive and y is the sense axis. m is the mass, $q = [x\ y]^T$ are the axis displacements, $F = [F_x\ F_y]^T$ is the force vector. K and C represents the stiffness and damping terms of the resonator respectively. Ideally, K and C are diagonal matrices, however due to non-idealities and mismatches they are often modeled

as ,

$$K = \begin{bmatrix} k_x & k_{xy} \\ k_{yx} & k_y \end{bmatrix},\ C = \begin{bmatrix} c_x & c_{xy} \\ c_{yx} & c_y \end{bmatrix},\ \Omega = \begin{bmatrix} 0 & -\Omega_z \\ \Omega_z & 0 \end{bmatrix}$$

The terms in the matrix are functions of θ_{k1} and θ_{k2} which model for the fabrication induced non-idealities. Ω is the angular rate input [104, 105].

The force vector and corresponding solution to (1) can be of the form

$$F(t) = \begin{bmatrix} F_d(t)e^{j\phi_F(t)} \\ (F_c(t) + jF_s(t))e^{j\phi_F(t)} \end{bmatrix} \tag{4.2}$$

$$q(t) = \begin{bmatrix} x_d(t)e^{j\phi_x(t)} \\ (y_c(t) + jy_s(t))e^{j\phi_x(t)} \end{bmatrix} \tag{4.3}$$

where, F_d and ϕ_F is the drive force amplitude and phase. y_c and y_s are the cosine and sine components (in-phase and quadrature) of displacements for the y-axis resonator with x-resonator phase ϕ_x. On solving (1) with solutions (2),(3), with the assumptions, $\dot{\phi}_x \approx \omega_x$, $y_c, y_s << x_d$ and $\omega_x >> \Omega_c, \Omega_z$ and under the mode-mismatch conditions ($\omega_x \neq \omega_y$) we can write [104, 105],

$$\dot{x_d} = -\beta_x x_a + (\alpha_z\Omega_z - \Omega_c)y_c - \Omega_{kx}y_s - \frac{1}{2m\omega_x}F_d sin\Delta\phi_x \tag{4.4}$$

$$\dot{y_c} = -\beta_y y_c + \Delta\omega_0 y_s - (\alpha_z\Omega_z + \Omega_c)x_d + \frac{1}{2m\omega_x}F_{y_s} \tag{4.5}$$

$$\dot{y_s} = -\beta_y y_s - \Delta\omega_0 y_c + \Omega_{kx}x_d - \frac{1}{2m\omega_x}F_{y_c} \tag{4.6}$$

where resonant frequencies ω_x, ω_y, bandwidths β_x, β_y along x,y axis are:

$$\omega_x = \sqrt{\frac{k_x}{m}},\ \omega_y = \sqrt{\frac{k_y}{m}},\ \beta_x = \frac{c_x}{2m},\ \beta_y = \frac{c_y}{2m}$$

and bias errors due to damper and spring axis misalignment is $\Omega_c, \Omega_{k(x,y)}$ are:

$$\Omega_c = \frac{c_{xy}}{2m},\ \Omega_{kx} = \frac{1}{2}\frac{k_{xy}}{\omega_x m},\ \Omega_{ky} = \frac{1}{2}\frac{k_{xy}}{\omega_y m}$$

$\Delta\omega_0 = \frac{1}{2\omega_x}(\omega_x^2 - \omega_y^2)$ and $\Delta\phi_x = \phi_x - \phi_F$

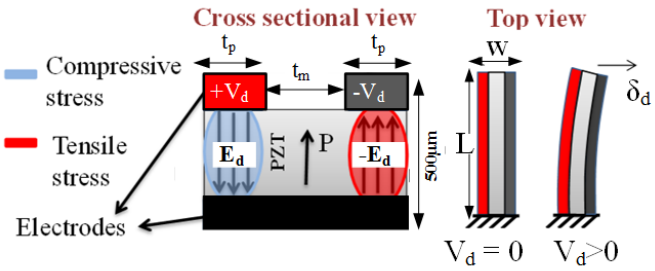

Figure 4.2: Sketch of the bulk PZT bimorph transducer, which is a basic building block for actuation and sensing in the X and Y resonator of the gyroscope. P denotes the polarization direction for the PZT4 plate.

Drive transduction

The drive resonator dynamics is as described by (1), (2) and (3). The drive force F_d for this device is obtained by using piezoelectric in-plane actuators. In general, for a piezoelectric actuators, the strain generated owing to d_{31} can be written as

$$s_x = d_{31}\frac{V_d}{h},\ d_{31} = \sqrt{\frac{k_{31}^2 \epsilon_0 \epsilon_r}{Y_{11}}} \tag{4.7}$$

For a drive resonator with quality factor Q_x, the force achieved can be written as,

$$F_d \propto Q_x k_x (\frac{k_{31}^2 \epsilon_0 \epsilon_r}{Y_{11}})(\frac{V_d}{h}) \tag{4.8}$$

where, V_d is the applied drive voltage amplitude and where, h is the thickness of the piezoelectric transducer, Y_{11} is the Young's modulus for the in-plane actuator. k_{31} is the electromechanical coupling coefficient for electric fields applied in the thickness direction resulting in longitudinal vibrations in the $X-Y$ directions. As seen in Eq(8) it is desirable to have high $k_{31}Q$ in the drive actuation. To generate the desired in-plane forces, a previously demonstrated high aspect ratio (1:3) $500\mu m$ thick bulk PZT-4 lateral bimorph actuator is chosen, which has an inherent differential voltage drive capability. When a voltage +V and -V is applied on top electrodes and a common ground on the bottom, compression and tension is formed along the length, owing to the d_{31} coefficient of the PZT. This causes in-plane bending in the beam as shown in the sketch in Fig.4.2. Owing to large $k_{31}Q(> 100)$ (section 1.5.2, Table.1.2) in the lateral bimorph actuators, large in-plane forces are possible (Eq(8)). The high aspect ratio and the predominant piezoelectric coupling (d_{31}) ensures $< 100ppm$ cross axis (out-of plane) coupling in the actuators (section 1.2.1) . On constraining the lateral bimorph width to $450\mu m$, with $150\mu m$ wide electrodes (limited by the fabrication tolerance and laser beam diameter [16]) the in-plane tip deflection of a single lateral bimorph actuator of length L can be shown as, (section 1.2.1)

$$\delta_d(j\omega) = \frac{7.29 \times 10^{-7} L^2 V_d}{(1 - (\frac{\omega}{\omega_x})^2) + \frac{j\omega}{\omega_x Q}} \tag{4.9}$$

where, the Q for PZT bimorph actuator can range from $1000 - 1500$.

Sense transduction

Using the inverse piezoelectric effect, the lateral bimorph transducers can be used as an in-plane Coriolis and drive force sensor along X and Y axis respectively. The lateral bimorph is capable of generating differential output voltages and currents due to the strains induced by the in-plane forces (section 1.2.2). The current output of the lateral PZT bimorph is given by,

$$i_s \propto j\omega(\frac{3}{4}\frac{d_{31}Y_{11}t_p^2F_{(x,y)}}{Lk_{(x,y)}}) \tag{4.10}$$

Sensing the current allows for measuring of input-output characteristics and electrical frequency response of X-Y resonators. When there is no external force on the sense (y) resonator ($F_y = 0$), Eq(1) can be rewritten as,

$$\ddot{y} + \frac{\omega_y}{Q_y}\dot{y} + (\omega_y^2 - \Omega_z^2)y = -2\dot{x}\Omega_z \tag{4.11}$$

Further, for resonance condition, under mode matched condition ($\omega_x = \omega_y$), in an ideal case with no mismatches, from Eq(10) and Eq(11) the gyroscope scale factor can be estimated as,

$$SF_g = \frac{i_s}{\Omega_z} \propto \omega_x(\frac{3}{4}\frac{\epsilon_0\epsilon_r k_{31}^2 t_p^2 Y_{11}^{1/2} Q_x Q_y m\dot{x}_d}{k_y L}) \tag{4.12}$$

where, t_p is the electrode width of interest (Fig.4.2), optimized to regions of maximum strain to improve SNR of the sense signals (Fig.1.7, Fig.1.8).

The signal induced by mechanical noise in the sensor can be expressed as,

$$i_n \propto \frac{1}{x_d\omega_x}\sqrt{\frac{4k_bT\omega_xBW}{Qm}} \tag{4.13}$$

Where, k_b is the Boltzman constant and T is the temperature and BW is the device bandwidth and the drive displacement amplitude $x_d = F_d/k_x$ (Eq(8)). From Eq(8), (12) and (13) for high SNR, it is clear that we need to have large $k_{31}Qm$ for the device. A monolithic bulk PZT based gyroscope design enables higher mass for a given area than silicon ($\rho_{PZT} > 4\rho_{Si}$). Also, on having high k_{31} while relaxing on the Q requirements, we can increase the gyroscope bandwidth ($BW = \omega_y/(2\pi Q_y)$). The monolithic bulk PZT transducer based design proposed here has higher $k_{31}Q$ (> 100) for low Q than most existing capacitive counterparts (< 1), which often rely on high Q for bandwidth tradeoff. Hence, lateral bimorph transducer is a desirable building block for the drive and sense in-plane (XY) resonator to achieve a bulk PZT Z-axis gyroscope.

4.2.2 Errors and noise sources

Like most MEMS gyroscopes, the bulk PZT gyroscope suffers from various error sources and has a few errors similar to capacitive gyroscopes [106]. Although there are many advantages in a piezoelectric gyroscope as discussed earlier, the gyroscope suffers from bias and scale factor drifts due to fabrication induced mismatches, temperature fluctuations and aging in the material [14]. Additionally, in PZT there are error contributions from the pyroelectric effect, thermal self heating with resonator cycles [107], which effects the long term stability of gyroscope. Here their contributions are discussed and addressed with the mitigation steps taken in the design.

Drive amplitude and frequency error

A stable drive resonator is essential for high performance gyroscope. As seen in Eq(4), fluctuations in the drive velocity induces spurious current noise in the sense resonator. In PZT it is known that material parameters change due to aging and thermal fluctuation from environment and self heating over resonator cycles. While changes in d_{31}, ϵ_r and Q effect the drive displacement amplitude (Eq(4),(8)), spring softening due to thermal expansion and changes in Y_{11} would change the resonance frequency of the resonator and the drive displacement velocity (Eq(4)). A general approach to achieve stable resonance is to have closed loop resonator control [108,109]. On sensing the currents from dedicated lateral bimorphs in the drive resonator (drive pickoff), the drive velocity $\dot{x_d}(t)$ is monitored. Assuming there is no thermal gradient across different elements in the device, from Eq(8) and (10) we can see that by adjusting the drive amplitude based on the current sensed from the drive resonator pickoff, to maintain a constant drive velocity in automatic gain control (AGC) loop. The control loop also accounts for fluctuation in the PZT material parameters (k_{31}, ϵ_r, Y). As seen in equation (4), by having a phased lock loop circuitry (PLL) maintaining $\Delta\phi_x$ at 90^0 (resonance condition) and a automatic gain control (AGC) loops with PID control on the drive voltage one can achieve stable drive velocity.

Sense error

Due to the fabrication imperfections and spring non-idealities, often modeled as off-diagnal elements in K and C (Eq(1)), the sense resonator sees additional rate errors commonly referred to as quadrature and bias drift [101,104,105]. Assuming perfect demodulation of the sense signal, these errors are modeled as Ω_c

and $\Omega_{k(x,y)}$. Such errors can be mitigated by having additional tuning electrodes applying external forces F_{xy} at the resonance frequencies using the lateral PZT bimorphs placed such that the forces are applied at 45^0 to the drive axis. Additionally, the sense current has noise from pyroelectric effect and self heating, at thermal time constant of the order of seconds as shown in [BIMROPH]. This directly effects the scale factor of the gyroscope by changing the charge generation capabilities. Thermal compensation by means of thicker metal, packaging, ovenization and insitu calibration may be necessary to mitigate such effects

Phase error

Due to the fabrication intolerance, non-idealities and the anisotropy in PZT, we expect to see mode splits for the drive and sense mode even for a symmetric design. Under mode mismatched conditions, we have to take into consideration additional phase shift in the sense demodulation given by [110]

$$\phi_y = \phi_x - 90^o - tan^{-1}\frac{\frac{1}{Q_y}\frac{\omega_x}{\omega_x+\Delta f}}{1-(\frac{\omega_x}{\omega_x+\Delta f})^2} \tag{4.14}$$

Since there are additional phase shift from traces, its better to extract this from phase response plots obtained experimentally.

4.2.3 Design

The bulk-PZT gyroscope design demonstrated in this work is a Coriolis vibratory yaw rate gyroscope. To improve the shock survivability the approach here is a monolithic bulk micromachined gyroscope with high spring constants. The design has the mass, suspension and the lateral bimorph transducer elements

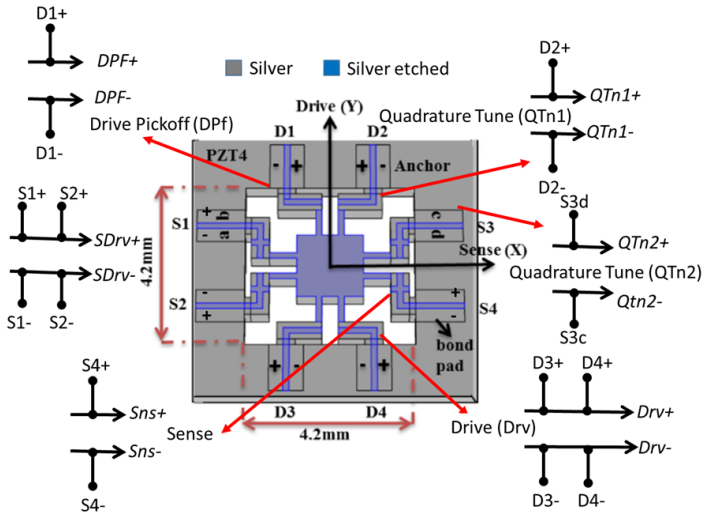

Figure 4.3: Sketch of the bulk PZT gyroscope showing the all the electrodes and connections. the length of each bimorph transducer element is $L = 1.1mm$, with width $w = 450\mu m$ and thickness $h = 500\mu m$

all made of PZT-4. Monolithic design ensures stiff suspension and also reduces chances of failure compared to heterogeneous integration that has additional layers such as adhesive layer and other structural materials. The device is a single mass sensor with eight lateral PZT bimorph transducers, each with 2 electrodes for differential drive and sense. Fig.4.3 shows the device schematic with all the lateral bimorph labelled. $D3$ and $D4$ are connected to have a fully-differential piezoelectric drive (Drv). Additionally, they also allow for drive resonator frequency tuning when DC voltages are applied. Similarly, $S1$ and $S2$ are used to measure sense resonator characteristics ($Sdrv$). Coriolis signal is detected on the differential sense bimorph $S4$ (Sns). Lateral bimorph (Dpf) is used for sensing drive resonance characteristics. The differential signal from this drive resonance pick-off bimorph (Dpf) is used in the feedback control of the drive resonator frequency and amplitude. Using the combination of bimorphs $D2$ and $S3$, we can tune for quadrature (k_{xy}) errors using $Qtn1$ and $Qtn2$. The

tuning of k_x, k_y and k_{xy} is possible by virtue of non-linear drive. As described in [105], for a generic vibratory gyroscope, the errors in the gyroscope leading to the mode split can be modelled as mismatches in the stiffness in the drive and sense resonators (k_x, k_y). Additionally, cross-axis stiffness (k_{xy}) arises from fabrication intolerance and spring non-idealities. For mode-matching the gyroscope one needs to tune for k_x, k_y and also k_{xy}. Closed loop control of errors is necessary as the frequency and damping mismatches are often changing with time and temperature [99,111]. Ways to tune out such errors electronically, with dedicated loop controls for drive and sense resonators and quadrature control was explored. Here, the sensitivities of frequency and quadrature tuning loops in a bulk PZT yaw gyroscope are shown. In this design, the length of each bimorph transducer element $L = 1.1mm$, $t_p = 150\mu m$ $w = 450\mu m$ $h = 500\mu m$.

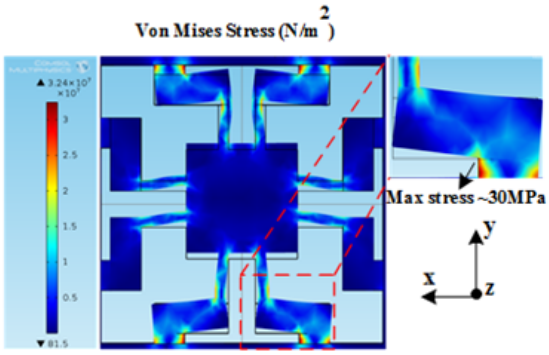

Figure 4.4: COMSOL^{TM} simulation for anchor stress in bulk PZT gyroscope for $10V_p$ resonant drive

4.2.4 Nonlinear model of the resonator

The bulk PZT gyroscope utilizes the piezoelectric properties of PZT lateral bimorph for actuation and sensing. In PZT, material properties such as Young's modulus, d-coefficients, dielectric constants and mechanical loss factor have

non-linear dependence to stress [112]. Therefore, a simple model of a spring-mass piezoelectric resonator can be expressed as,

$$\ddot{x} + c\dot{x} + \omega_0^2 x = Fcos(\omega t) \tag{4.15}$$

Resonant frequency of a resonator is proportional to the Young's modulus of interest in PZT (Y) and elasticity in general.

$$\omega_0^2 \propto \frac{Ywh^3}{4L^3m} \tag{4.16}$$

Where, m is the mass. The nonlinearity in Y due to stress in PZT can be expressed as [112],

$$Y = Y_0 + \beta_m Y_0 T_m^2 + (higher\ order\ terms) \tag{4.17}$$

where, $\beta_m = \frac{\Delta Y}{Y_0}$ and T_m is the stress The stress caused due to piezoelectric drive is,

$$T_m = T_0 cos(\Omega t + \phi) + T_{dc} \tag{4.18}$$

$$T_0 \propto \frac{d_{31} V_{ac}}{h} \tag{4.19}$$

Where, T_{dc} is the stress caused by DC voltage. Combining equations (15)-(19), an approximate model of the non-linear resonator can be expressed as,

$$\begin{aligned} &\ddot{x} + c\dot{x} + \omega_0^2 \left[1 + \beta_m \left(\frac{T_0^2}{2} + T_{dc}^2\right)\right] x \\ &+\omega_0^2 \left[\beta_m \left(2T_{dc}T_0 cos(\omega t + \phi) + \frac{T_0^2}{2} cos(2\omega t + 2\phi) + ...\right)\right] x \\ &= Fcos(\omega t) \end{aligned} \tag{4.20}$$

Using finite element analysis software (COMSOL^{TM}), the stress as a function of drive voltage in the piezoelectric gyroscope is simulated. This is done to estimate the drive voltage required to operate in the non-linear region. FEA simulation in Fig.4.4 shows the stress distribution for the device. The model assumes Q_y = 1000. Simulation predicted that for this design, the Von-Mises stress is > 10^7 Pa (<yield stress $500MPa$ for PZT) for $10V_p$ drive at resonance. With stress higher than 10^7 Pa, we can be certain that nonlinearity can be achieved for greater than $5Vp$ drive

Nonlinearity in the elastic constants can also be leveraged by operating the resonator at high stress regions (stresses > $10^7 Pa$) [112]. As shown in Eq(20), one can use the stress induced by DC voltage to bias the resonator at different small signal stiffness. The nonlinearity in Y also leads to higher order harmonics in the resonator response. DC control of stress for bimorphs in the drive ($D3, D4$) and sense resonator ($S1, S2$) tunes k_y, k_x for mode matching purposes. From equation Eq(20) we can express the frequency tune sensitivity at resonant operation with DC tune voltage as,

$$\frac{\Delta\omega_0}{\omega_0} \approx \sqrt{\frac{\beta_m d_{31} Y V_{dc}}{h}} \tag{4.21}$$

Additionally, by having a DC control of stress on $D2$ and $S3$ bimorphs, we can tune for quadrature error by controlling off-diagonal spring constant of the resonator (k_{xy}). Table.4.1 shows the design specification and parameters for the bulk PZT gyroscope.

Table 4.1: Design Specifications

Parameter	Value
$k_x = k_y$	5.18×10^6 N/m
k_z	4.84×10^6 N/m
ρ_{PZT}	$7600 kg/m^3$
m	10.34×10^{-6}kg
$f_x = f_y$	$112.63 kHz$
$Q_x = Q_y$	1000
β_y	$48.3 Hz$
x_a (1V drive)	$88.2 nm$
SF(mode-mismatch, 1V drive)	$\approx 26 nA/deg/s$
β_m (PZT) [112]	2×10^{-15}
Frequency tune	$8.3 ppm/V$
Dielectric dissipation factor (tan δ) [5]	0.4
Drive resonator capacitance C_d	$24.1 pF$
Device power $\left(2\pi f_x C_d tan\delta V_d^2\right)$ $1V_p$ drive	$6.8 \mu Watts$

4.2.5 Gyroscope control circuitry

Closed loop control of drive and sense resonators are necessary to mitigate many errors originating from structural imperfections, nonlinearity and environmental effects.

Fig.4.5 shows the schematic of gyroscope control PCB used. Zurich Instrument HF2LI is used for frequency response measurements, synchronous demodulation, PID and PLL control loops. The interface circuit for the gyro-

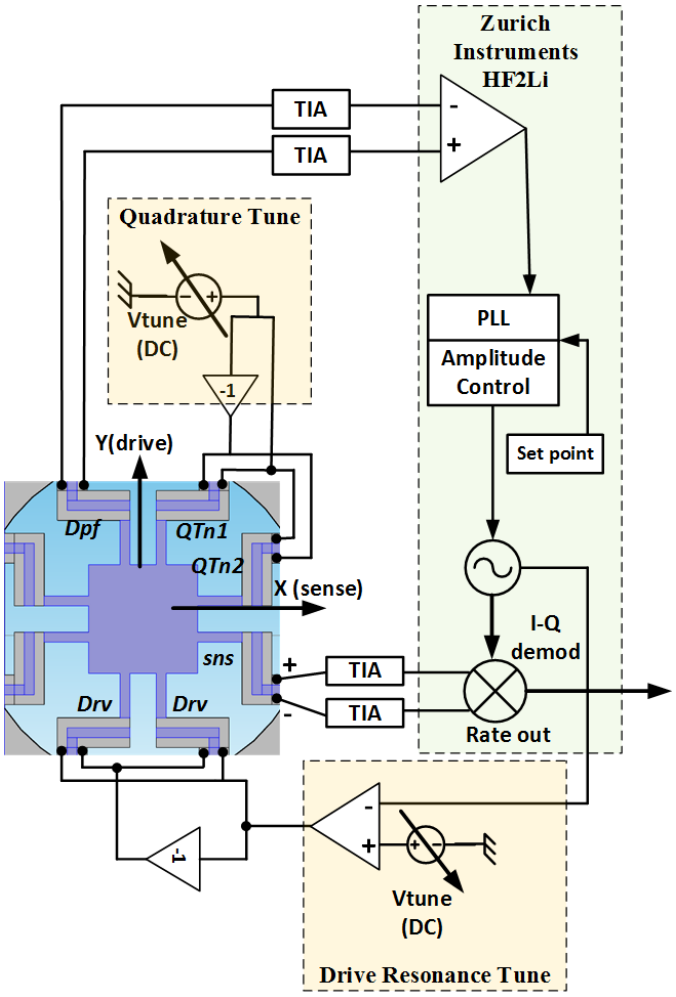

Figure 4.5: Circuit schematic showing the control blocks for the operation of bulk PZT gyroscope.

scope is designed using off the shelf components. The gyroscope drive circuit has two high voltage operational amplifiers (Apex Microelectronics PA443DF). High voltage amplifiers (PiezoDrive PDM200B) were used to amplify (x20) precision DC tune voltage ($0 - 5V$), up to $\pm 150V$ and added to the AC drive from HF2LI. Similar drive is used for $Sdrv$ while measuring sense resonator response. For the sense circuit, TL082 JFET opamps with 1M resistors buffer output from Dpf and Sns to HF2LI, to measure displacement. Since the drive and sense electrodes are in close proximity and the respective signals are at the same fre-

quency, parasitic coupling of the drive signals in the sense is seen. To mitigate the effects parasitic capacitances and $60Hz$ noise, currents from from Dpf and Sns are measured using a TIA (LTC6268) with $10k\Omega$ and $9pF$ as feedback resistors and capacitors. Currents from Dpf is a measure of drive velocity and the currents from sns is the rate signal. In the quadrature tuning, PA443DF amplifies (x20) DC tune voltages, and provides bridge drive to $Qtn1$ and $Qtn2$. An external power source supplies $\pm 12V$ to the PCB.

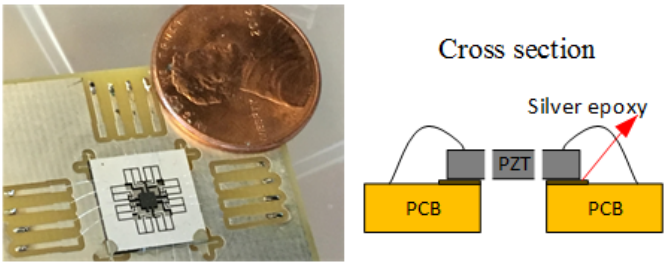

Figure 4.6: Fabricated bulk PZT gyroscope bonded onto a custom PCB. Cross section of the assembly is also shown.

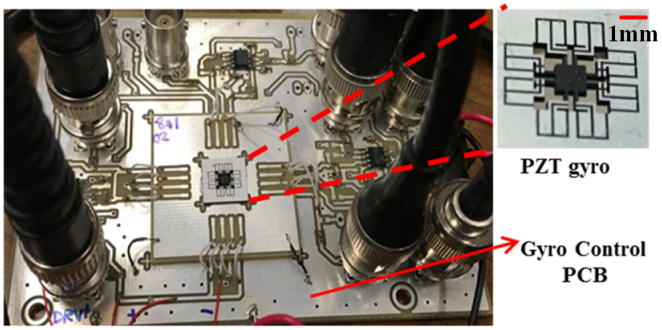

Figure 4.7: Fabricated device bonded onto PCB with control electronics and interface to Zurich Instruments HF2li.

4.3 Fabrication

The device is fabricated using the laser micromachining process described in [16]. Bulk PZT plates (500 micron thick) with silver electrodes on both top and

bottom were laser micro-machined. High aspect ratio (width: height of 3:10) with reduced side wall angles were achieved by repetitive hatching of dense laser scan lines. The laser micro-machining process is discussed in detail in [16]. Post fabrication, the device is bonded onto a custom PCB with a silver acrylic and wire bonded (Fig.4.6). For further testing and characterization, an interface PCB is designed for controls. PZT-gyroscope is operated in air, packaged on a custom PCB. The gyroscope is bonded on PCB using conductive acrylic (GC electronics 22-023) for bottom electrode contact and the top electrodes are wirebonded to interface electronics for characterization as shown in Fig.4.7.

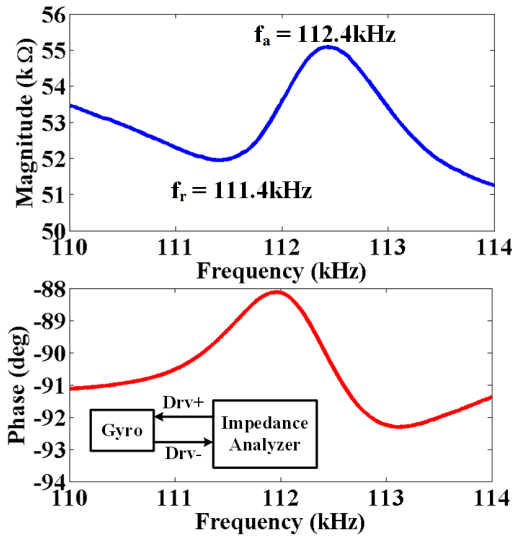

Figure 4.8: Impedance response of the drive resonator in the bulk PZT gyroscope measured for $1V_p$ drive, using HP4194A. Sketch in the inset shows the connections to the drive terminal *Drv* while the other electrodes of the gyroscope are left floating.

4.4 Measured Characteristics Of Bulk PZT Gyroscope

4.4.1 Bulk PZT gyroscope frequency response

The impedance response of the drive resonator of the gyroscope is measured to estimate the electromechanical coupling coefficient k_{31}. Fig.4.8 shows the impedance response of the *Drv* port of the drive resonator. The $k_{31} = 14.7\%$ for the high frequency gyroscope mode is estimated from [113],

$$k_{31} = \sqrt{\left(\frac{(\pi/2)(f_a/f_r)tan[(\pi/2)((f_a - f_r)/f_r)]}{1 + (\pi/2)(f_a/f_r)tan[(\pi/2)((f_a - f_r)/f_r)]}\right)} \tag{4.22}$$

The phase response in Fig.4.8 does not show an expected phase shift of a second order resonance system. This is due to the parasitic capacitance in the measurement setup. To alleviate these effects, subsequent measurements were done using a differential sensing, TIA and a lock-in amplifier.

Using the Zurich Instruments lock in amplifier (HF2Li), the frequency response of the device is measured for $10V_p$ differential drive on the *Drv* and *Sdrv* electrodes. The resonator pickoff *Dpf* and *Sns* are buffered to measure the respective voltages. The frequency response of the drive and sense resonator voltage (displacements) for the Y (drive) and X (sense) resonators is shown in Fig.4.9 with drive resonance frequency around $108kHz$. From the frequency response we can measure the quality factor, given by

$$Q = \frac{\omega_0}{2}\frac{d\phi}{d\omega}|_{\omega_0} \tag{4.23}$$

where, ϕ is the phase. The resonator has a quality factor $Q \approx 100$.

Frequency domain analysis in COMSOL^{TM}, under symmetric meshing conditions yielded the resonance mode to within 5% of the experimental results. The mode shapes of the drive and sense simulated using COMSOL^{TM} is as shown in the inset of Fig.4.9. The model here does not include damping and spring constant mismatches. Without any tuning, the device shown has a mode split of $< 80Hz$. Several other devices were characterized for the as-fabricated mode splits. Although the devices were symmetric in design, most devices had $< 100Hz$ mode split owing to the fabrication inaccuracies arising from the laser micromachining process.

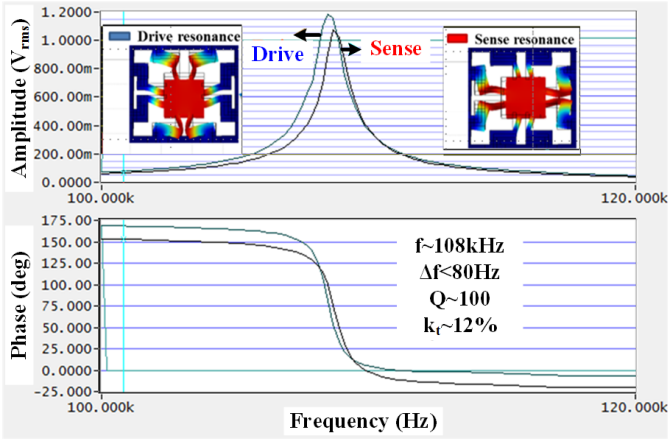

Figure 4.9: Measured frequency response of the drive and sense resonators for $10V_p$ drive. As-fabricated mode split $< 80Hz$. Inset shows COMSOL mode simulations for drive and sense resonance.

4.4.2 Bulk PZT gyroscope sensitivity under mode-split operation

Initially, the gyroscope scale factor is measured under mode-split open loop sense configuration. In this measurement, JFET buffers are used instead of transimpedance amplifiers to measure sense voltages without gain stages. Fig.4.10

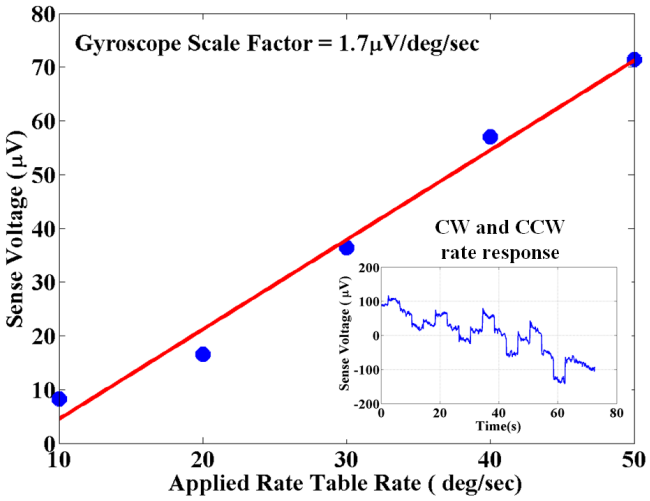

Figure 4.10: Scale factor of the bulk PZT gyroscope for $10V_p$ drive with no gain stages on a commercial rate table (Ideal Aerosmith 1270VS). The gyroscope has $< 1kHz$ mode-split between drive and sense. Picture in the inset show the rate response of the gyroscope as a function of time when different CW and CCW rate were applied by the rate table for 4s intervals

shows the measured scale factor using a rate table. The scale factor of the gyroscope is $1.7\mu V/deg/sec$. Bias drift of $\approx 1deg/sec$ is measured for the gyroscope with $< 1kHz$ mode mismatch between drive and sense resonator. The bias drift is as seen in the gyroscope voltage response as a function of time in the inset of Fig.4.10. Therefore, for each rate measurement the bias offset for the reported sensitivity curve is subtracted in Fig.4.10. The bias drift measured in the gyroscope is potentially due to the mode-split between drive and sense resonator reducing the effective Q [114]. Additionally, since there is no quadrature compensation for this gyroscope, we can expect bias drift due to Ω_c and $\Omega_{k(x,y)}$ (Eq(6)).

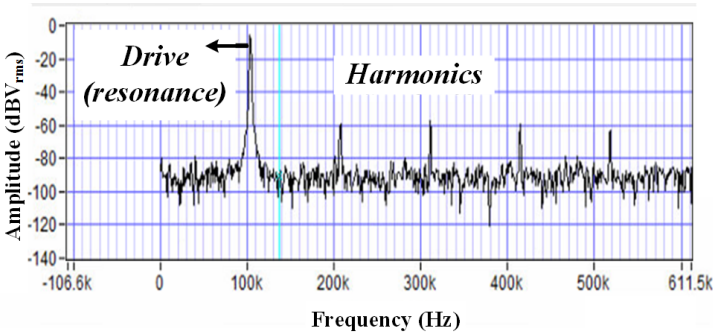

Figure 4.11: Resonator nonlinearity: Frequency response of drive pick-off electrode (Dpf) on $10V_p$ drive (Drv) at resonance. Non-linear dependence of elasticity to stress in PZT allows for tuning of spring constants.

4.4.3 Nonlinear response of the bulk PZT resonator

In order to operate the gyroscope in the non-linear regime, the Drv electrodes are driven at $10V_p$, resonance. The tuning voltages were all set to zero for measuring the non-linear response of the drive resonator. The gyroscope is operated under closed loop drive conditions using phase locked loop (PLL) and fixed drive amplitude using proportional control for optimal operation. Fig.4.11 shows the frequency response of differential signals obtained from Dpf bimorph. The measured the drive resonator response has higher order harmonics. Harmonics for drive amplitudes $< 10V_p$ were not readily measurable. As suggested by the simulation result in Fig.4.4, we see nonlinearity for drive $>= 10V_p$ at resonance, when the high stress criterion is met.

4.4.4 Frequency and quadrature tuning of bulk PZT gyroscope

The gyroscope is operated under closed loop non-linear drive conditions as explained before. The drive signals are frequency controlled using phased locked loop to track the resonance frequency shifts. The phase lock loop tracks the resonance frequency shifts while applying signals of frequencies corresponding to 0^0 phase between reference drive oscillator and the signal from Dpf. An additional DC voltage on the drive electrodes (Drv), changes the resonance frequency of the drive resonator. Fig.4.12 shows the frequency shifts recorded using PLL for manual sweep of DC voltages on Drv electrodes. On applying $50V$ DC, the drive resonator frequency shifted by $50Hz$ from its initial resonance frequency of $108kHz$. The frequency tune sensitivity of DC voltage is measured to be $10ppm/V_{DC}$. The measurement is in close agreement with estimated tune sensitivity of $8.3ppm/V$ in Table.4.1

To demonstrate quadrature tuning sensitivity of DC voltages on QTn electrodes, the gyroscope is operated under the closed loop drive condition as described above. The sense resonator is operated under open loop and the output is obtained by synchronous demodulation at the drive resonance frequency. The gyroscope is operated under mode-mismatched condition with demodulation phase correction due to the mode-split (Eq(14)). Initial quadrature is canceled using AC voltages on $Sdrv$ to record the effect of DC quadrature tune. Effect of DC voltage on quadrature is shown in Fig.4.13 to demonstrate k_{xy} compensation. In the experiments, the DC voltages were swept manually, in $10V_p$ increments while recording the quadrature channel. For a scale factor of $1.3\mu V/deg/s$, a quadrature tuning sensitivity of $20deg/s/V_{DC}$ is measured.

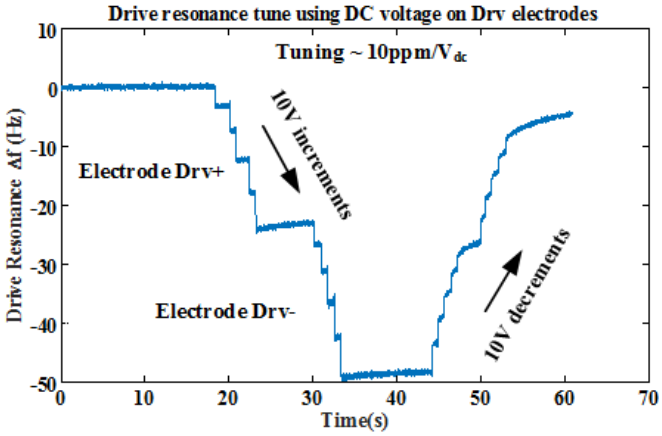

Figure 4.12: Frequency tuning sensitivity: Change in the drive resonance frequency with DC voltages on Drv electrodes under $10V_p$ closed loop drive operation, measured by the HF2li lock-in amplifier PLL

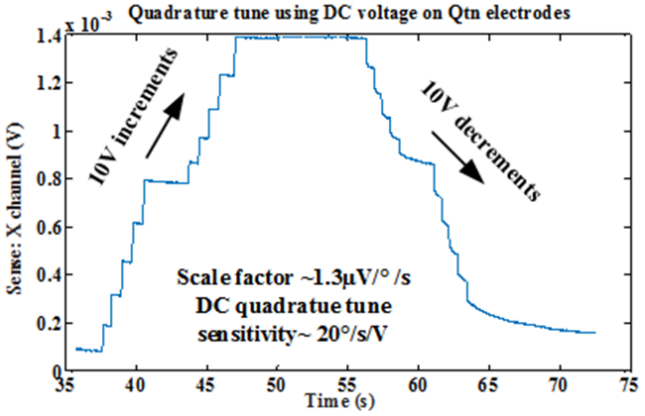

Figure 4.13: DC voltage quadrature tune sensitivity: Initial quadrature is removed using AC voltages at resonance on Sdrv electrodes. Plot shows quadrature tuning sensitivity for DC voltage sweep on QTn electrodes under $10V_p$ closed loop drive operation

4.5 Monolithic Integration Of PZT Gyroscope Onto PZT Dither Stage

A 50ppm precision PZT dither stage has been demonstrated to correct for scale factor and drifts in commercial silicon gyroscopes [100]. One can use the

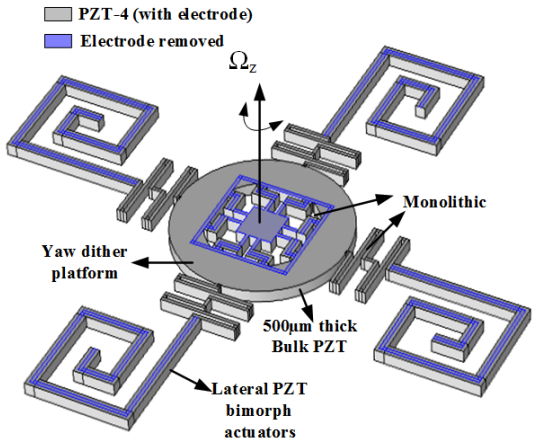

Figure 4.14: Sketch showing monolithically integrated bulk PZT gyroscope on the bulk PZT dither stage

same bulk PZT stage for in-situ calibration of the bulk PZT gyroscope. Monolithic integration of gyroscope and stage is possible as both are fabricated using the same base technology with the fundamental building block being the lateral PZT bimorph transducer. The previous approaches for in-situ calibration have relied on manual assembly of inertial sensors onto the calibration stage [100, 103]. Manual assembly of inertial sensors leads to errors and does not allow for microsystem integration. Manual mount induced errors often lead to cross axis and acceleration sensitivities [100]. Fig.4.14 shows the 3D sketch of the monolithic device. Additionally, the monolithic integration improves the anchoring to improve the Q of the resonators. Further, since the gyroscope on stage is tethered on four PZT beams (Fig.4.14), the thermal resistance increases and enables better thermal isolation of the device from ambient fluctuations.

The bulk PZT stage can apply in-plane dither (θ_z) as a function of applied sinusoidal voltage. Yaw dither rates can be applied to the gyroscope under test by varying the frequency of the input sinusoidal voltage while keeping the

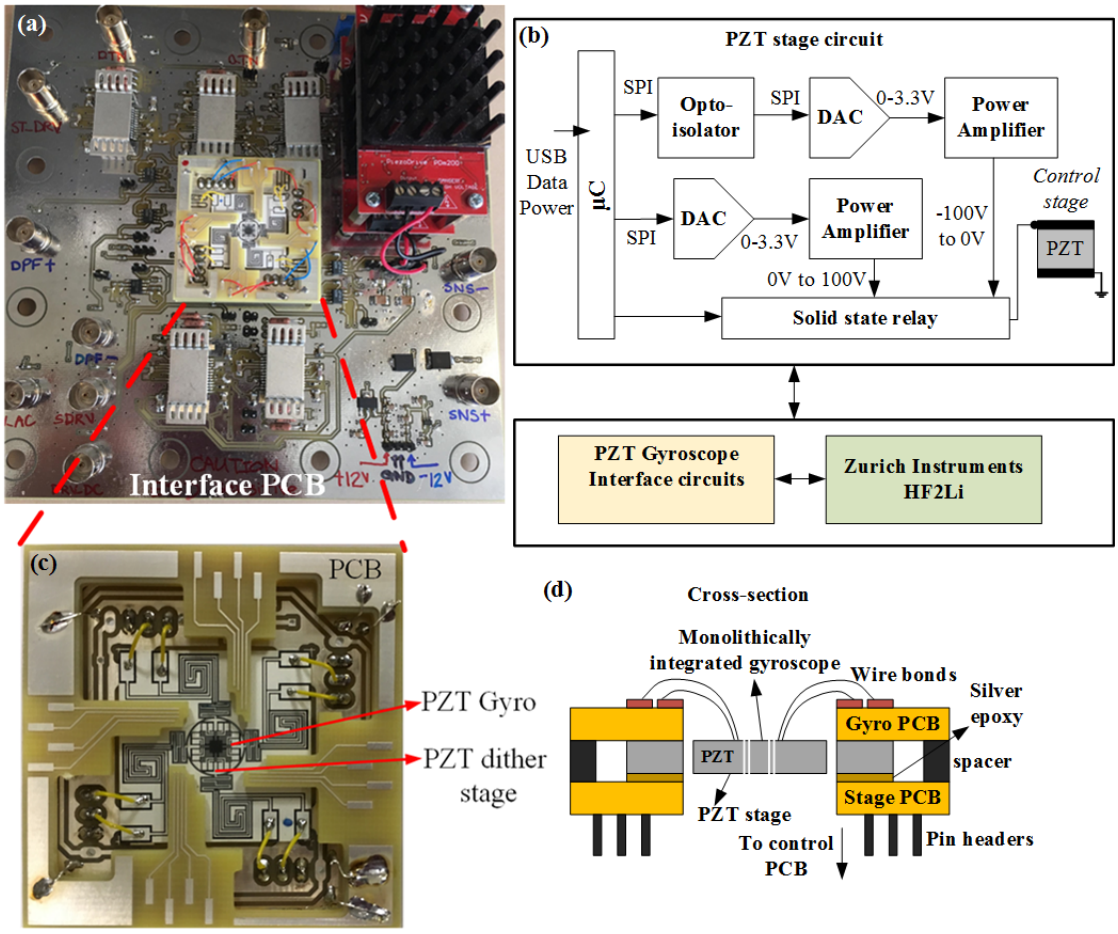

Figure 4.15: System implementation of the monolithic bulk PZT gyroscope and PZT stage device interfaced using custom PCB (a) Shows the system (b) Shows the schematic of the control circuit with the gyroscope interface circuit elaborated in Fig.4.7 (c) Custom DIP implementation of the monolithic device that is detachable from the control PCB (d) Sketch of the cross section of the device on the DIP implementation

voltage constant. Alternatively, for a fixed frequency, the dither rates can also be controlled by applied voltage amplitude. On applying different yaw rates the scale factor is extracted for the gyroscope under test. Details of the PZT calibration stage characteristics and controls are explained in [100, 115]. Also, sinusoidal rate dithering and demodulation of the gyroscope response enables

in-situ quadrature measurement as a function of time, temperature and rate which is useful in feedback control of quadrature.

4.6 Results For The Bulk PZT Monolithic Gyroscope And Stage Device

Fig.4.15 shows the experimental setup for testing the monolithic device. Fig.4.15(d) shows the cross section of the device along with the custom DIP package onto which the device is adhesively bonded. The high frequency PZT gyroscope signals are routed on a separate PCB from the high voltage PZT stage signals.

4.6.1 Bulk PZT stage impedance response

The stage has its fundamental resonance ω_{0s} is around $903Hz$ with the impedance response as shown in Fig.4.16. The picture in the inset shows the in-plane dither mode (θ_z) of the stage at the fundamental resonance. The equivalent circuit model for the stage is extracted from the impedance response. The quality factor of the calibration stage is given by,

$$Q_{stage} = \frac{\omega_{0s} L_r}{R_r} \tag{4.24}$$

The measured Q_{stage} = 900. The stage resonance is much lower than the gyroscope resonance ($112kHz$). The electromechanical coupling coefficient for the PZT stage is given by,

$$k_{31} = \sqrt{\left(\frac{f_a}{f_r}\right)^2 - 1} \tag{4.25}$$

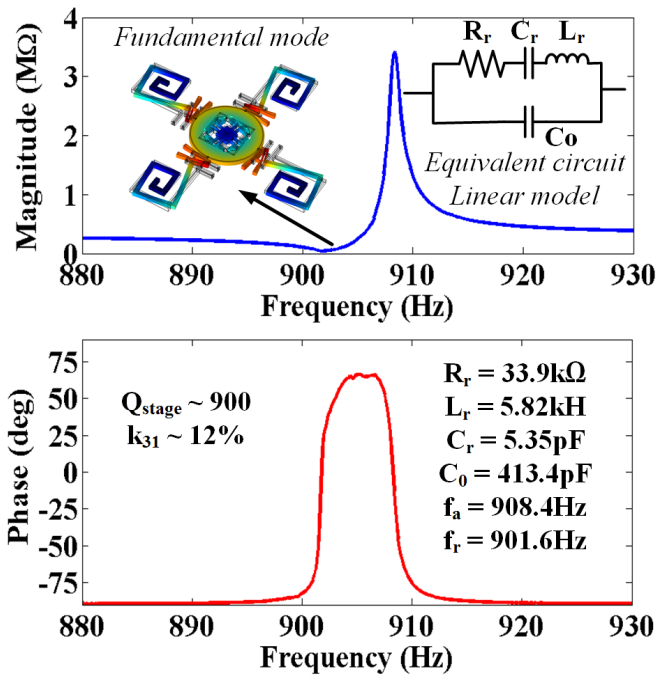

Figure 4.16: Impedance response of bulk PZT calibration stage measured using HP4194A impedance analyzer. Picture in the inset shows the COMSOL^{TM} simulated mode shape of the dominant mode of the bulk PZT stage. An equivalent circuit model is also shown

k_{31} is measured to be 12% for the bulk PZT calibration stage. For the purpose of gyroscope calibration, the stage is operated near DC due to the limited bandwidth ($< 50Hz$) of the bulk PZT gyroscope.

4.6.2 Bulk PZT stage sensitivity

The stage sensitivity to applied voltage is characterized using a Polytec MSA400. Using the in-plane stroboscopic capabilities of the Polytec, the stage in-plane dither for $1Hz$ sinusoidal excitation is measured as a function of PZT stage drive voltage. The measured stage sensitivity is as shown in Fig.4.17.

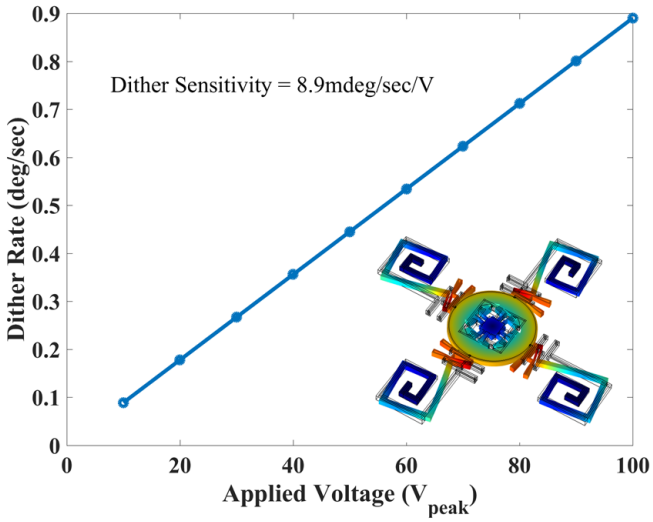

Figure 4.17: Dither stage sensitivity for 1Hz sinusoidal input as a function of voltage measured using in-plane stroboscopy capability with Polytec MSA400

COMSOL^{TM} simulation for in-plane dither is shown in the inset of Fig.4.17. The bulk PZT stage has a in-plane Ω_z dither rate sensitivity of $8.9 mdeg/sec/V$ at applied frequency of $1Hz$. The stage has $< 5 ppm/V$ of out-of-plane motion while operating in the in-plane dither mode. The details of the stage characteristics are discussed in [100, 115]

4.6.3 Frequency response of the monolithically integrated bulk PZT gyroscope

Fig.4.18 shows the frequency response of the gyroscope drive and sense current (velocity) for the monolithic device shown in Fig.4.15. Compared to the gyroscope discussed in section *IV.A, B*, the Q improved by a factor of $\approx$ 10 to 1250 due to the reduction in anchor loses. Additionally, the measured resonance frequency for the monolithically integrated gyroscope is $112.1 kHz$ compared to

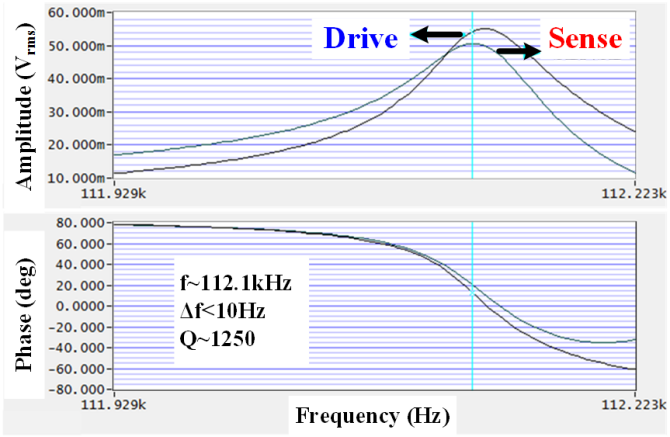

Figure 4.18: Frequency response of the monolithically integrated bulk PZT gyroscope on PZT dither stage for $1V_p$ differential drive of the gyroscope.

previously measured $108kHz$. The anchor loses reduced as the monolithic integration eliminated the need for conductive acrylic layer which is initially used to bond the gyroscope onto PCB. The resonance frequency of the monolithically integrated gyroscope is in agreement to the analytical calculations in Table.4.1 due to the improved anchor.

4.6.4 Sensitivity of the monolithically integrated bulk PZT gyroscope

As shown in frequency response of the monolithically integrated bulk PZT gyroscope on stage in Fig.4.18, the gyroscope in nearly mode-matched with a frequency split of $\approx$ $10Hz$. Fig.4.19 shows the scale factor measurement of the gyroscope using stage dither sweep. The measured scale factor and bias of the gyroscope are $3.4mV/deg/s$ and $0.31mV$ respectively. Higher angular rates (Ω_z) can be applied to the gyroscope by sweeping the dither frequency at a fixed

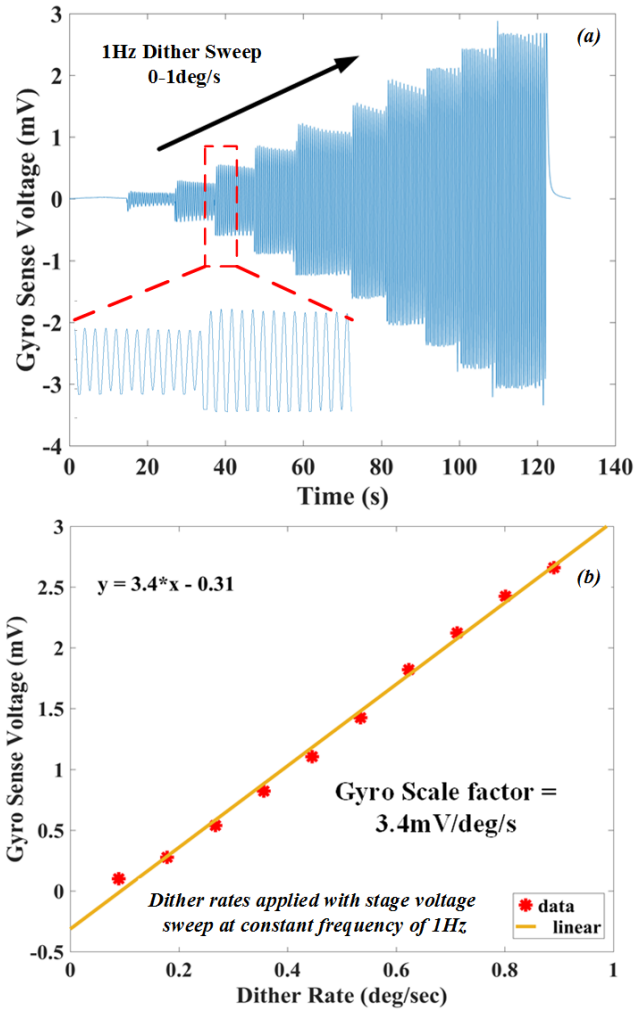

Figure 4.19: PZT gyroscope response to dither: (a) Shows the gyroscope response to dither rate on sweeping the dither stage input voltage for constant 1Hz frequency. (b) Scale factor of the gyroscope measured for $1V_p$ gyroscope drive with TIA gain $10k\Omega$

stage drive voltage. In the current operating configuration of closed loop drive and open loop sense, the gyroscope bandwidth is limited to the $\beta_y < 45Hz$. Due to the limited bandwidth of operation for this configuration, the dither stage applied voltage is swept and operated at a constant $1Hz$ dither frequency. For frequency based control of dither, one can operate the sense in closed loop in force-to-rebalance mode [104, 109] for improving the gyroscope bandwidth.

Compared to the gyroscope discussed in section *IV.B* (Fig.4.10), the monolithically integrated gyroscope here has reduced quadrature error and mode split due to tuning. Hence, we observe lower bias drift ($< 0.2 deg/s$) in the time domain response of the gyroscope (Fig.4.19). Here the gyroscope sense response is measured using a TIA with gain of $10k\Omega$. The unamplified gyroscope sensitivity is $0.34\mu A/deg/s$, which is $\approx$ 13 times higher than analytical estimation in Table.4.1 due to near mode-matching between the drive and sense mode.

4.7 Conclusion

In this work a bulk PZT Z-axis gyroscope was demonstrated and the non-linear behavior of the resonator was explored. The sensitivities of gyroscope frequency and quadrature tune loops to DC voltages was measured. The bulk PZT gyroscope is also monolithically integrated into a bulk PZT calibration stage for in-situ calibration of the gyroscope. The calibration stage system can extract the gyroscope input-output characteristics such as in-run scale factor and bias etc. Closed loop control of the drive and sense resonator ensuring mode matching of drive and sense resonators, along with scale factor, bias and quadrature compensations are necessary for long term stable gyroscopes. Low noise front end electronics implemented on FPGA or custom ASIC for the control loops of the gyroscope and PZT stage is necessary to measure the noise performance of the bulk PZT gyroscope.

CHAPTER 5

MONOLITHIC 2-AXIS IN-PLANE PZT LATERAL BIMORPH ENERGY HARVESTER WITH DIFFERENTIAL OUTPUT

5.1 Introduction

One of the key challenges in energy harvesting is the ability to generate electrical energy from vibration regardless of its direction. This can be achieved in part by manual packaging of single axis harvesters oriented along different directions or wafer-level integration of energy harvesters which are sensitive along different axis [116]. While both approaches need additional circuitry to combine the generated powers, manual assembly approach also suffers from increased system volume and cost. For piezoelectric energy harvesters,

$$Power(f_r) \propto \frac{k_{31}^2 Q^2 m_{eff} a^2}{f_r} \tag{5.1}$$

where, a is the applied acceleration and f_r the resonance frequency [117]. Recent work on thin film PZT harvesters such as sol-gel, sputtered AlN and also thinned PZT on silicon [117], which have reported good quality factor Q (32 – 1800) and k_{31}^2 (0.05 – 0.35), generally aim to reduce resonance frequencies to improve Normalized Power Densities (NPD in $\mu Watt/mm^3 g^{-2}$) [117]. Although high values for NPD ($6.309 \mu Watt/mm^3 g^{-2}$ [117]) are reported in the literature, most devices rely on resonant structures sensitive along a single sensitive axis (generally out of plane) and are not monolithic. High NPD and low resonance frequency is achieved by steps requiring die-level alignment and bonding of high density materials, such as tungsten in [117], which leads to a multi-step process flow. This work uses a single-step, laser-micro machined, spiral

shaped beam structure to get around single-axis limitation while still achieving high normalized power densities at low resonance frequencies. The energy harvester is fabricated using a laser micromachining process, which is a subtractive process requiring no additional deposition. The entire device is fabricated using direct-write micro patterning technique involving precision removal of PZT and/or electrode material [118]. The constraints considered for the energy harvester design are as summarized in Fig.5.1. The design aims to maximize power output for a given volume for lower resonance frequency while being responsive to any in-plane ($X - Y$) vibration. The operation of the key transducer element of the 2-axis bulk-micro machined PZT harvester is sketched in Fig.5.2 The design exploits lateral bimorphs [118], generating differential voltage from in-plane motion at high efficiencies. The monolithic nature of the device eliminates the need for additional circuitry to combine the outputs of multiple harvesters for the purpose of multi-directional operation.

5.2 Design

The vibrational energy harvester has the lateral PZT bimorph as its fundamental building block [118]. The lateral bimorph generates differential voltages for in-plane bending due to equal and opposite tensile and compressive strains as shown in Fig.5.2 and owing to voltage coefficient g_{31}. The equal and opposite polarity voltages generated on top electrodes due to compressive and tensile stress can be useful, post rectification, in analog electronics that require symmetric $\pm V$ supply for operation, which is otherwise realized by having additional capacitors and inductors. Here, two designs are tested. First, the performance of a single bimorph element as energy harvester is characterized. For this pur-

pose, a common design is chosen that includes lateral bimorph with mass on the tip, as shown in Fig.5.3, all cut out from a single PZT substrate. The mass at the tip is chosen so as to lower the resonance frequency while still maintaining the fundamental resonance to be in-plane. Next, a second device structure with a spiral design as shown in Fig.5.5 is explored. This design allows improvements in performance and metrics described in Fig.5.4. PZT-4 used in both designs is chosen for its higher coupling coefficients and Curie temperature ($324C$), the latter of which is important to minimize any potential heat induced local depolarization of bulk PZT during laser micromachining. Furthermore, bulk PZT is also a good choice as a tip mass to lower resonance frequency due to its high density.

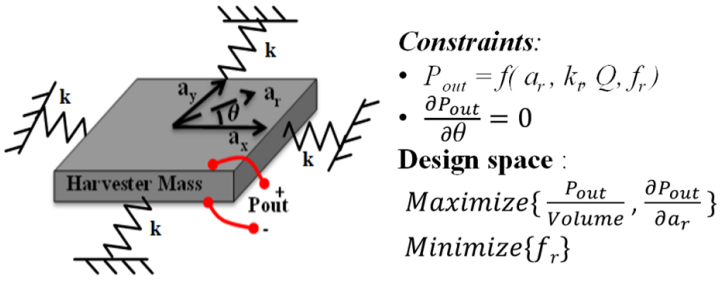

Figure 5.1: Metrics considered in the design of a 2-axis energy harvester under arbitrary planar acceleration a_r. k_t: electromechanical coupling coefficient, f_r: resonance frequency, k: spring constant.

5.3 Fabrication

The energy harvester is fabricated using laser micromachining, which involves precision removal of PZT and/or electrode material [118], by repeated and selective scanning of a $355nm$ UV laser (LPKF ProtoLaser U) on $0.5mm$ thick PZT-4 plates. The scan speeds are optimized for through cut of PZT and/or metal

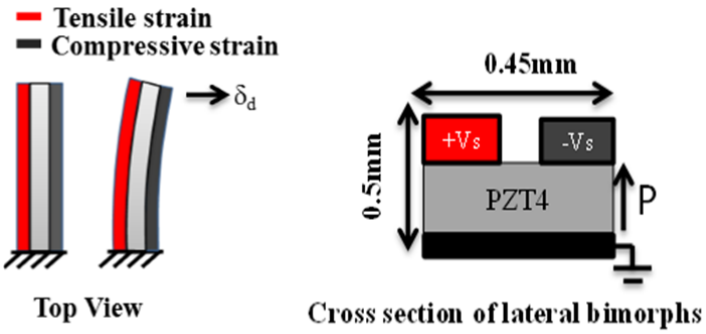

Figure 5.2: Basic building block of the harvester

without depoling piezoelectric regions that are part of the device. The process can achieve an aspect ratio of 1:5 (0.1*mm* wide, 0.5*mm* thick) bulk PZT structures. For the energy harvester, PZT-4 plates with silver as top and bottom electrodes are laser-machined [118, 119] to form 0.45*mmwide* and 0.5*mm* thick lateral bimorphs, with electrode patterns as shown in Fig.5.2. Typical cut rates for PZT are 16.6$\mu m/min$ in thickness, and 250mm/s laterally leading to beams with minimum width of 100μm. After laser-micromachining, the PZT structures were cleaned with acetone followed by IPA (Iso-Propyl Alcohol) to clear any debris around the processed regions. Described process enables both the active energy harvesting element and the mass to be cut out from single PZT substrate.

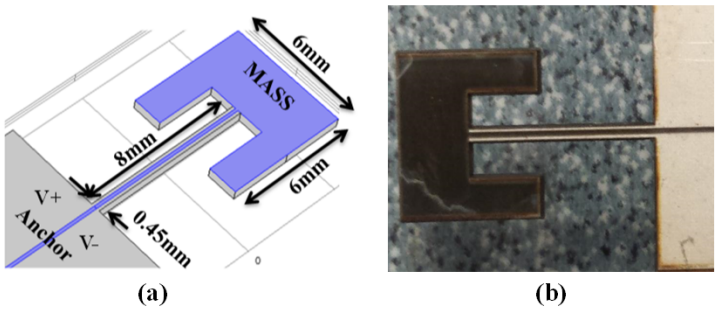

Figure 5.3: A generic energy harvester design with lateral PZT bimorph with tip mass. (a) Schematic of the device (b) Fabricated device on PCB

5.4 Modeling And Experimental Results

5.4.1 Lateral bimorph with tip mass

Impedance analysis

For characterization, the device shown in Fig.5.3(b), which is adhered to PCB with silver acrylic paint, is used. This also ensured electrical contact to bottom electrode (ground). The two electrodes were then wire-bonded to pads on the PCB. The impedance response of the device is shown in Fig.5.4. The device has a resonance frequency of 626.5Hz and the mode is simulated to be in-plane using COMSOL with a measured Q-factor of 45 with k_t^2 3.55%.

Power output

The device is clamped on a shaker table to measure the peak power for 1g acceleration at its resonance. The device generates 4.5$\mu Watts$ when connected across a load resistor of 198$k\Omega$, which is found to be the optimal load for maximum

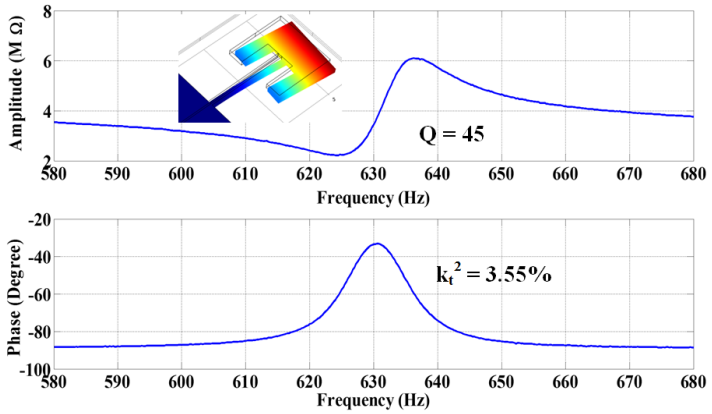

Figure 5.4: Impedance response of the lateral bimorph with a tip mass. Plot shows resonance at $626.5Hz$ measured using impedance analyzer HP4194A. The Q factor is measured to be 45. The mode is simulated to be in-plane using COMSOL^{TM} with the displacement contour shown in the inset.

power. The corresponding normalized power density is $0.305\mu Watts/mm^3g^{-2}$.

5.4.2 Spiral energy harvester

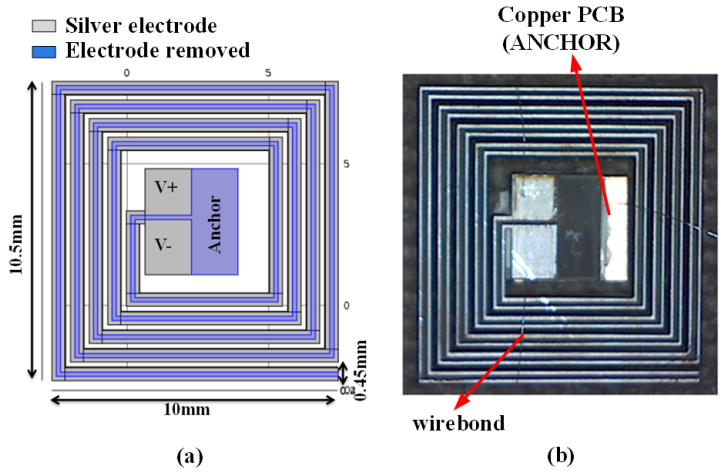

Figure 5.5: Two axis spiral PZT energy harvester.(a) Schematic (b) Fabricated device anchored to a PCB

For improvement in NPD, Q-factor and to achieve rotational invariance, the

spiral shaped energy harvester is pursued as shown in Fig.5.5. The lateral bimorphs were micromachined in the form of a rectangular spiral coil of volume $26mm^3$. Cascading of several such lateral bimorphs in a spiral fashion enables the device to be sensitive to any in-plane vibrations, making the energy harvesters sensitive axis rotationally invariant.

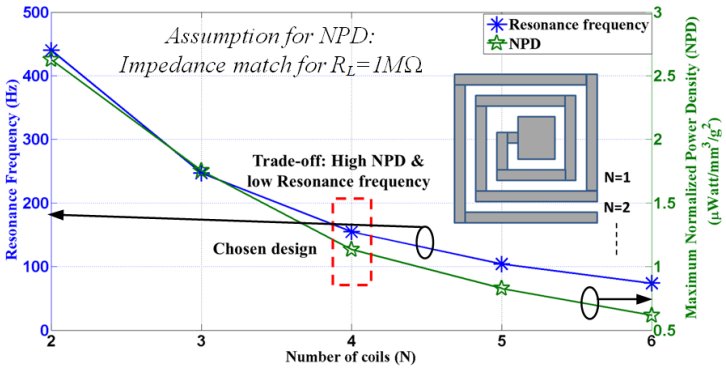

Figure 5.6: Simulated relations between NPD, resonance frequency versus number of coils N. Coils (N) is as shown in inset sketch

Design optimization

Near rotational symmetry of the spiral shaped beam structures allows the sensitive axis of the harvester to be rotationally invariant in-plane. Fig.5.6 shows the simulated curves for optimal spiral design as a function of number of coils, N. Also for $N < 2$, it is seen from simulations that the fundamental mode is no longer in-plane. $N = 4$ is chosen due to the trade-off between resonance frequency and NPD.

Impedance analysis

It is shown in [120] that the energy harvesters load, peak power and its frequency is strongly dependent on K^2Q and is referred to as the coupling efficiency figure of merit. This is evident from the expression for impedance of the device, which is essential for calculating resonance frequency and the optimal load to be connected to the energy harvester for maximum power transfer. The impedance Z of the device can be expressed as, [120]

$$Z(j\omega) = \frac{-j}{\omega_0 C} \frac{j\frac{\omega}{\omega_0} + Q\left(1 - \frac{\omega^2}{\omega_0^2}\right)}{\frac{\omega}{\omega_0}\left(\frac{j\omega}{\omega_0} + Q\left(1 - \frac{\omega^2}{\omega_0^2}\right) + QK^2\right)} \tag{5.2}$$

where, ω_0 is the resonance frequency, K is the generalized electromechanical coupling coefficient ($K = k_{31}$,is experimentally determined to be 2.71%), and C is the capacitance of the device $3nF$. The measurements were done using impedance analyzer and further verified with lock-in amplifier frequency sweeps which yielded an in-plane Q-factor of 129.5. Analytical expression for Z is in close agreement to experimentally determined impedance curve shown in Fig.5.7(a). Fig.5.7(b) shows the equivalent circuit which closely models the device [120]. For maximum power transfer from the piezoelectric vibrational energy harvester, load impedance must be the complex conjugate of the device impedance ($Z = Zload*$), which is purely real at resonance ($163.5Hz$) that corresponds to zero phase. The impedance at this frequency is $1M\Omega$ as seen in Fig.5.7(a). Hence the load resistance is chosen to be the same. The fabricated spiral energy harvester here falls under the strongly coupled case [120] of $K^2Q > 2$ ($K^2Q = 3.88$), with two operation frequencies for maximum power, corresponding to $163.5Hz$ and $165.5Hz$, where impedance has zero phase for the tested de-

vice. In-plane nature of the mode shape is verified by FEM in COMSOL^{TM} as seen in Fig.5.8, which shows the surface potential distribution for $1g$ acceleration along the devices X axis. Similar results were obtained for acceleration applied along any axis in $X-Y$ plane. The differential strain due to equal and opposite compression and tension during in-plane bending of the cascaded bimorphs generates differential voltages. The strain is maximum at the L-shaped corners, which act as apparent anchors. This is shown in the zoomed picture at the inset of Fig.5.8. It is seen in simulations that the contributions to strain/voltage from subsequent outer rings reduce, which is in agreement with the results of Fig.5.6.

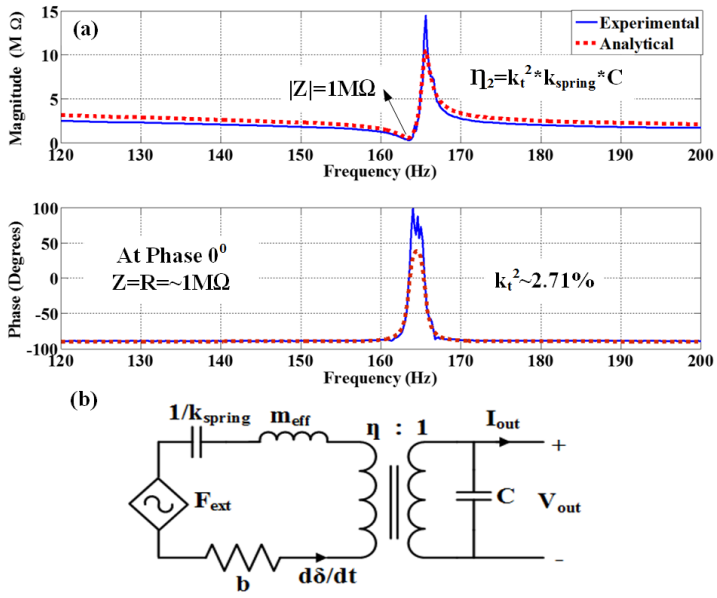

Figure 5.7: Impedance response of the device. (a) Plot showing resonance frequency of $163.5Hz$ measured using Impedance analyzer (HP4194A) and the analytical curve for Z with extracted parameters. The measured Q factor for the mode is 129.5 (b) Shows the equivalent circuit model of the device.

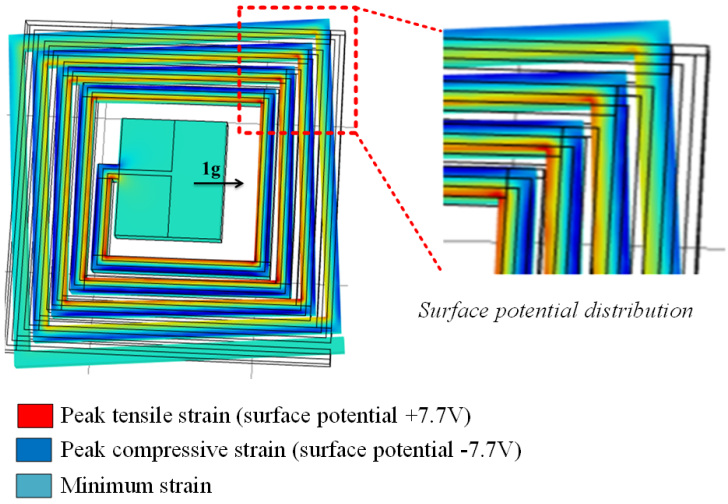

Figure 5.8: COMSOL^{TM} simulation of mode shape and the associated surface potential profile. Simulation shows peak open circuit voltage is $7.7V$ for $1g$ acceleration along X-axis of the device at the simulated device resonance frequency of $155.3Hz$

Power output

The experimental setup to characterize the energy harvester is shown in Fig.5.9. The device is clamped on a commercial shaker table from Vibrations Research at varying angular orientations to measure output versus shaker frequency, amplitude, and harvester mounting angle. Experiments are performed for both $1M\Omega$load and at near infinite load by measuring open-circuit voltages using a JFET buffer to cancel the effect of oscilloscope finite input impedance. Experimental data show an average voltage of $6.4V_{pp}$ across $1M\Omega$ load. Table.5.1 lists the relatively constant output (within ±7.4%) and power as a function of the planar orientation with respect to vibration. The NPD of the device is measured to be $0.89\mu Watt/mm^3g^{-2}$. Compared to the simple bimorph energy harvester with tip mass, the spiral energy harvester has 2.9 times higher NPD because of higher Q and lower resonance frequency. The maximum power generated for $1M\Omega$ load is $23.14\mu Watt$ for applied acceleration of $1g$ at $163.5Hz$.

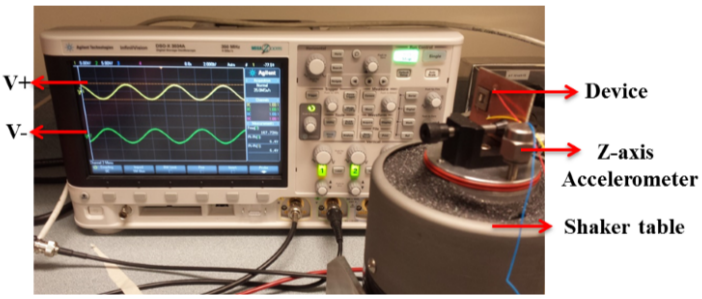

Figure 5.9: Experimental setup showing the device mounted vertically on a Z-axis shaker table to excite the devices in-plane resonance. The device is mounted at different angles about its XY plane to test its dependence on vibration orientation.

Table 5.1: Measured voltages at resonance frequency for $1g$ applied acceleration for different mount angles about the XY plane of the device on the shaker table.*(Measurements were done with JFET buffer to measure open circuit voltages generated for applied 1g accelerations to compare with COMSOL model (Fig.5.8))

Metric	JFET buffer* $V_{pp}(V)$	$1M\Omega$ load $V_{pp}(V)$	Power ($\mu Watts$)
X	±8	±6.8	23.12
20^0	±7.8	±6.4	20.48
45^0	±7.6	±6.3	19.85
70^0	±7.6	±6.3	19.85
Y	±7.6	±6.8	23.12

5.5 Conclusion

A piezoelectric vibration energy harvester whose sensitive axis is shown to be rotationally symmetric with power output variations to within 7.4% is presented. Fabricated using only a single step laser micromachining of bulk PZT, this harvester has a resonance frequency of $163.5Hz$ and an NPD of $0.89\mu Watt/mm^3g^{-2}$. COMSOL^{TM} simulation results for the in-plane mode fre-

quency of 155.3Hz matches experimental data to within 5%. Such a power harvester could be useful in applications where in-plane motion directionality changes with time such as motion of a hovering aircraft or on top of a head mounted helmet display.

APPENDIX A

MATLAB CODE FOR NORIS

```
%pixel size  0.08"x0.12"->3200x2400 pixels
%Output : 640x480 pixels (combining 5 pixels)

frames = length(I);
usfac = 100;
ref = fft2(I(:,:,1)); % Reference diffraction pattern
    image

for k=2:1:frames-1
[output Greg] = dftregistration(ref,fft2(I(:,:,k)),usfac);
imager_shift_Y(k) = output(3);
imager_shift_X(k) = output(4);
r(k) = sqrt(imager_shift_Y(k)^2+imager_shift_X(k)^2);
end
r = r.*5e-6;
figure
plot(time(1:length(r)),r)

function [output Greg] = dftregistration(buf1ft,buf2ft,
    usfac)

% function [output Greg] = dftregistration(buf1ft,buf2ft,
    usfac);
```

```
% Efficient subpixel image registration by
    crosscorrelation.

%This code  gives the same precision as the FFT upsampled
    cross correlation in a  small fraction of the
    computation time and with reduced memory requirements.

%It obtains an initial estimate of the crosscorrelation
    peak by an FFT and then refines the shift estimation by
     upsampling the DFT  only in a small neighborhood of
    that estimate by means of a  matrix-multiply DFT. With
    this procedure all the image points are used to %
    compute the upsampled crosscorrelation.

% Manuel Guizar - Dec 13, 2007

% Portions of this code were taken from code written by
    Ann M. Kowalczyk  and James R. Fienup.
%J.R. Fienup and A.M. Kowalczyk, "Phase retrieval for a
    complex-valued  object by using a low-resolution image
    ," J. Opt. Soc. Am. A 7, 450-458 (1990).

% Citation for this algorithm:
%Manuel Guizar-Sicairos, Samuel T. Thurman, and James R.
    Fienup, "Efficient subpixel image registration
```

```
    algorithms," Opt. Lett. 33, 156-158 (2008).

% Inputs
% buf1ft Fourier transform of reference image,
%  DC in (1,1)   [DO NOT FFTSHIFT]
% buf2ft Fourier transform of image to register, DC in
    (1,1) [DO NOT FFTSHIFT]
% usfac  Upsampling factor (integer). Images will be
    registered to   within 1/usfac of a pixel.
% For example usfac = 20 means the images will be
    registered within 1/20 of a pixel. (default = 1)

% Outputs
% output =  [error,diffphase,net_row_shift,net_col_shift]
% error Translation invariant normalized RMS error between
     f and g diffphase
% Global phase difference between the two images (should
    be zero if images are non-negative).
% net_row_shift net_col_shift Pixel shifts between images
% Greg (Optional) Fourier transform of registered version
    of buf2ft,the global phase difference is compensated
    for.

% Default usfac to 1
if exist('usfac')~=1, usfac=1; end
```

```
% Compute error for no pixel shift
if usfac == 0,
    CCmax = sum(sum(buf1ft.*conj(buf2ft)));
    rfzero = sum(abs(buf1ft(:)).^2);
    rgzero = sum(abs(buf2ft(:)).^2);
    error = 1.0 - CCmax.*conj(CCmax)/(rgzero*rfzero);
    error = sqrt(abs(error));
    diffphase=atan2(imag(CCmax),real(CCmax));
    output=[error,diffphase];

% Whole-pixel shift - Compute crosscorrelation by an IFFT
   and locate the peak
elseif usfac == 1,
    [m,n]=size(buf1ft);
    CC = ifft2(buf1ft.*conj(buf2ft));
    [max1,loc1] = max(CC);
    [max2,loc2] = max(max1);
    rloc=loc1(loc2);
    cloc=loc2;
    CCmax=CC(rloc,cloc);
    rfzero = sum(abs(buf1ft(:)).^2)/(m*n);
    rgzero = sum(abs(buf2ft(:)).^2)/(m*n);
    error = 1.0 - CCmax.*conj(CCmax)/(rgzero(1,1)*rfzero
       (1,1));
    error = sqrt(abs(error));
    diffphase=atan2(imag(CCmax),real(CCmax));
```

```
    md2 = fix(m/2);
    nd2 = fix(n/2);
    if rloc > md2
        row_shift = rloc - m - 1;
    else
        row_shift = rloc - 1;
    end

    if cloc > nd2
        col_shift = cloc - n - 1;
    else
        col_shift = cloc - 1;
    end
    output=[error, diffphase, row_shift, col_shift];

% Partial-pixel shift
else

% First upsample by a factor of 2 to obtain initial
   estimate
% Embed Fourier data in a 2x larger array
    [m,n]=size(buf1ft);
    mlarge=m*2;
    nlarge=n*2;
    CC=zeros(mlarge,nlarge);
```

```
    CC(m+1-fix(m/2):m+1+fix((m-1)/2),n+1-fix(n/2):n+1+fix
        ((n-1)/2)) = ...
          fftshift(buf1ft).*conj(fftshift(buf2ft));

% Compute crosscorrelation and locate the peak
    CC = ifft2(ifftshift(CC)); % Calculate cross-
        correlation
    [max1,loc1] = max(CC);
    [max2,loc2] = max(max1);
    rloc=loc1(loc2);cloc=loc2;
    CCmax=CC(rloc,cloc);

% Obtain shift in original pixel grid from the position of
    the crosscorrelation peak
    [m,n] = size(CC); md2 = fix(m/2); nd2 = fix(n/2);
    if rloc > md2
        row_shift = rloc - m - 1;
    else
        row_shift = rloc - 1;
    end
    if cloc > nd2
        col_shift = cloc - n - 1;
    else
        col_shift = cloc - 1;
    end
    row_shift=row_shift/2;
```

```
    col_shift=col_shift/2;

% If upsampling > 2, then refine estimate with %matrix
    multiply DFT
    if usfac > 2,
      %%% DFT computation %%%
 % Initial shift estimate in upsampled grid
        row_shift = round(row_shift*usfac)/usfac;
        col_shift = round(col_shift*usfac)/usfac;
        dftshift = fix(ceil(usfac*1.5)/2); %% Center of
           output array at dftshift+1
 % Matrix multiply DFT around the current shift estimate
        CC = conj(dftups(buf2ft.*conj(buf1ft),ceil(usfac
           *1.5),ceil(usfac*1.5),usfac,...
             dftshift-row_shift*usfac,dftshift-col_shift*
                usfac))/(md2*nd2*usfac^2);
% Locate maximum and map back to original pixel grid
        [max1,loc1] = max(CC);
        [max2,loc2] = max(max1);
        rloc = loc1(loc2); cloc = loc2;
        CCmax = CC(rloc,cloc);
        rg00 = dftups(buf1ft.*conj(buf1ft),1,1,usfac)/(md2
           *nd2*usfac^2);
        rf00 = dftups(buf2ft.*conj(buf2ft),1,1,usfac)/(md2
           *nd2*usfac^2);
        rloc = rloc - dftshift - 1;
```

```
            cloc = cloc - dftshift - 1;
            row_shift = row_shift + rloc/usfac;
            col_shift = col_shift + cloc/usfac;

    % If upsampling = 2, no additional pixel shift refinement
        else
            rg00 = sum(sum( buf1ft.*conj(buf1ft) ))/m/n;
            rf00 = sum(sum( buf2ft.*conj(buf2ft) ))/m/n;
        end
        error = 1.0 - CCmax.*conj(CCmax)/(rg00*rf00);
        error = sqrt(abs(error));
        diffphase=atan2(imag(CCmax),real(CCmax));
     % If its only one row or column the shift along that
        dimension has no effect. We set to zero.
        if md2 == 1,
            row_shift = 0;
        end
        if nd2 == 1,
            col_shift = 0;
        end
        output=[error,diffphase,row_shift,col_shift];
    end

    % Compute registered version of buf2ft
    if (nargout > 1)&&(usfac > 0),
        [nr,nc]=size(buf2ft);
```

```
    Nr = ifftshift([-fix(nr/2):ceil(nr/2)-1]);
    Nc = ifftshift([-fix(nc/2):ceil(nc/2)-1]);
    [Nc,Nr] = meshgrid(Nc,Nr);
    Greg = buf2ft.*exp(i*2*pi*(-row_shift*Nr/nr-col_shift*
       Nc/nc));
    Greg = Greg*exp(i*diffphase);
elseif (nargout > 1)&&(usfac == 0)
    Greg = buf2ft*exp(i*diffphase);
end
return

function out=dftups(in,nor,noc,usfac,roff,coff)
% function out=dftups(in,nor,noc,usfac,roff,coff);
% Upsampled DFT by matrix multiplies, can compute an
   upsampled DFT in just a small region.
% usfac Upsampling factor (default usfac = 1)
% [nor,noc]  Number of pixels in the output upsampled DFT,
    in  units of upsampled pixels (default = size(in))
% roff, coff    Row and column offsets, allow to shift the
    output array to  a region of interest %on the DFT (
   default = 0)
% Recieves DC in upper left corner, image center must be
   in (1,1)
% Manuel Guizar - Dec 13, 2007
% Modified from dftus, by J.R. Fienup 7/31/06
```

```
% This code is intended to provide the same result as if
    the following  operations were performed
%    - Embed the array "in" in an array that is usfac times
     larger in each  dimension. ifftshift to bring the
    center of the image to (1,1).
%    - Take the FFT of the larger array
%    - Extract an [nor, noc] region of the result. Starting
     with the [roff+1 coff+1] element.

% It achieves this result by computing the DFT in the
    output array without the need to zeropad. £Much faster
    and memory efficient than the
% zero-padded FFT approach if [nor noc] are much smaller
    than [nr*usfac nc*usfac]

[nr,nc]=size(in);
% Set defaults
if exist('roff')~=1, roff=0; end
if exist('coff')~=1, coff=0; end
if exist('usfac')~=1, usfac=1; end
if exist('noc')~=1, noc=nc; end
if exist('nor')~=1, nor=nr; end
% Compute kernels and obtain DFT by matrix products
kernc=exp((-i*2*pi/(nc*usfac))*( ifftshift([0:nc-1]).' -
    floor(nc/2) )*( [0:noc-1] - coff ));
```

```
kernr=exp((-i*2*pi/(nr*usfac))*( [0:nor-1].' - roff )*(
    ifftshift([0:nr-1]) - floor(nr/2)  ));
out=kernr*in*kernc;
return
```

BIBLIOGRAPHY

[1] C. D. Rahn, S. A. Tadigadapa, R. Street, and C. D. Rahn, "High Performance Piezoelectric Actuators And Wings Distribution A - Approved for Public Release," vol. 298, no. 0704, 2012.

[2] M. Wehner, R. L. Truby, D. J. Fitzgerald, B. Mosadegh, G. M. Whitesides, J. A. Lewis, and R. J. Wood, "An integrated design and fabrication strategy for entirely soft, autonomous robots," *Nature Publishing Group*, vol. 536, 2016.

[3] J. S. Pulskamp, R. G. Polcawich, R. Q. Rudy, S. S. Bedair, R. M. Proie, T. Ivanov, and G. L. Smith, "Piezoelectric PZT MEMS Technologies For Small-Scale robotics and RF Applications," *MRS bulletin*, vol. 37.11, pp. 1062–1070, 2012.

[4] J. Gubbi, R. Buyya, S. Marusic, and M. Palaniswami, "Internet of Things (IoT): A vision, architectural elements, and future directions," *Future Generation Computer Systems*, vol. 29, no. 7, pp. 1645–1660, 2013.

[5] Hooker and M. W., "Properties of PZT-Based Piezoelectric Ceramics Between -150 and 250 C," 1998.

[6] R. Wood, E. Steltz, and R. Fearing, "Optimal energy density piezoelectric bending actuators," *Sensors and Actuators A: Physical*, vol. 119, no. October 2004, pp. 476–488, 2005.

[7] E. E. Aktakka and K. Najafi, "A Micro Inertial Energy Harvesting Platform With Self-Supplied Power Management Circuit for Autonomous Wireless Sensor Nodes," *IEEE Journal of Solid-State Circuits*, vol. 49, no. 9, pp. 2017–2029, sep 2014. [Online]. Available: http://ieeexplore.ieee.org/lpdocs/epic03/wrapper.htm?arnumber=6845376

[8] Y.-C. Hsu, C.-C. Wu, C.-C. Lee, G. Cao, and I. Shen, "Demonstration and characterization of PZT thin-film sensors and actuators for meso- and micro-structures," *Sensors and Actuators A: Physical*, vol. 116, no. 3, pp. 369–377, oct 2004. [Online]. Available: http://linkinghub.elsevier.com/retrieve/pii/S0924424704003541

[9] G. Gerlach, G. Suchaneck, R. Köhler, T. Sandner, P. Padmini, R. Krawietz, W. Pompe, J. Frey, O. Jost, and A. Schönecker, "Properties of sputter

and Sol-Gel deposited PZT thin films for sensor and actuator applications: Preparation, stress and space charge distribution, self poling," *Ferroelectrics*, vol. 230, no. 1, pp. 109–114, may 1999. [Online]. Available: http://www.tandfonline.com/doi/abs/10.1080/00150199908214904

[10] N. Sinha, G. E. Wabiszewski, R. Mahameed, V. V. Felmetsger, S. M. Tanner, R. W. Carpick, G. Piazza, G. E. . Wabiszewski, V. V. . Felmetsger, S. M. . Tanner, and R. W. . Carpick, "Piezoelectric aluminum nitride nanoelectromechanical actuators," *Appl. Phys. Lett. Departmental Papers (MEAM*, vol. 95, no. 053106, 2009. [Online]. Available: http://repository.upenn.edu/meam_papers http://link.aip.org/link/?APPLAB/95/053106/1 http://repository.upenn.edu/meam_papers/165

[11] W. Hackenberger, J. Luo, and K. Snook, "Advanced Single Crystal Piezoelectric Transducers for Naval Sonar and Medical Ultrasound Applications," *The Journal of the Acoustical Society of America*, vol. 123, no. 5, pp. 3115–3115, may 2008. [Online]. Available: http://asa.scitation.org/doi/10.1121/1.2933014

[12] K. Oldham, J. Pulskamp, R. Polcawich, and M. Dubey, "Thin-Film PZT Lateral Actuators With Extended Stroke," *Journal of Microelectromechanical Systems*, vol. 17, no. 4, pp. 890–899, aug 2008. [Online]. Available: http://ieeexplore.ieee.org/document/4570438/

[13] H. K. R. Kommepalli, K. Mateti, C. D. Rahn, and S. A. Tadigadapa, "Piezoelectric T-Beam Actuators," *Journal of Mechanical Design*, vol. 133, no. 6, p. 061003, 2011.

[14] Y. A. Genenko, J. Glaum, and M. J. Hoffmann, "Mechanisms of aging and fatigue in ferroelectrics," *Materials Science and Engineering: B*, vol. 192, pp. 52–82, 2015.

[15] S. Nadig, S. Ardanuç, and A. Lal, "Monolithic piezoelectric in-plane motion stage with low cross-axis-coupling," in *2014 IEEE 27th International Conference on Micro Electro Mechanical Systems (MEMS)*. IEEE, 2014, pp. 524–527.

[16] ——, "Planar laser-micro machined bulk pzt bimorph for in-plane actuation," in *2013 Joint IEEE International Symposium on Applications of Ferroelectric and Workshop on Piezoresponse Force Microscopy (ISAF/PFM)*. IEEE, 2013, pp. 152–155.

[17] S. Nadig, S. Ardanuc, and A. Lal, "Self-calibration compatible Z-axis bulk PZT vibratory gyroscope," in *2015 Transducers - 2015 18th International Conference on Solid-State Sensors, Actuators and Microsystems (TRANSDUCERS)*. IEEE, jun 2015, pp. 1117–1120. [Online]. Available: http://ieeexplore.ieee.org/document/7181123/

[18] V. Pinrod, L. Pancoast, B. Davaji, S. Lee, R. Ying, A. Molnar, and A. Lal, " Zero-Power Sensors With Near-Zero-Power Wakeup Switches For Reliable Sensor Platforms," in *2017 IEEE 30th International Conference on Micro Electro Mechanical Systems (MEMS)*.

[19] S. Nadig, S. Ardanuc, and A. Lal, "Monolithic 2-axis in-plane PZT lateral bimorph energy harvester with differential output," in *2015 28th IEEE International Conference on Micro Electro Mechanical Systems (MEMS)*. IEEE, jan 2015, pp. 1129–1132. [Online]. Available: http://ieeexplore.ieee.org/document/7051163/

[20] X. Bao, Y. Bar-Cohen, S. Sherrit, M. Badescu, and T. Shrout, "High temperature piezoelectric drill."

[21] T. Li and Y. B. Gianchandani, "A Die-Scale Micromachining Process For Bulk PZT Aand Its Applications To In-Plane Actuators."

[22] E. E. Aktakka, R. L. Peterson, and K. Najafi, "A 6-DOF piezoelectric micro vibratory stage based on multi-axis distributed-electrode excitation of PZT/Si unimorph T-beams," in *2013 Transducers & Eurosensors XXVII: The 17th International Conference on Solid-State Sensors, Actuators and Microsystems (TRANSDUCERS & EUROSENSORS XXVII)*. IEEE, jun 2013, pp. 1583–1586. [Online]. Available: http://ieeexplore.ieee.org/document/6627085/

[23] M. Brissaud, S. Ledren, and P. Gonnard, "Modelling of a cantilever non-symmetric piezoelectric bimorph," *Journal of Micromechanics and Microengineering*, vol. 13, no. 6, pp. 832–844, 2003.

[24] R. Dunsch and J. M. Breguet, "Unified mechanical approach to piezoelectric bender modeling," *Sensors and Actuators, A: Physical*, 2007.

[25] L. Q. Yao, J. G. Zhang, L. Lu, and M. O. Lai, "Nonlinear dynamic characteristics of piezoelectric bending actuators under strong applied electric field," *Journal of Microelectromechanical Systems*, vol. 13, no. 4, pp. 645–652, 2004.

[26] S. Li, W. Cao, and L. E. Cross, "The extrinsic nature of nonlinear behavior observed in lead zirconate titanate ferroelectric ceramic," 1991.

[27] Y. Jia, S. Du, and A. A. Seshia, "Twenty-Eight Orders of Parametric Resonance in a Microelectromechanical Device for Multi-band Vibration Energy Harvesting," *Nature Publishing Group*, no. July, pp. 1–8, 2016. [Online]. Available: http://dx.doi.org/10.1038/srep30167

[28] B. J. Gallacher, Z. Hu, K. M. Harish, S. Bowles, and H. Grigg, "The Application of Parametric Excitation in Resonant MEMS Gyroscopes." Springer, Cham, 2014, pp. 473–492. [Online]. Available: http://link.springer.com/10.1007/978-3-319-08266-0_36

[29] S. Chakram, Y. S. Patil, M. Vengalattore, G. G. Slade, E. D. Filho, J. R. Ruggiero, K. C. Iarosz, C. C. Martins, A. M. Batista, C. G. L. Martins, F. A. Marcus, I. L. Caldas, M. J. Correia, P. C. Rech, F. Prebianca, H. A. Albuquerque, R. M. Rubinger, N. Rubido, C. Cabeza, R. Ávila, A. Carrillo, B. A. Rodríguez, and A. A. Batista, "Squeezing of thermal noise in a parametrically-driven oscillator," *J. Phys.: Conf. Ser*, vol. 285. [Online]. Available: http://iopscience.iop.org/1742-6596/285/1/012041

[30] H. Search, C. Journals, A. Contact, M. Iopscience, and I. P. Address, "Nonlinear Piezoelectric Effect in Ferroelectric Ceramics," vol. 5292.

[31] A. J. Dick, "Characterizing Effective d 31 Values for PZT from the Nonlinear Oscillations of Clamped-Clamped Micro- Resonators," vol. 59, pp. 50–55, 2013.

[32] ——, "Characterizing Effective d 31 Values for PZT from the Nonlinear Oscillations of Clamped-Clamped Micro- Resonators," vol. 59, pp. 50–55, 2013.

[33] P. Rafel, "Extrinsic contribution to the non-linearity in a PZT disc," vol. 2648.

[34] W. Yeon Hwang, K. Geun Lee, C. Jin Yang, G. Tao, B. Choubey, T. Kobayashi, R. Maeda, M. Harashima, K. Yasui, M. Moriyama, H. Liew Ong, S. Ghatnekar-Nilsson, J. Lindahl, and A. Dahlin, "Strong nonlinear harmonic generation in a PZT/Aluminum resonator," *J. Phys.: Conf. Ser*, vol. 195, 2009. [Online]. Available: http://iopscience.iop.org/1742-6596/195/1/012006

[35] S. Sherrit and B. K. Mukherjee, "Characterization of Piezoelectric Materials for Transducers." [Online]. Available: https://arxiv.org/ftp/arxiv/papers/0711/0711.2657.pdf

[36] H. Li, S. Preidikman, B. Balachandran, and C. D. Mote, "Nonlinear free and forced oscillations of piezoelectric microresonators," *Journal of Micromechanics and Microengineering*, vol. 16, no. 2, pp. 356–367, feb 2006. [Online]. Available: http://stacks.iop.org/0960-1317/16/i=2/a=021?key=crossref.f1055f47d9e66c3408fbd82898c5bf3f

[37] B. Li, G. Li, Q. Yin, K. Ayusawa, T. Arai, H. Sato, J. Takarada, K. Imoto, K. Yamamoto, A. Kokubo, M. Ohno, W. Bai, X. Meng, J. Yang, S. Goljahi, C. S. Lynch, M. H. Lente, and J. A. Eiras, "Interrelationship between self-heating and ferroelectric properties in PZT ceramics during polarization reorientation," *J. Phys.: Condens. Matter*, vol. 12, no. 1200, pp. 5939–5950, 2000. [Online]. Available: http://iopscience.iop.org/0953-8984/12/27/312

[38] R. Keoschkerjan, M. Harutyunyan, and H. Wurmus, "Analysis of self-heating phenomenon of piezoelectric microcomponents actuated harmonically."

[39] F. A. Levinzon, "Fundamental Noise Limit of Piezoelectric Accelerometer," vol. 4, no. 1, pp. 108–111, 2004.

[40] S. Dalola, V. Ferrari, and D. Marioli, "Procedia Engineering Pyroelectric Effect in PZT Thick Films for Thermal Energy Harvesting in Low-Power Sensors," *Procedia Engineering*, vol. 5, pp. 685–688.

[41] D. Damjanovic, R. C. Kell, R. Kandilian, A. Navid, and L. Pilon, "Experiments to demonstrate piezoelectric and pyroelectric effects Ferroelectric, dielectric and piezoelectric properties of ferroelectric thin films and ceramics The pyroelectric energy harvesting capabilities of PMNPT near the morphotropic phaseboundary," *Phys. Educ*, vol. 48, 2013. [Online]. Available: http://iopscience.iop.org/0031-9120/48/4/438

[42] S. Ueha, Y. Tomikawa, M. Kurosawa, and N. Nakamura, *Ultrasonic motors: theory and applications*. Oxford University Press, USA, 1993, vol. 29.

[43] K. Uchino, "Piezoelectric ultrasonic motors: overview," *Smart Materials and structures*, vol. 7, no. 3, p. 273, 1998.

[44] K. Uchino, S. Cagatay, B. Koc, S. Dong, P. Bouchilloux, and M. Strauss, "Micro piezoelectric ultrasonic motors," *Journal of electroceramics*, vol. 13, no. 1-3, pp. 393–401, 2004.

[45] T. Morita, "Miniature piezoelectric motors," *Sensors and Actuators A: Physical*, vol. 103, no. 3, pp. 291–300, 2003.

[46] K. Uchino, *Piezoelectric actuators and ultrasonic motors*. Springer Science & Business Media, 1996, vol. 1.

[47] Y. Chen, Q. Liu, and T. Zhou, "A traveling wave ultrasonic motor of high torque," *Ultrasonics*, vol. 44, pp. e581–e584, 2006.

[48] Z. Wan and H. Hu, "Modeling and experimental analysis of the linear ultrasonic motor with in-plane bending and longitudinal mode," *Ultrasonics*, vol. 54, no. 3, pp. 921–928, 2014.

[49] X. Yang, Y. Liu, W. Chen, and J. Liu, "Miniaturization of a longitudinal–bending hybrid linear ultrasonic motor," *Ceramics International*, vol. 41, pp. S607–S611, 2015.

[50] Y. Liu, X. Yang, W. Chen, and J. Liu, "A rotary piezoelectric actuator using longitudinal and bending hybrid transducer," *AIP Advances*, vol. 2, no. 4, p. 042136, 2012.

[51] Y. Liu, J. Liu, W. Chen, and S. Shi, "A u-shaped linear ultrasonic motor using longitudinal vibration transducers with double feet," *IEEE transactions on ultrasonics, ferroelectrics, and frequency control*, vol. 59, no. 5, pp. 981–989, 2012.

[52] Y. Liu, W. Chen, X. Yang, and J. Liu, "A t-shape linear piezoelectric motor with single foot," *Ultrasonics*, vol. 56, pp. 551–556, 2015.

[53] M. Kurosawa, K. Nakamura, T. Okamoto, and S. Ueha, "An ultrasonic motor using bending vibrations of a short cylinder," *IEEE transactions on ultrasonics, ferroelectrics, and frequency control*, vol. 36, no. 5, pp. 517–521, 1989.

[54] Y. Liu, D. Xu, Z. Yu, J. Yan, X. Yang, and W. Chen, "A novel rotary piezoelectric motor using first bending hybrid transducers," *Applied Sciences*, vol. 5, no. 3, pp. 472–484, 2015.

[55] J.-M. Seo, J. Hur, and H.-G. Sung, "A novel ultrasonic motor using orthogonal bimorphs," *IEEE Transactions on Magnetics*, vol. 43, no. 4, pp. 1413–1416, 2007.

[56] H. D. Choi, J. H. Kim, S. Kim, and Y. K. Kwak, "Development of piezoelectric motor using momentum generated by bimorph," *Review of Scientific Instruments*, vol. 76, no. 10, pp. 1–7, 2005.

[57] S. Kondo, D. Koyama, and K. Nakamura, "Miniaturization of the traveling wave ultrasonic linear motor using series connection of bimorph transducers," in *2011 IEEE International Ultrasonics Symposium*. IEEE, 2011, pp. 790–793.

[58] D. Avirovik and S. Priya, "L-shaped piezoelectric motor-part i: Design and experimental analysis," *IEEE transactions on ultrasonics, ferroelectrics, and frequency control*, vol. 59, no. 1, pp. 98–107, 2012.

[59] X. Li, P. Ci, G. Liu, and S. Dong, "A two-layer linear piezoelectric micromotor," *IEEE transactions on ultrasonics, ferroelectrics, and frequency control*, vol. 62, no. 3, pp. 405–411, 2015.

[60] W. Chen, S. Shi, Y. Liu, and P. Li, "A new traveling wave ultrasonic motor using thick ring stator with nested pzt excitation," *IEEE transactions on ultrasonics, ferroelectrics, and frequency control*, vol. 57, no. 5, pp. 1160–1168, 2010.

[61] H. K. Kommepalli, K. Mateti, C. D. Rahn, and S. A. Tadigadapa, "Piezoelectric t-beam actuators," *Journal of Mechanical Design*, vol. 133, no. 6, p. 061003, 2011.

[62] M. Bexell and S. Johansson, "Fabrication and evaluation of a piezoelectric miniature motor," *Sensors and Actuators A: Physical*, vol. 75, no. 1, pp. 8–16, 1999.

[63] S. Nadig, S. Ardanuç, and A. Lal, "Planar laser-micro machined bulk pzt bimorph for in-plane actuation," in *2013 Joint IEEE International Symposium on Applications of Ferroelectric and Workshop on Piezoresponse Force Microscopy (ISAF/PFM)*. IEEE, 2013, pp. 152–155.

[64] ——, "Monolithic piezoelectric in-plane motion stage with low cross-axis-coupling," in *2014 IEEE 27th International Conference on Micro Electro Mechanical Systems (MEMS)*. IEEE, 2014, pp. 524–527.

[65] A. K. Brown and Y. Lu, "Performance Test Results of an Integrated GPS/MEMS Inertial Navigation Package," 2004. [Online]. Available: http://ftp.navsys.com/Papers/0409001.pdf

[66] N. Barbour and G. Schmidt, "Inertial sensor technology trends," *IEEE Sensors Journal*, vol. 1, no. 4, pp. 332–339, 2001. [Online]. Available: http://ieeexplore.ieee.org/document/983473/

[67] M. El-Diasty, A. El-Rabbany, and S. Pagiatakis, "Temperature variation effects on stochastic characteristics for low-cost MEMS-based inertial sensor error," *Measurement Science and Technology*, vol. 18, no. 11, pp. 3321–3328, nov 2007. [Online]. Available: http://stacks.iop.org/0957-0233/18/i=11/a=009?key=crossref.1aa04a0fc0a1610efcb317f5411539c8

[68] M. Tanaka, "An industrial and applied review of new MEMS devices features," *Microelectronic Engineering*, vol. 84, no. 5, pp. 1341–1344, 2007. [Online]. Available: http://www.sciencedirect.com/science/article/pii/S0167931707001633

[69] J. Y. Cho, J.-K. Woo, J. Yan, R. L. Peterson, and K. Najafi, "Fused-Silica Micro Birdbath Resonator Gyroscope," *Journal of Microelectromechanical Systems*, vol. 23, no. 1, pp. 66–77, feb 2014. [Online]. Available: http://ieeexplore.ieee.org/document/6675759/

[70] D. Senkal, M. J. Ahamed, M. H. A. Ardakani, S. Askari, and A. M. Shkel, "Demonstration of 1 Million <inline-formula> <tex-math notation="LaTeX">Q </tex-math></inline-formula>-Factor on Microglassblown Wineglass Resonators With Out-of-Plane Electrostatic Transduction," *Journal of Microelectromechanical Systems*, vol. 24, no. 1, pp. 29–37, feb 2015. [Online]. Available: http://ieeexplore.ieee.org/document/6955708/

[71] G. Casinovi, W. K. Sung, M. Dalal, A. N. Shirazi, and F. Ayazi, "Electrostatic self-calibration of vibratory gyroscopes," in *2012 IEEE 25th International Conference on Micro Electro Mechanical Systems (MEMS)*. IEEE, jan 2012, pp. 559–562. [Online]. Available: http://ieeexplore.ieee.org/document/6170237/

[72] A. A. Trusov, M. R. Phillips, G. H. Mccammon, D. M. Rozelle, and A. D. Meyer, "Continuously self-calibrating CVG system using hemispherical resonator gyroscopes," in *2015 IEEE International Symposium on Inertial Sensors and Systems (ISISS) Proceedings*. IEEE, mar 2015, pp. 1–4. [Online]. Available: http://ieeexplore.ieee.org/document/7102362/

[73] B. Eminoglu, M. H. Kline, I. Izyumin, Y.-C. Yeh, and B. E. Boser, "Background calibrated MEMS gyroscope," in *IEEE SENSORS 2014 Proceedings*. IEEE, nov 2014, pp. 922–925. [Online]. Available: http://ieeexplore.ieee.org/lpdocs/epic03/wrapper.htm?arnumber=6985152

[74] E. E. Aktakka, J.-K. Woo, D. Egert, R. J. M. Gordenker, and K. Najafi, "A Microactuation and Sensing Platform With Active Lockdown for <italic>In Situ</italic> Calibration of Scale Factor Drifts in Dual-Axis Gyroscopes," *IEEE/ASME Transactions on Mechatronics*, vol. 20, no. 2, pp. 934–943, apr 2015. [Online]. Available: http://ieeexplore.ieee.org/document/6832587/

[75] H. S. Kim and Y. M. Cho, "Design and modeling of a novel 3-DOF precision micro-stage," *Mechatronics*, vol. 19, no. 5, pp. 598–608, 2009. [Online]. Available: http://dx.doi.org/10.1016/j.mechatronics.2009.01.004

[76] C. H. Liu, W. Y. Jywe, Y. R. Jeng, T. H. Hsu, and Y. tsung Li, "Design and control of a long-traveling nano-positioning stage," *Precision Engineering*, vol. 34, no. 3, pp. 497–506, 2010. [Online]. Available: http://dx.doi.org/10.1016/j.precisioneng.2010.01.003

[77] J. W. Judy, "Microelectromechanical systems (MEMS): fabrication, design and applications," *Smart Mater. Struct*, vol. 10, pp. 1115–1134, 2001. [Online]. Available: http://www.leb.eei.uni-erlangen.de/termine/ferienakademie/2008/mikrosysteme/Judy_MEMS_Review.pdf

[78] P. R. Ouyang, R. C. Tjiptoprodjo, W. J. Zhang, and G. S. Yang, "Micro-motion devices technology: The state of arts review," *International Journal of Advanced Manufacturing Technology*, vol. 38, no. 5-6, pp. 463–478, 2008.

[79] K. Uchino and S. Takahashi, "Multilayer ceramic actuators," *Current Opinion in Solid State and Materials Science*, vol. 1, no. 5, pp. 698–705, oct 1996. [Online]. Available: http://linkinghub.elsevier.com/retrieve/pii/S1359028696800544

[80] D. Corey and A. Hudspeth, "Mechanical stimulation and micromanipulation with piezoelectric bimorph elements," *Journal of Neuroscience Methods*, vol. 3, no. 2, pp. 183–202, 1980. [Online]. Available: http://www.sciencedirect.com/science/article/pii/0165027080900254

[81] K. Oldham, J. Pulskamp, R. Polcawich, and M. Dubey, "Thin-Film PZT Lateral Actuators With Extended Stroke," *Journal of Microelectromechanical*

Systems, vol. 17, no. 4, pp. 890–899, aug 2008. [Online]. Available: http://ieeexplore.ieee.org/document/4570438/

[82] N. Yoshimizu, A. Lal, and C. R. Pollock, "Nanometrology Using a Quasiperiodic Pattern Diffraction Optical Ruler," *Journal of Microelectromechanical Systems*, vol. 19, no. 4, pp. 865–870, aug 2010. [Online]. Available: http://ieeexplore.ieee.org/document/5484589/

[83] Y. K. Yong and T.-F. Lu, "The effect of the accuracies of flexure hinge equations on the output compliances of planar micro-motion stages," *Mechanism and Machine Theory*, vol. 43, no. 3, pp. 347–363, 2008. [Online]. Available: http://www.sciencedirect.com/science/article/pii/S0094114X07000626

[84] M. Muraoka and S. Sanada, "Displacement amplifier for piezoelectric actuator based on honeycomb link mechanism," *Sensors and Actuators A: Physical*, vol. 157, no. 1, pp. 84–90, 2010. [Online]. Available: http://www.sciencedirect.com/science/article/pii/S0924424709004622

[85] Y. Nada, M. Medhat, M. Nagi, F. Marty, B. Saadany, and T. Bourouina, "Mechanical displacement multiplier: 250 μM stable travel range MEMS actuator using frictionless simple compliant structures," in *2012 IEEE 25th International Conference on Micro Electro Mechanical Systems (MEMS)*. IEEE, jan 2012, pp. 1161–1164. [Online]. Available: http://ieeexplore.ieee.org/document/6170369/

[86] G. K. Fedder, "Simulation of Microelectromechanical Systems," 1994. [Online]. Available: https://www.ece.cmu.edu/ mems/pubs/pdfs/ucberkeley/phd_thesis/0053_fedder-1994.pdf

[87] N. Lobontiu, "In-Plane Compliances of Planar Flexure Hinges With Serially Connected Straight- and Circular-Axis Segments," *Journal of Mechanical Design*, vol. 136, no. 12, p. 122301, oct 2014.

[88] Y. A. Genenko, J. Glaum, and M. J. Hoffmann, "Mechanisms of aging and fatigue in ferroelectrics," *Materials Science and Engineering: B*, vol. 192, pp. 52–82, 2015.

[89] J. Glaum, T. Granzow, L. A. Schmitt, H.-J. Kleebe, and J. Rödel, "Temperature and driving field dependence of fatigue processes in PZT bulk ceramics," *Acta Materialia*, vol. 59, no. 15, pp. 6083–6092, 2011. [Online]. Available: http://www.sciencedirect.com/science/article/pii/S1359645411004319

[90] M. Guizar-Sicairos, S. T. Thurman, and J. R. Fienup, "Efficient subpixel image registration algorithms," *Optics Letters*, vol. 33, no. 2, p. 156, jan 2008. [Online]. Available: https://www.osapublishing.org/abstract.cfm?URI=ol-33-2-156

[91] N. El-Sheimy, H. Hou, and X. Niu, "Analysis and Modeling of Inertial Sensors Using Allan Variance," *IEEE TRANSACTIONS ON INSTRUMENTATION AND MEASUREMENT*, vol. 57, no. 1, 2008.

[92] E. Tatar, T. Mukherjee, and G. K. Fedder, "Stress Effects and Compensation of Bias Drift in a MEMS Vibratory-Rate Gyroscope," *Journal of Microelectromechanical Systems*, pp. 1–11, 2017. [Online]. Available: http://ieeexplore.ieee.org/document/7887664/

[93] I. P. Prikhodko, A. A. Trusov, and A. M. Shkel, "Compensation of drifts in high-Q MEMS gyroscopes using temperature self-sensing," *Sensors and Actuators A: Physical*, vol. 201, pp. 517–524, oct 2013. [Online]. Available: http://linkinghub.elsevier.com/retrieve/pii/S0924424712007613

[94] N. Yazdi, F. Ayazi, and K. Najafi, "Micromachined inertial sensors," *Proceedings of the IEEE*, vol. 86, no. 8, pp. 1640–1659, 1998. [Online]. Available: http://ieeexplore.ieee.org/document/704269/

[95] J. Söderkvist, "Micromachined gyroscopes," *Sensors and Actuators A: Physical*, vol. 43, no. 1-3, pp. 65–71, may 1994. [Online]. Available: http://linkinghub.elsevier.com/retrieve/pii/092442479300667S

[96] K. Ono, M. Yachi, and N. Wakatsuki, "H-Type Single Crystal Piezoelectric Gyroscope of an Oppositely Polarized LiNbO ₃ Plate," *Japanese Journal of Applied Physics*, vol. 40, no. Part 1, No. 5B, pp. 3699–3703, may 2001. [Online]. Available: http://stacks.iop.org/1347-4065/40/3699

[97] K. Maenaka, H. Kohara, M. Nishimura, T. Fujita, and Y. Takayama, "Novel Solid Micro-Gyroscope," in *19th IEEE International Conference on Micro Electro Mechanical Systems*. IEEE, 2006, pp. 634–637. [Online]. Available: http://ieeexplore.ieee.org/document/1627879/

[98] K. Jose, W. Suh, P. Xavier, V. Varadan, and V. Varadan, "Surface acoustic wave MEMS gyroscope," *Wave Motion*, vol. 36, no. 4, pp. 367–381, oct 2002. [Online]. Available: http://linkinghub.elsevier.com/retrieve/pii/S0165212502000306

[99] M. Hodjat-Shamami, A. Norouzpour-Shirazi, R. Tabrizian, and F. Ayazi, "A dynamically mode-matched piezoelectrically transduced high-frequency flexural disk gyroscope," in *2015 28th IEEE International Conference on Micro Electro Mechanical Systems (MEMS)*. IEEE, jan 2015, pp. 789–792. [Online]. Available: http://ieeexplore.ieee.org/document/7051077/

[100] S. Nadig, V. Pinrod, S. Ardanuç, and A. Lal, "Multi-modal mechanical stimuli stage for in-situ calibration of MEMS gyroscopes," in *2015 IEEE International Symposium on Inertial Sensors and Systems (ISISS) Proceedings*. IEEE, mar 2015, pp. 1–2. [Online]. Available: http://ieeexplore.ieee.org/document/7102393/

[101] A. Sharma, M. F. Zaman, M. Zucher, and F. Ayazi, "A 0.1/HR bias drift electronically matched tuning fork microgyroscope," in *2008 IEEE 21st International Conference on Micro Electro Mechanical Systems*. IEEE, jan 2008, pp. 6–9. [Online]. Available: http://ieeexplore.ieee.org/document/4443579/

[102] M. Y. Elsayed, P.-V. Cicek, F. Nabki, and M. N. El-Gamal, "Bulk Mode Disk Resonator With Transverse Piezoelectric Actuation and Electrostatic Tuning," *Journal of Microelectromechanical Systems*, vol. 25, no. 2, pp. 252–261, apr 2016. [Online]. Available: http://ieeexplore.ieee.org/document/7397821/

[103] E. E. Aktakka, J.-K. Woo, D. Egert, R. J. M. Gordenker, and K. Najafi, "A Microactuation and Sensing Platform With Active Lockdown for <italic>In Situ</italic> Calibration of Scale Factor Drifts in Dual-Axis Gyroscopes," *IEEE/ASME Transactions on Mechatronics*, vol. 20, no. 2, pp. 934–943, apr 2015. [Online]. Available: http://ieeexplore.ieee.org/document/6832587/

[104] M. Kline, "Frequency Modulated Gyroscopes," 2013.

[105] D. Lynch, "Vibratory Gyro Analysis By The Method Of Avergaing," *Proc. 2nd St. Petersburg Conf. on Gyroscopic Technology and Navigation, St. Petersburg*, 1995.

[106] M. Weinberg and A. Kourepenis, "Error Sources in In-Plane Silicon Tuning-Fork MEMS Gyroscopes," *Journal of Microelectromechanical Systems*, vol. 15, no. 3, pp. 479–491, jun 2006. [Online]. Available: http://ieeexplore.ieee.org/document/1638473/

[107] R. Keoschkerjan, M. Harutyunyan, and H. Wurmus, "Analysis of self-

heating phenomenon of piezoelectric microcomponents actuated harmonically."

[108] I. Prikhodko, "Development of a self-calibrated mems gyrocompass for north-finding and tracking," Ph.D. dissertation, University of California, Irvine, 2013. [Online]. Available: http://gradworks.umi.com/35/65/3565862.html

[109] A. Norouz Pour Shirazi, Ph.D. dissertation, Georgia Institute of Technology.

[110] C. Acar and A. Shkel, *MEMS Vibratory Gyroscopes*, ser. MEMS Reference Shelf. Boston, MA: Springer US, 2009. [Online]. Available: http://link.springer.com/10.1007/978-0-387-09536-3

[111] I. P. Prikhodko, J. A. Gregory, W. A. Clark, J. A. Geen, M. W. Judy, C. H. Ahn, and T. W. Kenny, "Mode-matched MEMS Coriolis vibratory gyroscopes: Myth or reality?" in *2016 IEEE/ION Position, Location and Navigation Symposium (PLANS)*. IEEE, apr 2016, pp. 1–4. [Online]. Available: http://ieeexplore.ieee.org/document/7479674/

[112] H. Search, C. Journals, A. Contact, M. Iopscience, and I. P. Address, "Nonlinear Piezoelectric Effect in Ferroelectric Ceramics," vol. 5292.

[113] Q.-B. Zhou, Y.-k. Lu, and S.-Y. Zhang, "Extraction of electromechanical coupling coefficient of piezoelectric thin films deposited on substrates," *Ultrasonics*, vol. 39, no. 5, pp. 377–382, aug 2001. [Online]. Available: http://linkinghub.elsevier.com/retrieve/pii/S0041624X01000622

[114] A. Sharma, M. F. Zaman, and F. Ayazi, "A Sub-$0.2^0/hr$ Bias Drift Micromechanical Silicon Gyroscope With Automatic CMOS Mode-Matching," *IEEE Journal of Solid-State Circuits*, vol. 44, no. 5, pp. 1593–1608, may 2009. [Online]. Available: http://ieeexplore.ieee.org/document/4907312/

[115] S. Nadig, S. Ardanuc, and A. Lal, "Monolithic piezoelectric in-plane motion stage with low cross-axis-coupling," in *2014 IEEE 27th International Conference on Micro Electro Mechanical Systems (MEMS)*. IEEE, jan 2014, pp. 524–527. [Online]. Available: http://ieeexplore.ieee.org/document/6765693/

[116] J. L. Fu, Y. Nakano, L. D. Sorenson, and F. Ayazi, "Multi-axis AlN-on-Silicon vibration energy harvester with integrated frequency-upconverting transducers," in *2012 IEEE 25th International Conference on*

Micro Electro Mechanical Systems (MEMS). IEEE, jan 2012, pp. 1269–1272. [Online]. Available: http://ieeexplore.ieee.org/document/6170388/

[117] E. E. Aktakka, R. L. Peterson, and K. Najafi, "A CMOS-compatible piezoelectric vibration energy scavenger based on the integration of bulk PZT films on silicon," in *2010 International Electron Devices Meeting*. IEEE, dec 2010, pp. 31.5.1–31.5.4. [Online]. Available: http://ieeexplore.ieee.org/document/5703459/

[118] S. Nadig, S. Ardanuc, and A. Lal, "Planar laser-micro machined bulk PZT bimorph For in-plane actuation," in *2013 Joint IEEE International Symposium on Applications of Ferroelectric and Workshop on Piezoresponse Force Microscopy (ISAF/PFM)*. IEEE, jul 2013, pp. 152–155. [Online]. Available: http://ieeexplore.ieee.org/lpdocs/epic03/wrapper.htm?arnumber=6748750

[119] ——, "Monolithic piezoelectric in-plane motion stage with low cross-axis-coupling," in *2014 IEEE 27th International Conference on Micro Electro Mechanical Systems (MEMS)*. IEEE, jan 2014, pp. 524–527. [Online]. Available: http://ieeexplore.ieee.org/document/6765693/

[120] A. Lei, R. Xu, L. M. Borregaard, M. Guizzetti, O. Hansen, and E. V. Thomsen, "Impedance Based Characterization of a High-Coupled Screen Printed PZT Thick Film Unimorph Energy Harvester," *Journal of Microelectromechanical Systems*, vol. 23, no. 4, pp. 842–854, aug 2014. [Online]. Available: http://ieeexplore.ieee.org/document/6710107/